

# **Wearable System for Real-Time Sensing of Biomarkers in Human Sweat**

**Thèse N° 9696**

Présentée le 22 août 2019

à la Faculté des sciences et techniques de l'ingénieur  
Laboratoire des dispositifs nanoélectroniques  
Programme doctoral en génie électrique

pour l'obtention du grade de Docteur ès Sciences

par

**Junrui ZHANG**

Acceptée sur proposition du jury

Dr J.-M. Sallese, président du jury  
Prof. M. A. Ionescu, Prof. M. Mazza, directeurs de thèse  
Prof. L. Selmi, rapporteur  
Dr G. Salvatore, rapporteur  
Prof. A. Hierlemann, rapporteur

2019



“美妙人生的关键在于，你能迷上什么东西。”

—— 《球状闪电》，刘慈欣，2005

*The key to a wonderful life is that you are able to fall in love  
with something.*

— — *Ball Lightning*, Cixin Liu, 2005

To all the beloved who made life and work enjoyable during my Ph.D.





# Acknowledgements

---

This thesis is the outcome of learning and getting help from people I had the honor to work with during the past five years of my PhD life in Switzerland. My foremost gratitude is addressed to my supervisor, Professor Ionescu, for supporting me to work in a very interesting multidisciplinary topic. I am most grateful that he kept me on track of the high level directions and always offered me the right opportunities to get hands on new and challenging work.

Next, I would like to thank my co-supervisor, Professor Marco Mazza, for guiding me into the field of IC design, giving me enough freedom to practice, and always being positive and supportive in the research.

Besides my supervisors, I would like to acknowledge and thank the other members of the jury that reviewed this thesis: Dr. Jean Michelle-Sallèse, President of the Jury, Prof. Luca Selmi from University of Modena and Reggio Emilia, Prof. Andreas Hierlemann from ETHZ, and Dr. Giovanni Salvatore from ABB Zurich.

I have had the opportunity to work in iPrint (Fribourg, Switzerland) for the first two years of my PhD. There I have met a team of highly motivated people who were always enthusiastic about *la vie*. I appreciate every event we had together. Thanks to Fritz for holding the team altogether, and bringing us out for relaxing from time to time. My first officemate in Switzerland, Emanuele, you were perfect in sharing the same influence in both English and French, and I really enjoyed the time spent with you. To the rest of iPrint team, Celine, Johannes, Matthew, Lorenzo, Florian, Damien, Jonathan, Gaëtan, Muriel, Raphaël, Thanks to you all. Thanks to the administrative staffs in HEIA-FR, Charlotte and Isabelle, for helping so much at the beginning of my settling.

I have had the chance to work with and learn from a great team from many disciplines. I would like to take the opportunity to express my most sincere gratitude to all of you. Hoel, thanks for giving many suggestions and your always calm attitude during the project. Fabien and Johan, thank you for contributing your expertise to help me in the project and always keeping the positive atmosphere in our team. Thanks to Marc, Pietro, Julian for interesting discussions and help in experiments. To the rest of the Xsensio family,

Guillaume, Ron, Aristeia, Yann, Ali, and Esmeralda, it has been a great experience to work and discuss with you all. To my officemates, Francesco, Manee and Erick, I could never have made it through the mess of my thesis without your help. Sadegh, thank you for being a lot more quiet than Erick during the last period of writing a thesis.

I would also like to address many thanks to three master students, Michael, Jérémie, and Bilggun, for contributing your time in discussing and developing of the software that has finally helped a lot in the visualizing of the project. Indeed, I have learnt a lot from your work.

Thanks to Karin, Isabell, Cedric, Raymond, and Valerie, who had all the patience to deal with my administrative procedures. I am also grateful to the CMi staffs for their support during my time in the cleanroom. Special thanks to Giancarlo Corradini, who helped me with last minute requirements more times than I can count. Many thanks to the ACI staffs for their tremendous help in assembling PCBs. My special thanks to Peter Brühlmeier and Jean-Marie Barblan, who helped me pass every urgent deadlines in my project.

My sincere thanks also go to all my Chinese friends for the time spent together during my PhD and providing me with a lot of knowledge and happiness.

Last but not least, I would like to thank my family: my parents, my uncles and aunts, my cousins who provided me much mental support; my grandmother who passed away during my PhD, I hope her to be happy seeing my graduation. Thanks to my grandparents for taking care of me, teaching me many things in my childhood.

Lausanne, 20 May, 2019

# Abstract

---

Wearable sweat sensing systems offer non-invasive and real-time bio-data streaming solutions. They open the possibility for continuous monitoring of biomarkers' concentrations as well as their variation in sweat, which is a complementary to current passive and discrete health check procedures. Sweat contains many biomarkers, ranging from electrolytes and small molecules, to peptides and proteins. Some of these biomarkers' concentrations have been demonstrated to be closely correlated to their concentrations in blood, while others show more complicated partitioning procedures related to re-adsorption to sweat gland, sweat rate, contamination from old skin and degradation due to exposure to ambient environment. Therefore, on-body sweat sensing is of utmost importance in both application-driven industry and clinical research.

Yet, there are several challenges in the development of on-body sweat sensing systems. *i.* reliable and scalable sensors that can be integrated within a miniaturized area, *ii.* real-time sweat sampling and analysis that minimizes contamination and preserves maximum fidelity of bio-info from biomarker degradation. The goal of this thesis is to demonstrate a wearable sensing system for simultaneous monitoring of multiple analytes in sweat, with building blocks potentially solving the above-mentioned challenges.

This thesis reports the development and experimental validation of a wearable sensor system that allows multiplexed sensing and streaming of bio-data concerning electrolyte concentrations in sweat. The wearable sensor system comprises:

I. Multi-analyte (pH, Na<sup>+</sup>, K<sup>+</sup> and Ca<sup>2+</sup>) sensing chip that incorporates high performance, high yield, high robustness, ultra-low power (down to pico-Watt per sensor) ISFETs. High sensitivities close to the Nernstian limit for all the analytes are demonstrated. Simultaneous time-dependent recording of multiple analytes and dedicated tests with prepared samples containing many known analytes, demonstrate the high selectivity of the reported sensors.

II. Bio-compatible skin interface (microfluidics) with drop-to-drop resolution, capable of sampling and analyzing sweat drops with volume as low as tens of nano-Liters. Continuous electronic readout of sweat rate is enabled with the implementation of microfluidics.

III. Multiplexed readout circuits are implemented on bio-compatible substrates, in order to simultaneously readout the electrolyte concentrations and sweat rate in real-time, enabling bio-data streaming.

We report integration of all the needed functions in a wearable patch that is developed to be tested on humans.

Keywords: Wearable sensor; Biomarker analysis; 3D-EMG-ISFET; Skin microfluidics; Passive microfluidics; Hydrophilic microfluidics; Ultra-low dead volume; Label-free sensor; Biochemical sensing; Continuous sweat rate monitor.

## Riassunto

---

I sensori di sudore indossabili offrono soluzioni per la raccolta non-invasiva e in tempo reale di dati biologici. Aprono così la possibilità di monitorare continuamente la concentrazione di bioindicatori nel sudore e i suoi cambiamenti nel tempo, offrendo opzioni complementari alle attuali procedure passive e non invasive per il controllo dello stato di salute. Il sudore contiene molti biomarcatori, che variano da elettroliti e piccole molecole fino a peptidi e proteine. È stato dimostrato che le concentrazioni di alcuni di questi biomarcatori nel sudore sono strettamente correlate alle rispettive concentrazioni nel sangue, mentre altre mostrano procedure di partizione più complesse, legate al riassorbimento da parte delle ghiandole sudorifere, alla velocità di sudorazione, alla contaminazione dovuta alla pelle e alla degradazione dovuta all'esposizione all'ambiente. Per questi motivi, l'analisi di sudore direttamente sul corpo è di fondamentale importanza sia per l'industria che per la ricerca clinica.

Ciononostante, esistono diverse sfide nello sviluppo di sensori di sudore indossabili: i) La fabbricazione di sensori affidabili e scalabili che possano essere integrati in un'area ridotta, ii) La raccolta e analisi in tempo reale del sudore, per minimizzare le contaminazioni e proteggere al meglio le informazioni biologiche dalla degradazione. L'obiettivo di questa tesi è dimostrare un sistema indossabile per il monitoraggio di multipli analiti nel sudore, con componenti potenzialmente capaci di superare le sfide menzionate.

Questa tesi riporta lo sviluppo e la verifica sperimentale di un sistema sensoristico indossabile che permette di misurare e trasferire dati biologici riguardanti la concentrazione di elettroliti nel sudore. Il sistema sensoristico indossabile comprende:

I. Un chip sensore predisposto per un set di analiti differenti (pH,  $\text{Na}^+$ ,  $\text{K}^+$  e  $\text{Ca}^{2+}$ ) che incorpora ISFET caratterizzati da alte performance, alto yield, alta robustezza e consumi ultra-ridotti (fino a un pico-Watt per sensore). Alte sensibilità, vicine al limite di Nernst, sono dimostrate per tutti gli analiti. Controlli simultanei di multipli analiti e test con campioni contenenti molti analiti in concentrazioni conosciute dimostrano l'alta selettività dei sensori presentati.

II. Un'interfaccia biocompatibile tra sensore ed epidermide (sistema microfluidico) con risoluzione goccia-goccia, capace di campionare e analizzare gocce di sudore con un

volume ridotto fino a poche decine di nano-Litri. Il controllo continuo della velocità di sudorazione è reso possibile dall'implementazione della microfluidica.

III. Circuiti di read-out multiplex implementati su substrati bio-compatibili, in modo da leggere simultaneamente le concentrazioni degli elettroliti e la velocità di sudorazione in tempo reale, rendendo possibile il trasferimento continuo di dati biologici.

Riportiamo l'integrazione di tutte le funzionalità necessarie in un adesivo indossabile che è stato testato su dei volontari.

Parole chiave: Dispositivo indossabile; Analisi di biomarcatori; 3D-EMG-ISFET; Sistema microfluidico sulla pelle; Sistema microfluidico passivo; Sistema microfluidico idrofilo; Volume morto ultra-ridotto; Sensori label-free; Sensori biochimici; Monitoraggio continuo della velocità di sudorazione.

# Contents

---

Acknowledgements.....	v
Abstract .....	vii
Riassunto.....	ix
Contents .....	xi
List of Figures.....	xv
List of Tables .....	xxi
List of equations.....	xxiii
Nomenclature.....	xxv
Greek letters .....	xxxi
Chapter 1 Introduction to Wearable Sweat Analysis.....	1
1.1 Complementary to Current Healthcare Procedures .....	2
1.2 Sweat as a Rich Data Mine .....	3
1.3 State of the Art .....	5
1.4 Challenges .....	7
1.5 Thesis outline .....	8
Chapter 2 Electrochemical Methods.....	11
2.1 Electrochemical Sensing System .....	12
2.2 Classification of Electrochemical Methods .....	15
2.3 Potentiometric Methods .....	16
2.3.1 Nernst Equation and Ion-Selective Electrodes (ISEs) .....	16
2.3.2 Solid State ISEs (SS-ISEs) .....	18
2.3.3 Ion Sensitive Field Effect Transistors (ISFETs).....	20
2.3.4 ISEs vs. ISFETs .....	25
2.4 Summary .....	26
Chapter 3 3D-Extende-Metal-Gate-ISFET .....	29

3.1	Introduction .....	30
3.2	Fabrication and Post-processing .....	32
3.3	pH Sensing .....	35
3.4	Trapped charge elimination.....	37
3.5	Drift .....	41
3.6	Multiple Cation Sensing.....	41
3.6.1	Functionalization .....	41
3.6.2	Sensitivity and Selectivity.....	43
3.7	Dynamic Response.....	47
3.8	In-vitro Sweat Tests.....	52
3.8.1	Results and Discussions.....	52
3.8.2	Experimental Methods.....	55
3.9	Conclusions .....	56
Chapter 4	Microfluidic Channel for Sweat Collection and Analysis.....	59
4.1	Introduction .....	60
4.2	Results and Discussions .....	66
4.3	Methods .....	78
4.3.1	Fabrication methods for the glass microfluidic chips.....	78
4.3.2	Experiment methods .....	81
4.4	Conclusions .....	82
Chapter 5	Readout Circuits .....	85
5.1	Typical Readout Circuits for ISFETs.....	86
5.2	Multiplexed current readout implementation .....	88
5.2.1	Block diagram .....	88
5.2.2	Multiplexer (MUX) .....	90
5.2.3	Current source.....	91
5.2.4	Operational amplifier (OPA) .....	94
5.2.5	Bandgap reference (BGP).....	97
5.2.6	Wearable sensor node implementation.....	100



5.3	Sweat-rate-to-frequency readout implementation .....	102
5.3.1	Block design and analysis.....	102
5.3.2	Component selection and circuit implementation.....	104
5.3.3	Experimental validation and discussions .....	105
5.4	Conclusions.....	108
Chapter 6	Conclusions .....	111
6.1	Main contributions.....	112
6.1.1	High performance, CMOS BEOL integrated 3D-EMG-ISFET sensors.....	112
6.1.2	Experimental verification of sensor performance with unspiked sweat samples .....	113
6.1.3	First demonstration of long term, continuous, electronic monitoring of low sweat rate .....	113
6.1.4	Integration and test of wearable, wirelessly powered sweat sensing patch.....	114
6.2	Outlook .....	114
6.2.1	Reliability of miniaturized ISMs.....	114
6.2.2	Sensing uncharged or weakly charged biomarkers.....	115
6.2.3	Microfluidics with long term sweat transporting capability.....	115
6.2.4	Continuous streaming and processing of physiological data .....	117
6.3	Concluding remarks .....	117
References	.....	119
Curriculum Vitae	.....	131



## List of Figures

---

Figure 1-1 Nowadays healthcare procedures.....	2
Figure 1-2 Adhesive RFID Na <sup>+</sup> sensing bandage [44].....	6
Figure 1-3 Wearable sweat-sampling microfluidic patch for glucose and lactate [49].....	7
Figure 1-4 Wearable organic electrochemical transistor for cortisol sensing [49]. ....	7
Figure 2-1 Constituents of a typical three-electrode electrochemical sensing system. ....	12
Figure 2-2. Family tree of electrochemical analysis methods. Different blocks distinguish different experimental conditions or analysis methods. The area of them doesn't stand for percentage in any sense. The thickness of the outer ring (orange) stands for the complexity of each method: thicker orange ring means a simpler implementation. ....	14
Figure 2-3 Schematic diagram showing a typical potentiometric cell with an ion-selective electrode. The ion-selective electrode's membrane separates the sample, which contains the analyte at an activity of $a_{A,samp}$ , from an internal solution containing the analyte with an activity of $a_{A,int}$ . [3] .....	17
Figure 2-4 a) An example of a SS-ISE coated with oxide for pH sensing: Al <sub>2</sub> O <sub>3</sub> sensing layer is in contact with a sample solution of certain pH. b) An example of a SS-ISE coated with ISM for charged ion sensing. c) Equivalent circuit schematic of SS-ISEs in potentiometric measurement. ....	18
Figure 2-5 a) A typical n-type MOSFET. b) The channel of an n-type MOSFET is depleted. c) Two drawings of typical ISFETs, constructed by combining SS-ISE and MOSFET techniques. d) An n-type MOSFET working in saturation, conducting a current from drain to source. ....	21
Figure 2-6 Schematic of a capacitance divider model that models the electrical behavior of an ISFET. Inset: simplified capacitance divider to model the MOSFET. ....	22
Figure 2-7 Differential amplifier readout configuration for ISE potentiometric sensing. ....	26
Figure 3-1 Cross-sectional view showing the fabrication of a 3D-EMG-ISFET from post-processing of a MOSFET. ....	32
Figure 3-2 a) FIB Cross section of CMOS ISFET before RIE, b) HAADF STEM indicating passivation Si <sub>3</sub> N <sub>4</sub> /SiO <sub>2</sub> layers above the top metal. c) – g) EDX analysis confirm constituent elements of Al, Ti, O, Si, N in the cross section. ....	33

Figure 3-3 a) FIB cross section of 3D-EMG-ISFET with RIE etched openings. b) HAADF STEM image indicating 7nm native oxide on exposed top metal used for sensing. c) – d) EDX analysis confirms elemental composition of Al <sub>2</sub> O <sub>3</sub> . .....	33
Figure 3-4 DC characteristics of the MOSFET devices. a) $I_D$ - $V_G$ characteristics when $V_D = 0.1$ V and $V_S = 0$ V for the MOSFET (measurement and post-layout simulation). b) $I_D$ - $V_G$ characteristics of different MOSFET devices from 9 CMOS chips, showing maximum device variation $\Delta V_{th} = 12$ mV. ....	34
Figure 3-5 Measurement setup. a) A photo with the measurement setup, PCB with test connectors. b) Zoom in of the epoxy well created to contain a drop of ~ 100 $\mu$ L LUT. c) Sketch of the measurement setup. R.E: Reference electrode. ....	35
Figure 3-6 DC characteristics and sensitivity for pH sensing. a) $I_D$ - $V_G$ characteristics of the 3D-EMG-ISFET in various pH buffers, together with simulation results from a SPICE behavioral model [104]. b) pH sensitivities extracted from the shift in $I_D$ - $V_G$ curve, at different $I_D$ levels. ....	36
Figure 3-7 Process steps for removing trapped charge. a) Before RIE: the Si <sub>3</sub> N <sub>4</sub> passivation layer is used as sensing dielectric. b) After RIE: the Al <sub>2</sub> O <sub>3</sub> layer is used for sensing. c) Wet etching. ....	38
Figure 3-8 Threshold variation results after removing the trapped charges. $\Delta V_{th}$ of the ISFETs measured in pH 7 buffer solution. ....	38
Figure 3-9 Stability study of the ISFET, comparison between native Al <sub>2</sub> O <sub>3</sub> and 8 nm HfO <sub>2</sub> deposited with ALD as sensing layer. a) Long term $I_D$ drift of the 3D-EMG-ISFET in a period of 20 hours. b) Zoom in of the drift characteristics from 10 <sup>th</sup> hour to 20 <sup>th</sup> hour. ....	40
Figure 3-10 3D-EMG-ISFET with different functionalization for sensing different ions. a) 3D-EMG-ISFET with Al <sub>2</sub> O <sub>3</sub> as the sensing layer. b) 3D-EMG-Na <sup>+</sup> sensitive FET. c) 3D-EMG-K <sup>+</sup> sensitive FET. d) 3D-EMG-Ca <sup>2+</sup> sensitive FET. All ion sensitive FETs use a specific ISM. ....	42
Figure 3-11 DC characteristics and sensitivity for Na <sup>+</sup> sensing. a) $I_D$ - $V_G$ characteristics of the 3D-EMG-Na <sup>+</sup> sensitive FET, in NaCl solutions of various concentrations. b) Sensitivity and Cross sensitivity plot for the Na <sup>+</sup> sensitive FET. ....	44
Figure 3-12 DC characteristics and sensitivity for K <sup>+</sup> sensing. a) $I_D$ - $V_G$ characteristics of the 3D-EMG-K <sup>+</sup> sensitive FET, in KCl solutions of various concentrations. b) Sensitivity and Cross sensitivity plot for the K <sup>+</sup> sensitive FET. ....	45

Figure 3-13 DC characteristics and sensitivity for $\text{Ca}^{2+}$ sensing. a) $I_D$ - $V_G$ characteristics of the 3D-EMG- $\text{Ca}^{2+}$ sensitive FET, in $\text{CaCl}_2$ solutions of various concentrations. b) Sensitivity and Cross sensitivity plot for the $\text{Ca}^{2+}$ sensitive FET.....	46
Figure 3-14 Dynamic response of the 3D-EMG-ISFET pH sensor.....	48
Figure 3-15 Dynamic response of the 3D-EMG-ISFET $\text{Na}^+$ sensor.....	48
Figure 3-16 Dynamic response of the 3D-EMG-ISFET $\text{K}^+$ sensor.....	49
Figure 3-17 Dynamic response of the 3D-EMG-ISFET $\text{Ca}^{2+}$ sensor. ....	49
Figure 3-18 CMOS sensor chip functionalized to simultaneously monitor $\text{K}^+$ and $\text{Na}^+$ . a) CMOS sensor chip containing five groups of 3D-EMG-ISFET sensors. QRE (quasi reference electrode): will be introduced later. b) A drop of $\text{K}^+$ and $\text{Na}^+$ ISM is casted on top of two groups of ISFET, respectively.....	50
Figure 3-19 Measurement setup for simultaneously measuring the two different ion sensors in the CMOS sensor chip shown in Figure 3-18. Inset: Exploded view of the fluidic cell configuration.....	51
Figure 3-20 Simultaneous dynamic response of the 3D-EMG- $\text{Na}^+$ and 3D-EMG- $\text{K}^+$ sensitive FETs, in solutions with varying concentrations of both $\text{Na}^+$ and $\text{K}^+$ .....	52
Figure 3-21 a) Dynamic measurements with sweat samples and various pH buffers to extract b) calibration curve for 3D-EMG-pH sensors, and calculate sweat pH values. c) Dynamic measurements with sweat samples and various $\text{NaCl}$ solutions to extract d) calibration curve for 3D-EMG- $\text{Na}^+$ sensors, and calculate sweat $\text{Na}^+$ concentrations. ....	54
Figure 4-1 Simplified skin cross section showing the structure of human sweat gland. Adapted from [4].....	61
Figure 4-2 Young's equation interpreted as a force balance at the interface. ....	64
Figure 4-3 Sketch of the microfluidic channel: showing the principle of the passive capillary pump. a) A drop of sweat emerges from the epidermis. b) Sweat drop grows to be in contact with the microfluidic surface. c) Sweat drop forming the equilibrium contact angles on the two surfaces. d) The sweat droplet breaks into two parts: the upper one caught in the channel, the lower one stays on the skin. e) 3-D drawing of the previous subplot (upside down). f) The ultra-hydrophilic channel surface spreads the upper drop evenly in the microfluidic channel.....	65
Figure 4-4. SU-8 microfluidic patterned on a glass chip (a) without and (b) with dummy metallic layer.....	67
Figure 4-5. Time stamped snapshots of liquid transporting through the SU-8 microfluidic chip.....	68

Figure 4-6. Channel conductance periodically modulated by the formation, transportation and removal of sweat droplets. ....	69
Figure 4-7. Time domain variation of channel conductance, showing that it is periodically modulated by the flow rate from 100 nL/min to 500 nL/min. a) Conductance vs. Time plot for nine repetitions of the sweep. b) Zoom-in of the 4 <sup>th</sup> repetition. ....	72
Figure 4-8. Channel conductance variation frequency versus flow rate for every repetition of sweeping of flow rate, showing the flow-rate-to-frequency modulation. ....	74
Figure 4-9. Channel conductance variation frequency versus flow rate for every repetition .....	77
Figure 4-10. Experiment setup. (a) The microfluidic chip wire-bonded to a flexible substrate, attached to (b) artificial skin, with adhesive material as sealing and drain material to ensure a constant adsorption of liquid. The pink color is due to the drain material having absorbed drops of liquid containing a fluorescent dye. ....	79
Figure 4-11. Artificial skin contact angle measurement, for different droplet sizes of DI water. ....	80
Figure 5-1 One type of readout circuit for ISFET: source follower readout. ....	87
Figure 5-2 Another type of readout circuit for ISFET: Transconductance readout. ....	87
Figure 5-3 Block diagram of the ASIC implementation for the transconductance readout. $G'_i$ is the liquid-to-sensing membrane interfaces, $D_i$ is the drain terminal of the $i$ th ISFET, $i = 1, 2, \dots, 16$ . ....	88
Figure 5-4 MUX implementation with CMOS gates .....	89
Figure 5-5 Implementation of a) AND and b) NOT gates .....	90
Figure 5-6 Implementation of CMOS SPDT switches, a) block diagram, b) CMOS circuit	91
Figure 5-7 Beta-multiplier current source. a) Schematic diagram. b) Design parameters of the circuit, $R_s = 100 \text{ k}\Omega$ . ....	92
Figure 5-8 Simulation results of the Beta-multiplier current source. a) Output current varying with supply voltage. b) Output current varying with temperature. ....	93
Figure 5-9 Two stage operational amplifier. a) Schematic diagram. b) Design parameters of the circuit, $C_M = 11 \text{ pF}$ . ....	94
Figure 5-10 Simulation results for the key performances of OPA. a) Open-loop gain and phase margin. b) Common-mode rejection ratio (CMRR) and power supply rejection ratio (PSRR). c) Quiescent supply current varying with temperature at different supply voltages. d) Input referred voltage noise spectrum. ....	96

Figure 5-11 Bandgap reference. a) Schematic diagram. b) Design parameters. $R_s = 10\text{ k}\Omega$ , $R_{out} = 100\text{ k}\Omega$ .....	97
Figure 5-12 Simulation results for the BGP voltage source. a) Output voltage vs. temperature at $V_{DD} = 3.3\text{ V}$ . b) Output voltage and current consumption vs. supply voltage. ....	98
Figure 5-13 a) A photo of the wearable system. b) A photo of the top-side of the NFC tag. ASIC with 3D-EMG-ISFETs is bonded on the bottom side of the tag ('skin side'). A sweat outlet with cotton is attached and extended from the skin side to the front side of the tag through a hole in the tag. c) Corresponding block diagram of the NFC powered sensing tag. ....	99
Figure 5-14 Chronoamperometric readout of the pH sensing 3D-EMG-ISFET (a), and 3D-EMG- $\text{Na}^+$ sensitive FET (b), using NFC communication vs. with Precision semiconductor parameter analyzer (HP 4156). ....	101
Figure 5-15 Readout circuit for channel impedance.....	102
Figure 5-16 Signal generator schematic.....	105
Figure 5-17 Current mirror schematic .....	105
Figure 5-18 Experimental validation of the signal generator and current mode rectifier. ....	106
Figure 5-19 An 8th order current mode LPF, $n = 4$ . ....	106
Figure 5-20 Measurement results from the experimental validation setup. a) Dynamic response of the output current $I_{OF}$ under different gate bias conditions. b) Extracted $I_{OF}-V_G$ sweep compared with the $I_D-V_G$ characteristics of a standalone transistor.....	107





## List of Tables

---

Table 1-1 Typical concentration ranges for common biomarkers in sweat and their diagnostic applications .....	4
Table 3-1. Performance summary of state of the art devices from both un-modified CMOS processes and dedicated non-foundry processes.....	31
Table 3-2. Na <sup>+</sup> concentrations in two sweat samples measured by three 3D-EMG-Na <sup>+</sup> sensors and a commercial Na <sup>+</sup> Meter; pH values of the same samples measured by three 3D-EMG-pH sensors and a commercial pH Meter. Na <sup>+</sup> Meter results were converted from open-circuit-potential readings. ....	56
Table 3-3. State-of-the-Art (SoA) in electrochemical ion sensors.....	57
Table 4-1. Figure of merit comparison table for state of the art sweat sensors integrated with microfluidic channel. ....	62



## List of equations

---

Equation 2.1 .....	15
Equation 2.2 .....	16
Equation 2.3 .....	16
Equation 2.4 .....	17
Equation 2.5 .....	19
Equation 2.6 .....	20
Equation 2.7 .....	23
Equation 2.8 .....	23
Equation 2.9 .....	23
Equation 2.10 .....	24
Equation 2.11 .....	24
Equation 2.12 .....	25
Equation 2.13 .....	25
Equation 4.1 .....	64
Equation 4.2 .....	64
Equation 4.3 .....	70
Equation 4.4 .....	70
Equation 4.5 .....	70
Equation 4.6 .....	71
Equation 5.1 .....	89
Equation 5.2 .....	91
Equation 5.3 .....	103



# Nomenclature

---

Acronym/Abbreviation	Description
3D-EMG-ISFET	Tridimensional Extended Metal Gate ISFET
$(a_A)_{\text{samp}}$	Activity of ion species $A$
AC	Alternating current
$A_c$	Collecting area
ADC	Analog to digital converter
Ag	Silver
AgCl	Silver Chloride
Al	Aluminum
ALD	Atomic layer deposition
$\text{Al}_2\text{O}_3$	Aluminum oxide
AND	CMOS gate, AND
ASIC	Application-specific integrated circuit
B	Bulk terminal of a MOSFET/ISFET device
BEOL	Back End of the Line
BGP	Bandgap reference
BLE	Bluetooth low energy
CA	Chronoamperometry
C.A.	Contact angle
$\text{CaCl}_2$	Calcium chloride
$C_d$	Depletion capacitance
CE	Counter electrode
$C_{\text{Gouy}}$	Gouy-Chapman double layer capacitance
$C_{\text{Helm}}$	Helmholtz double layer capacitance
$C_{\text{in}}$	Input capacitance
CM	Current mirror
$\text{cm}^2$	Area unit, square millimeter
CMOS	Complementary Metal Oxide Semiconductor
CMRR	Common-mode rejection ratio
$C_{\text{ox}}$	Gate oxide capacitance
CPU	Central processing unit
$C_s$	Double layer capacitance
$C_{\text{sens}}$	Capacitance of the sensing layer
CTAT	Complementary to absolute temperature
CV	Cyclic voltammetry
D	Drain terminal of a MOSFET/ISFET device
DC	Direct current

DEC	decoder
dec	Decade of $I_D$
dec[X]	Decade of X's concentration
DI	De-ionized
DNA	Deoxyribonucleic acid
Drain	Drain terminal of transistors
	Drain material to remove droplets, in Chapter 4
DUT	Device under test
$E$	Potential
$E^0$	Standard-state reduction potential
EDL	Electrical double layer
EIS	Electrochemical impedance spectroscopy
$E_{ISE}$	Potential of the ISE
$E_{REF}$	Potential difference between reference electrode and liquid-ISFET interface
$E_{TC}$	Voltage offset due to trapped charges
$F$	Faraday's constant
fA	Current unit, femto-ampere
$f_{cond}$	Conductance variation frequency
$f_{max\_power}$	Frequency of maximum spectrum density
$G'$	The solution-ISFET interface
$G''$	The oxide-semiconductor interface
$G_{ch}$	Channel conductance
$g_{eff}$	Effective gap between the epidermal pore and microfluidic channel
H	Hydrogen
$[H^+]$	Concentration of hydrogen ions
$H_3PO_4$	Phosphoric acid
HAADF	High-angle annular dark-field imaging
$HfO_2$	Hafnium oxide
$i$	Current
$I_D$	Drain current
IMD	Inter-metal dielectric
$I_{off}$	Off current of a transistor
$I_{on}$	On current of a transistor
ISE	Ion selective electrode
ISFET	Ion sensitive field effect transistor
ISM	Ion sensitive membrane
$k$	Boltzmann constant
KCl	Potassium chloride
$l$	Liquid phase
LPF	Low pass filter

LUT	Liquid under test
mA	Current unit, milli-ampere
MIP	Molecularly imprinted polymer
mM	Concentration unit, milli-Molar
mm <sup>2</sup>	Area unit, square millimeter
MOSFET	Metal-Oxide-Semiconductor Field Effect Transistor
MUX	Multiplexer
mV	Voltage unit, milli-Volts
N	Nitrogen
$n$	Slope factor due to capacitive divider in a MOSFET
nA	Current unit, nano-ampere
[Na <sup>+</sup> ]	Concentration of sodium ions
NaCl	Sodium chloride
$n_e$	Mole of electrons per mole of redox reactant
NFC	Near field communication
NH <sub>4</sub> Cl	Ammonium chloride
nL	Volume unit, nano-Liter
nm	Length unit, nano-meter
NOT	CMOS gate, NOT
nS	Conductance unit, nano-Siemens
nW	Power unit, nano-Watt
O	Oxygen
OCP	Open circuit potential
ohm	Resistance unit
-OH	Hydroxyl group
OPA	Operational amplifier
pF	Capacitance unit, pico-Farad
pH	$-\log([H^+])$
pH <sub>pzc</sub>	pH value when the oxide-solution interface is electrically neutral
Poly Si	Polycrystalline silicon
PSRR	Power supply rejection ratio
PTAT	Proportional to absolute temperature
PVC	Polyvinyl chloride
pW	Power unit, pico-Watt
$q$	Elementary charge
$Q$	Reaction quotient
QRE	Quasi reference electrode
$R$	Gas constant
$R_{ch}$	Channel resistance
RE	Reference electrode
Red-ox	Reduction-oxidation

RIE	Reactive ion etching
R-Square	Coefficient of determination
S	Source terminal of a MOSFET/ISFET device
<i>s</i>	Solid phase
$S_f$	Frequency sensitivity of $f_{cond}$ to flow rate
$S_I$	Current sensitivity, unit: dec/dec[X]
Si	Silicon
$\text{Si}_3\text{N}_4$	Silicon nitride
$\text{SiO}_2$	Silicon dioxide
SoC	System on chip
SOI	Silicon on Insulator
SPDT	Single pole, double throw
SPICE	Simulation Program with Integrated Circuit Emphasis
SPST	Single pole, single throw
SRFM	Sweat-rate-to-frequency modulation
SRDC	Sweat-rate-to-duty-cycle
SS	Subthreshold swing
SS-ISE	Solid-state ion selective electrode
$S_V$	Voltage sensitivity, unit: mV/dec[X]
$T$	Temperature in Kelvins
$t$	Time
$t_a$	Minimum time resolution between old and new sweat
$t_F$	Sweat flow start time
$t_f$	Drop formation time
Ti	Titanium
$t_r$	Drop removal time
$t_s$	Sensor response start time
$t_t$	Drop transportation time
$U_T$	Thermal voltage
UV	Ultra-violet
<i>v</i>	Vapor phase
$V_B$	Bulk bias voltage
$V_c$	Volume of the collecting reservoir
$V_D$	Drain bias voltage
$V_d$	Volume of sweat droplet
$V_{DB}$	$V_D - V_B$
$V_{drop}$	Volume of the droplet
$V_{DS}$	$V_D - V_S$
$V_G$	Gate bias voltage
$V_{G'}$	Voltage at the solution-ISFET interface
$V_{G''}$	Voltage at the oxide-semiconductor interface
$V_{GB}$	$V_G - V_B$



$V_{GS}$	$V_G - V_S$
$V_{ref}$	Voltage applied to the reference electrode
$V_S$	Source bias voltage
$V_s$	Volume of the sensing reservoir
$V_{SB}$	$V_S - V_B$
$v_{siv}$	Sweat rate
$V_{th}$	Threshold voltage
$\Delta V_{th}$	Voltage shift of $I_D$ - $V_G$ characteristics curve
WE	Working electrode
$[X]$	Concentration of X
$Z$	Impedance
$z$	Valence of ion
$\mu m$	Length unit, micro-meter
$\mu A$	Current unit, micro-ampere
$\mu L$	Volume unit, micro-Liter



## Greek letters

---

Acronym/Abbreviation	Description
$\alpha$	Sensitivity coefficient
$\beta_s$	Surface buffer capacity
$\gamma$	Grouping of chemically related constant potentials
$\gamma_{sv}$	Surface tension at the solid-vapor interface
$\gamma_{lv}$	Surface tension at the liquid-vapor interface
$\gamma_{sl}$	Surface tension at the solid-liquid interface
$\theta$	Angle
$\theta_{skin}$	Contact angle of the skin
$\Psi$	Potential across the EDL at solution-oxide interface



# Chapter 1 Introduction to Wearable Sweat Analysis

---

This chapter introduces the motivations of this work. A brief introduction to wearable sweat analysis is given in three sections: Real time monitor of health status as a complementary to current healthcare procedures; Sweat as a reliable data mine that provides rich information on health status; Review of state of the art wearable sweat sensors and challenges. Finally, at the end of this chapter, the structural outline of this thesis is presented.

## 1.1 Complementary to Current Healthcare Procedures

Healthcare procedures today are overwhelmed by an inefficient feedback loop which only starts reacting when the illness is already in an advanced state, as shown in Figure 1-1. Most people only contact doctors when they feel noticeable symptoms of sickness (Figure 1-1C), which are significantly delayed signals generated by the body. However, the body releases warning signatures well in advance of symptoms establishment [1]–[3], during the early development stage of an ailment.

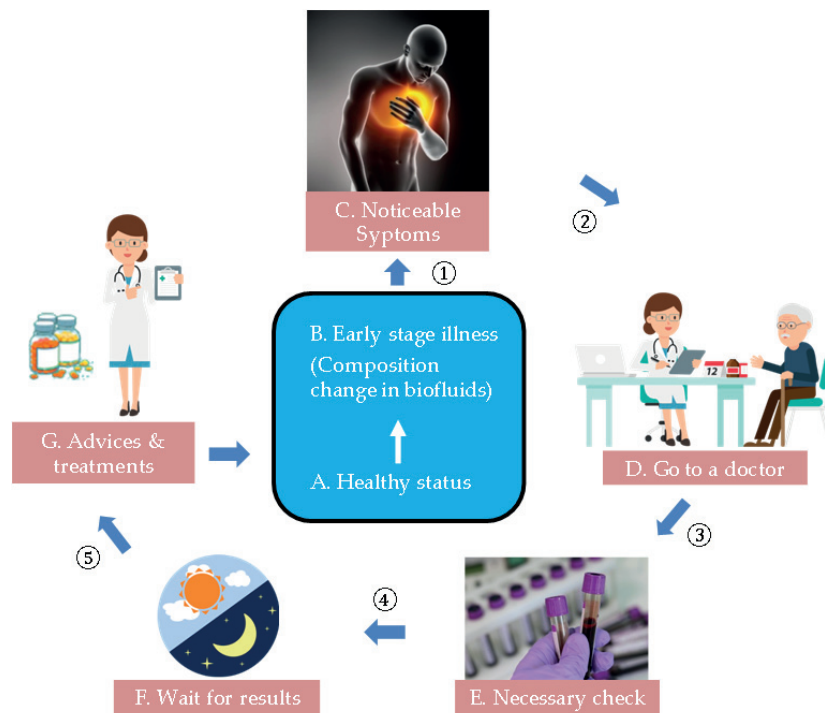


Figure 1-1 Nowadays healthcare procedures

Therefore, in order to allow early identification of potentially preventable conditions, it is of common sense to develop a more proactive healthcare system. For example a system which encourages people to go for regular physical checkups. That is, skipping step C in Figure 1-1, regularly visiting a doctor for a review of the patient’s health history, medications, allergies, and organ systems, as well as a “complete” physical

examination that is sometimes followed by laboratory testing and discussion of health risks [4]. However, it has been evidenced that these visits do not reduce morbidity or mortality [5], [6], but do consume substantial time and resources [7]. Opponents are calling to abandon annual physicals, while the supporters have to suggest less frequency of regular visits for healthy individuals [7]–[10]. In this quagmire of current healthcare procedures, the possibility of implementing point-of-care (POC) systems that enable users to check their own health status at home could manifest itself very well as a complementary. Such a device minimizes the cost of time and resources referred by the arrows ② to ⑤ in Figure 1-1.

Wearable smart watches are nowadays implementing heart rate measurement for physical activity monitoring, besides other functions such as sleep quality, respiration rate, skin temperature and blood oxygen monitoring. For biochemical wearables, portable POC devices to measure glucose concentration in blood have become a standard to monitor patients with diabetes. However, the blood tests are still discrete and time consuming in a way that requires the involvement of manual sample acquisition. Thus only limited information could be extracted about a person's health status with a relatively significant delay.

On top of that, a rapid growth in the need for a new kind of more versatile wearable is seen. This need calls for the wearable devices to provide more comprehensive health information including quantitative analysis of biomarkers' (protein, electrolytes, metabolites, etc.) concentration in bio-fluids, continuously and within minimum time lag. With the help of big data techniques, parsed data could be processed by machine learning algorithms [3], [11], to provide preventive healthcare advices before emergency situations occur.

## 1.2 Sweat as a Rich Data Mine

Among all the candidates of bio-fluids (blood, urine, interstitial fluid, saliva, tears, sweat) for biomarker analysis, blood test is a gold standard for analyzing the health status of a person. However, the collection of blood samples requires professionally sterilized equipment and stands risk of causing infections, hence not the first choice to be integrated in wearables. Non-invasive bio-fluid sampling and sensing methods are highly in demand,

and potential bio-fluid candidates which can be sampled non-invasively are discussed as follows.

**Interstitial fluid** (IF) exists just below the skin, thus can be sampled with minimally invasive methods. Microneedles are fabricated to penetrate the epidermal keratinized layer (the stratum corneum) in a painless way [12], [13]. However, as expressed by [14], “concerns regarding biocompatibility and biodegradation of the microneedles, protection from infection due to usage of needles and other sterility issues will need to be carefully addressed for successful implementation”.

Table 1-1 Typical concentration ranges for common biomarkers in sweat and their diagnostic applications

Category	Biomarker	Concentration range in sweat at surface	Diagnostic application	Ref.
Electrolyte	pH	4-7		
	Na <sup>+</sup>	(10-100) mM	Hyper/hyponatremia, cramp, cystic fibrosis	[15]–[17]
	Cl <sup>-</sup>	(10-100) mM	Cystic fibrosis	[15], [18]
	K <sup>+</sup>	(1-24) mM	Dehydration	[19], [20]
	Ca <sup>2+</sup>	(0.41-12.4) mM	Kidney stone forming	[20], [21]
	NH <sub>4</sub> <sup>+</sup>	(0.5-8) mM	Liver disease	[19], [22]
	Mg <sup>2+</sup>	(0.02-0.6) mM	Cardiovascular disease and muscle contraction	[15], [23]–[25]
Small molecule	Lactate	(5-60) mM	Body exertion, sepsis	[15], [26]
	Glucose	(0.01-0.2) mM	Diabetes management	[27]
	Creatinine	(0.014-0.051) mM	Renal dysfunction	[15]
	Uric acid	(2-10) mM	Renal dysfunction	[20]
	Ascorbic acid	(0.01-0.05) mM	Diabetes	[15], [20]
	Pyruvate	0.003-1 mM	Disorders of energy metabolism	[15]
	Cortisol	(22.1-386) nM	Emotional stress signals	[14]
Peptide	Neuropeptide Y (NPY)	(188-682) fM	Alertness, depression signals	[19]
Protein	Interleukin 6 (IL-6)	(291-654) fM	Inflammation	[19]



**Saliva** sample tests have gained considerable attention as an almost non-invasive alternative to blood tests [28]. Nevertheless, the chemical composition in saliva heavily depends on the previous meal. Thus professional instructions should be followed in order to get a qualified sample for valid information.

**Tear** represents itself as an attractive alternative in the non-invasive wearables family [29]–[31]. However, tear sampling can be uncomfortable and risky. Eye irritation stimulates tear glands and leads to formation of reflex tears, and may thus alter the analyte concentration and lead to false readings. Verily Life Sciences recently put the glucose-sensing part of the smart lens program on hold, due to “demonstrated challenges in achieving the steady state conditions necessary for reliable tear glucose readings” [31].

**Sweat** is another promising type of biofluid that can be sampled and tested non-invasively as well as continuously [20], [32], rendering a plethora of biochemical information in real time. Studies evaluating its capability and reliability in providing useful physiological information on different aspects have been reported. To name a few, type and concentration range of different biomarkers, how different biomarkers signal the health status (Table 1-1), comparison and correlation with other bio-fluids in terms of biomarker composition [19], [27], [33]–[36], different biomarkers’ behavioral correlation in eccrine sweat [18], [37], the partitioning mechanisms from inner bio-fluids [19], its secretion dependent mechanisms [19], heat acclimation dependence of biomarker compositions [38]–[40] and the variation and validity of sweat sample test in different local regions [18].

Nonetheless, in order to fulfill the promising potentials of sweat sensing, more systematic and in depth knowledge of the ‘hard science’ lying between health status and sweat biomarkers is required [41].

### 1.3 State of the Art

There are many opportunities in studying sweat, as well as many challenges. Despite the significant opportunities of sweat to be used as a rich physiological data mine, the many challenges which include the production of enough sweat for analysis, sample evaporation, lack of appropriate sampling devices, errors in results owing to chemical stimulations and biomarker degradation with time, result in high cost and lack of

automation for sweat tests [19], [32], [42], [43]. That is the reason why sweat data exploration methods have been extremely scattered and underdeveloped. Today, with the unprecedented pace of research advances in various fields such as microfluidics, bio-electronics, electrochemical transduction, bio-compatible materials, and wireless communication, many of the aforementioned issues are solved with low cost wearable sensors. The wearable sweat sensors are brought in intimate contact with skin, crafted to be fully automated in sampling/analysis of sweat biomarkers, and streaming of physiological information continuously or on demand to the computational terminal.

Wearable sweat sensors have been developed based on many different electrochemical techniques: potentiometric for direct sensing of electrolytes ( $\text{Na}^+$ ,  $\text{K}^+$ ,  $\text{Ca}^{2+}$  [44]–[46]), potentiometric for indirect sensing of non-charged species (cortisol [47]), amperometric sensing for immunoassays (glucose, lactate [13], [48], [49]), impedance spectroscopy for immunoassays (cortisol [50]), colorimetric sensors for sweat rate monitoring ([51]), etc. In this section, we are going to review state of the art wearable sweat sensing technologies.

Rose et al. [44] reported an adhesive RFID sensor bandage (Figure 1-2) capable of measuring sodium ion concentration in sweat, with a sensitivity of 57 mV/dec for standalone ISE, and 25 mV/dec for the ISE when measured together with the readout circuit. The sensor patch includes a polyimide-copper flexible electronic layer, integrated with a paper-microfluidics layer in order to transport sweat vapor.

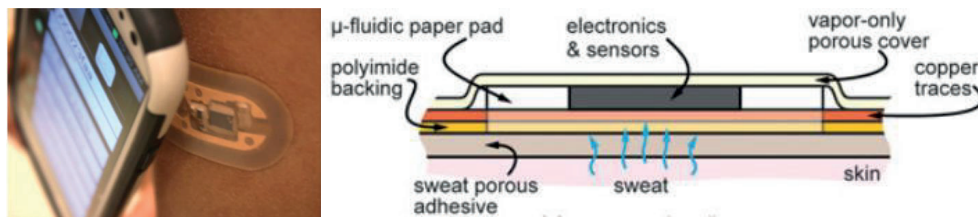


Figure 1-2 Adhesive RFID  $\text{Na}^+$  sensing bandage [44].

Martín et al. [49] realized a wearable sweat-sampling microfluidic system (Figure 1-3) for continuous, real-time monitoring of lactate and glucose concentration. In this system, microfluidic channels are designed so that it allows fast sampling at a flow rate of 20  $\mu\text{L}/\text{min}$ , and real-time streaming of measured data with Bluetooth communication.

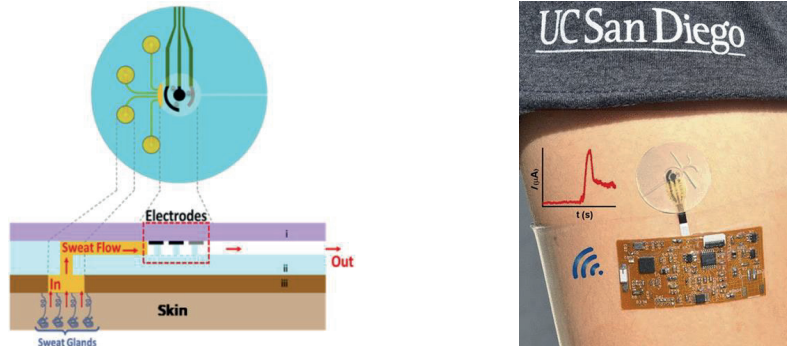


Figure 1-3 Wearable sweat-sampling microfluidic patch for glucose and lactate [49].

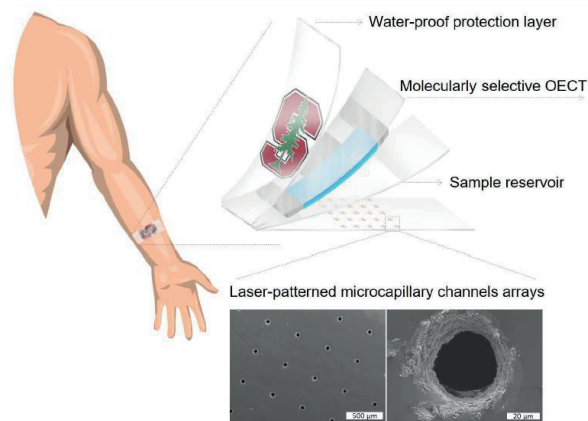


Figure 1-4 Wearable organic electrochemical transistor for cortisol sensing [47].

Parlak et al. [47] developed a sweat sensing patch with organic ISFET and molecularly imprinted polymer membrane, demonstrating an indirect method of sensing cortisol in sweat. A sensitivity of  $2.68 \mu\text{A}/\text{dec}$  was achieved for the cortisol concentration range from 10 nM to 10  $\mu\text{M}$  with in-vitro measurements of artificial sweat.

## 1.4 Challenges

Wearable sweat sensing is still facing a lot of challenges to reach reliability comparable to blood tests.

- Miniaturization of the sensing electrode. Miniaturization brings many issues such as long term stability and high drift rate. The gradual leaching [52]–[54] of membrane materials into the liquid under test, and physical detaching of membrane [55], [56] from the ISEs need to be optimized for long term continuous sweat sensing applications.
- Integration of miniaturized reference electrode. The achievement of a stable of reference electrode under different chemical conditions is a challenge for its miniaturization. This is due to the fact that the space is limited to keep the internal solution which forms a liquid junction to stabilize the junction potential [57]–[61].
- Sampling sweat at very low sweat rate (100 nanoliter per minute per cm<sup>2</sup>) so as to enable continuous monitoring of biomarker signatures [19], [62], [63]. State of the art sweat sensors doesn't offer this capability.
- Real-time continuous monitoring of sweat rate in compensation for sweat-rate related variations in biomarker concentration. [19]
- Data parsing and processing in order to accurately quantify biomarkers in sweat.

## 1.5 Thesis outline

In this thesis, we develop high performance individual blocks for the sweat sensing system. The outline of this thesis is introduced below.

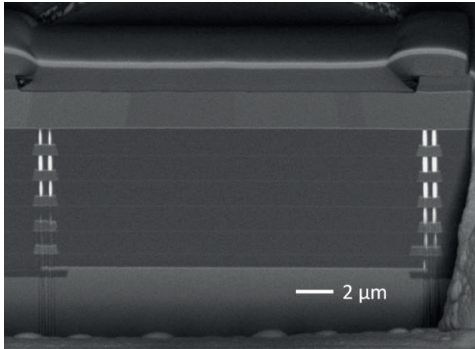
**Chapter 1: Introduction to the importance and challenges of wearable sweat sensing.**

The current chapter presented the motivations and goals of this thesis, and the challenges of state of the art researches in wearable sweat sensors.

**Chapter 2: Categorizing electrochemical methods and rationalize our research into ISFET sensors.**

This chapter categorizes existing electrochemical methods and explains the motivations for exploring potentiometric methods, especially the case of ISFET sensors. Theoretical limits of ISFET sensors are deducted, and serve to evaluate the 3D-EMG-ISFET sensors developed in the next chapter.

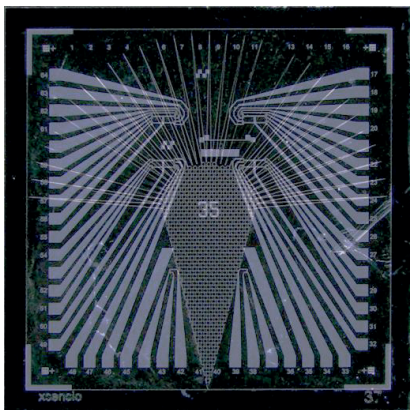
### Chapter 3: Developing and characterizing high performance 3D-EMG-ISFET sensor.



The development of a high performance, low cost, robust, high yield ISFET sensor is presented, characterized through both simulation and measurements. Through modification to the back-end-of-line of a commercial CMOS technology, the results shown in this chapter are, to the best of our knowledge, the first demonstration of

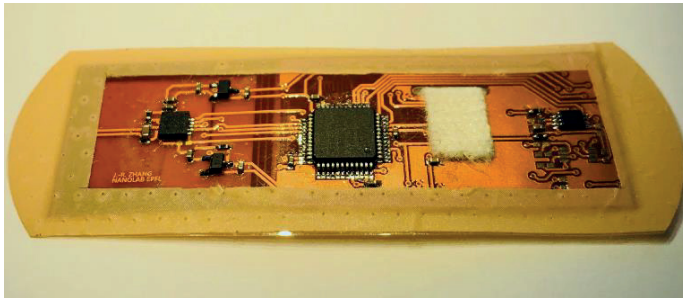
simultaneous multiple ion sensing integrated in an ultra-miniaturized area. Real-time DC measurements and calibrations experiments are carried out to measure unspiked human sweat samples and accuracy is comparable to commercially available ISEs.

### Chapter 4: Wearable passive microfluidics for continuous electronic monitoring of sweat rate.



In a previous work we integrated a hydrophilic passive microfluidic channel with an ISFET sensor chip. In this chapter, we are developing continuous electronic monitor of sweat rate, leveraging the drop-to-drop resolution of this microfluidics. The channel conductance is proved to be a periodical signal, whose frequency and duty cycle closely related to sweat rate, with in-vitro experiments.

## **Chapter 5: Readout circuit for the sensing system, including ISFET sensors and sweat rate sensors.**



In this chapter, we present the last building block of a wearable sweat sensor, i.e. the readout circuit. Readout circuits for the electrolyte sensors (ISFETs) and sweat rate sensors (channel

conductance) are designed and validated with ex-situ experiments.

## **Chapter 6: Conclusions and Outlooks**

The last chapter summarizes the main achievements of this thesis. It also provides a brief outlook of future work to be done in order to deploy a reliable sweat sensing wearable.

## Chapter 2 Electrochemical Methods

---

In the previous chapter, we have seen many electrochemical sensors characterized by various electrochemical analysis methods. To name a few, they include electrochemical impedance spectroscopy (EIS), chronoamperometry (CA), cyclic voltammetry (CV), open circuit potential (OCP), etc. Depending on the transduction principles of the sensing element, they can be applied either independently or coordinately to analyze the chemical condition at the solution-sensor interface as well as in the bulk solution. However, it is still not clearly explained what these methods are, how they are related to / different from each other, and when should we apply them. Individually addressing each of these methods in details is out of the scope of this work. Therefore, we try to make it concise and deliver a systematic overview.

In the first section of this chapter, we briefly introduce the constituting elements of an electrochemical sensor system, in order to have an idea of what the electrochemical analysis methods are. Next, we try to clarify the relationships and differences among electrochemical analysis methods with a family tree, so that the audiences will easily find their way out whenever they come across a new electrochemical analysis case. Then, in order to draw the readers' attention back to the title of this thesis, we highlight one of the electrochemical analysis methods, the potentiometric method, by introducing its easy implementation principle and evolvement in miniaturization. Finally, through comparison between two popular potentiometric methods, we rationalize our research into ISFETs.

## 2.1 Electrochemical Sensing System

As shown in Figure 2-1, an electrochemical sensing system usually consists of electronic control and measurement instruments, bulk solution, a reference electrode (RE), a working electrode (WE), a counter electrode (CE, connected to RE in a 2-electrode system), and the solution to electrode interface. The bulk solution contains biomarkers of interest. Some of the biomarkers are electrically charged (e.g. ions, proteins, etc.), while others are not (e.g. glucose, lactate, etc.). The interface is formed due to diffusion as well as chemical reactions. It exists on all of the three electrodes. However, the most important interface for transduction performance is the interface between biomarkers and the bio/chemical recognition element that performs chemical to electronic transduction.

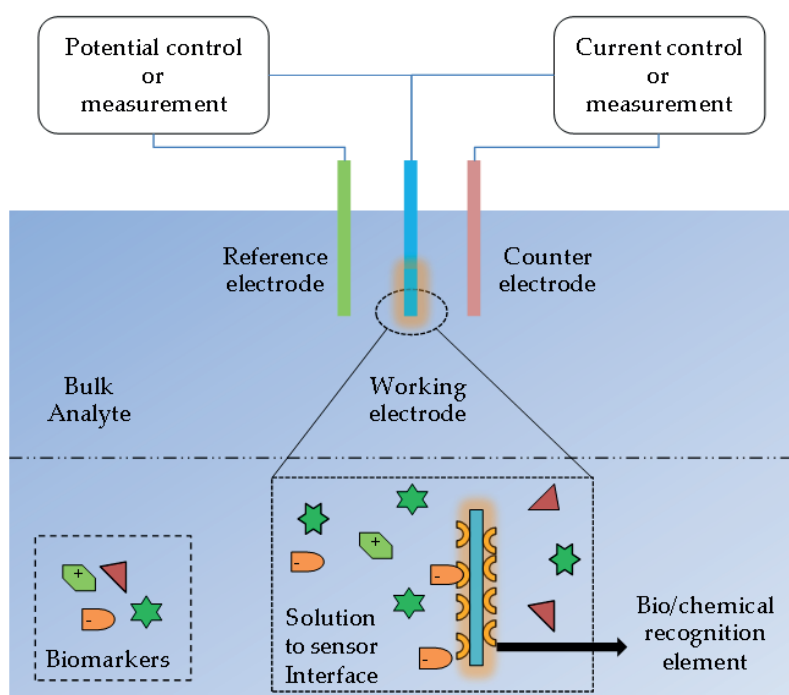


Figure 2-1 Constituents of a typical three-electrode electrochemical sensing system.

The RE is constructed with a chemically stable half-cell, producing stable potential over time. It is used to apply a stable bias voltage to the solution under test, in order to



maintain a controlled environment for the electrochemical reactions. WE is where the electrochemical reactions take place. CE allows the circulation of free electrons from/to the working electrode.

Various electrical methods (introduced later) can be used to stimulate and characterize the electrochemical reactions. There are very different methods, but one thing is in common, that the electrochemical reaction generates a current flow from the instrument through the working electrode into the bulk solution. However, this is only half way of the journey, the current has to be directed back into the instrument again. Furthermore, the current through RE should be kept low to ensure stability. Therefore, the system needs a third electrode, in order to form a complementary path for the current to flow. This electrode is called the counter electrode, or the auxiliary electrode. The above mentioned current path can be reversed, but the reasoning for the need of a complementary path stays the same. Remember that whenever an oxidation (reduction) takes place at the WE, there is a reduction (oxidation) taking place at the CE. Hence, an important requirement for the CE is that its reduction-oxidation products will not interfere with the electrochemical process at the WE.

On the contrary, there are many considerations for the design of a WE. Its surface is functionalized with bio/chemical recognition element (Figure 2-1: inset), in order to selectively react (physically, chemically, or both) with the biomarker under study. The solution to electrode interface is formed due to drift, diffusion, chemical reactions, as well as the liquid flow. It exists on all of the three electrodes. However, the most important interface for biomarker analysis is the interface between biomarkers and the WE, where bio/chemical recognition elements perform chemical-to-electrical transduction.

The chemical-to-electrical transduction reactions can be either electrostatic (e.g. in potentiometry), or reduction-oxidation (red-ox) initiated. Depending on the type of reaction at the interface, and what information is required, various control and measurement instruments can be integrated to design different electrochemical analysis experiments.

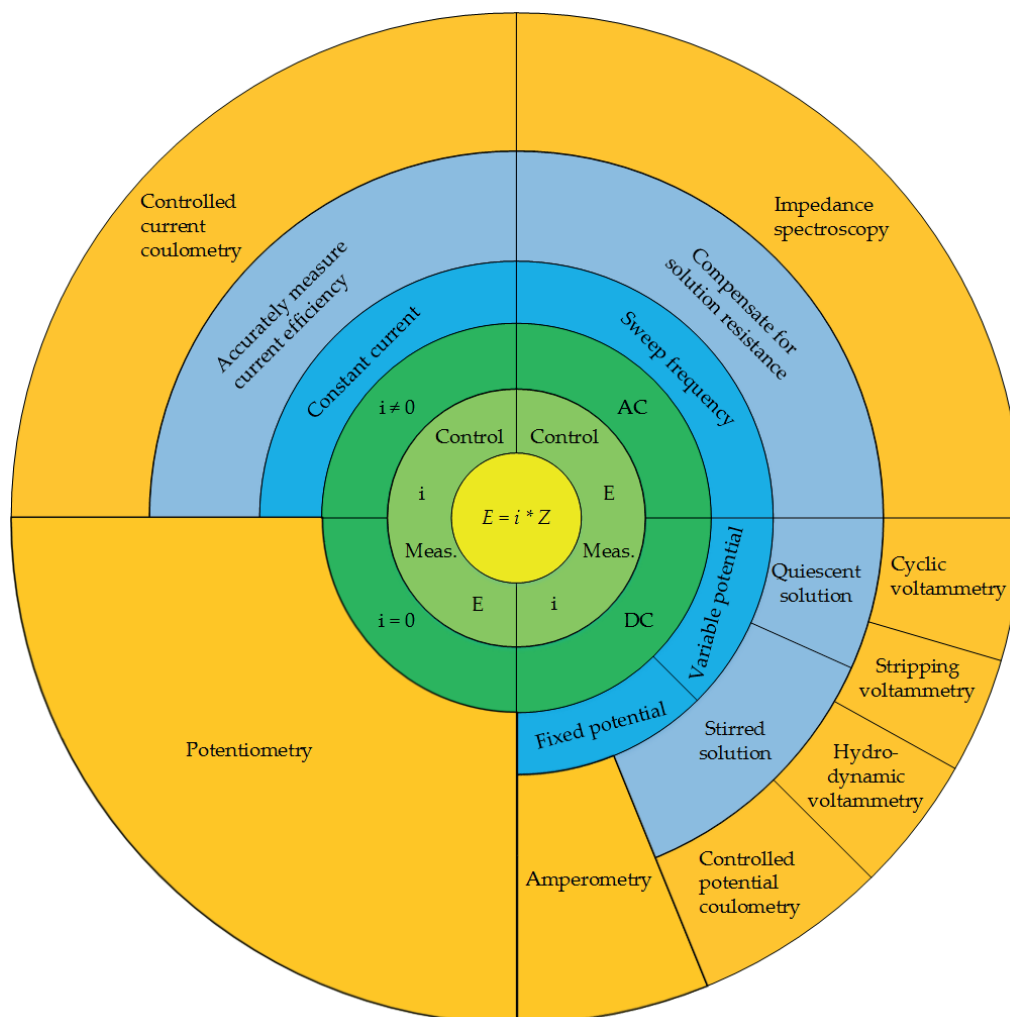


Figure 2-2. Family tree of electrochemical analysis methods. Different blocks distinguish different experimental conditions or analysis methods. The area of them doesn't stand for percentage in any sense. The thickness of the outer ring (orange) stands for the complexity of each method: thicker orange ring means a simpler implementation. Current efficiency is defined in ref [64, p. 3].

## 2.2 Classification of Electrochemical Methods

As mentioned earlier, since there are too many different craftily designed experiments for electrochemical analysis, it is better to first have a clear plot of their relationships. The fundamentals of electrochemical analyzing methods lie in the interpretation of two types of analytical signals: potential and current, with the aid of Ohm's law.

Equation 2.1

$$E = i * Z$$

Where  $E$  is the potential of WE with respect to RE,  $i$  and  $Z$  are the current and impedance through WE and bulk solution. It might be confusing here, that Equation 2.1 somehow seems not completely valid. However, since the potential of the bulk solution is stabilized by the RE, it is sometimes required to compensate for the solution resistance [65].

With the Ohm's law in mind, the three-electrode system can be seen as a black box that exhibits certain impedance, we only have two ways to analyze its characteristics: either apply a controlled potential and study the corresponding current, or apply a controlled current and study the corresponding potential.

Figure 2-2 provides one version of a family tree starting from the Ohm's law, branching through different experimental conditions, and terminating with the corresponding electrochemical techniques. Among the experimental conditions under our control are the potential or the current, analyzing in time domain or frequency domain, and whether we stir the analytes' solution or not. We can also get a direct impression on the implementation complexity of each method from the Figure 2-2. For example, potentiometric technique is the simplest one, since there isn't any experimental conditions requirement besides keeping  $i = 0$ . While controlled potential coulometry is more complicated than amperometry due to the need of stirring the solution in order to minimize the electrolysis time. Therefore, the implementation complexity of a method can be read intuitively from the thickness of the orange ring in Figure 2-2, i.e. thicker orange ring means simpler implementation.

## 2.3 Potentiometric Methods

In wearable applications, the system implementation solution inevitably requires an optimization of system complexity and power consumption. Thus, the lower complexity electrochemical analysis methods such as potentiometry and amperometry are more favorable in this situation. Indeed, a majority of wearable chemical sensors were developed with them [44], [45], [48], [66], [67]. In this section, we are going to introduce the potentiometric method.

### 2.3.1 Nernst Equation and Ion-Selective Electrodes (ISEs)

Potentiometric methods were first implemented just after the derivation of Nernst equation (Equation 2.2) from Gibb's free energy in 1889 [68], [69].

Equation 2.2

$$E = E^0 - \frac{RT}{nF} \ln(Q)$$

It relates the potential of an electrochemical cell/half-cell to temperature and the activity (approximately equal to concentration under some restrictions [3]) of electroactive species. In this equation,  $E^0$  is the standard-state reduction potential,  $R$  is the gas constant,  $T$  is the temperature in Kelvins,  $n$  stands for the mole of electrons per mole of redox reactant,  $F$  is the Faraday's constant, and  $Q$  is the reaction quotient. Notations are written following the convention of electrochemistry. Readers with a physics background may prefer another form of the Nernst equation

Equation 2.3

$$E = E^0 - 2.3 \frac{kT}{nq} \log(Q)$$

Where  $k$  is the Boltzmann constant,  $q$  is the elementary charge.

A majority of the potentiometric sensing family implement ion-selective electrodes (ISEs). Shown in Figure 2-3 is a systematic diagram of a typical potentiometric cell measuring the potential difference between an ISE and an RE. Although ISE has been developed to very simple forms (going to be discussed later in this section and used in the following chapters), it was originally a complex integration of RE, internal solution with known concentration of the ion ( $A$ ), and an ion-selective membrane (ISM), immersed in a sample solution with the ion ( $A$ ) at an unknown activity of  $(a_A)_{samp}$ . With the same principle as that of a chemical cell, the activity difference between inner solution and sample solution in contact with the ISM, gives rise to a potential difference at the membrane interface. In this way, as expected, the ISE, acting as the WE, is responsible to transducing the ion's activity  $(a)_{samp}$  into potential ( $E_{ISE}$ ) of the ISE. While as introduced before, the RE has a known stable potential. We can derive  $E_{ISE}$  to be a Nernst-like equation (Equation 2.4)

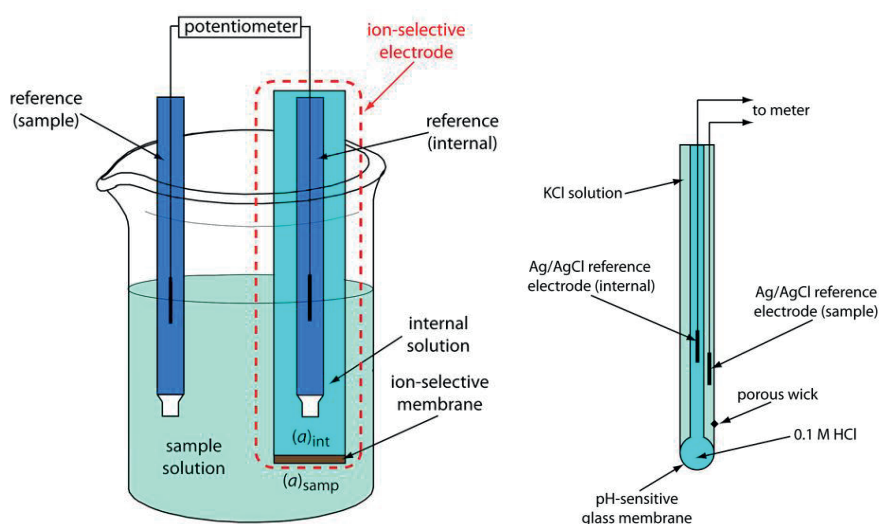


Figure 2-3 Schematic diagram showing a typical potentiometric cell with an ion-selective electrode. The ion-selective electrode's membrane separates the sample, which contains the analyte at an activity of  $(a_A)_{samp}$ , from an internal solution containing the analyte with an activity of  $(a_A)_{int}$ . [70, p. 2]

Equation 2.4

$$E_{ISE} = C + 2.3 \frac{kT}{zq} \log((a_A)_{samp})$$

Where  $z$  is the valence of the ion  $A$ .  $C$  is a constant that takes in to account the interfacial potentials of the two reference electrodes and the ion's activity in the internal solution, as well as other interface-dependent constant potentials. From this equation, it can be concluded that the potential of an ISE is proportional to the logarithmic value of the ion's concentration as well as inversely proportional to the valence of the ion under study.

Thus, there is a theoretical value for the sensitivity of an ISE, which is characterized by the change in  $E_{ISE}$  (i.e.  $\Delta E_{ISE}$ ) per decade of variation in ion concentration. It is called the Nernstian limit, and its value is  $\frac{59.2}{z}$  mV/dec at room temperature (300 K).

### 2.3.2 Solid State ISEs (SS-ISEs)

Conventional ISEs need internal RE and internal solution, making it difficult to implement in miniaturized and cost effective systems. That is where SS-ISEs drew the attention [71]–[73]. In SS-ISEs, metal wire or other solid state conductive materials (SSCM) such as glassy carbon and doped silicon are coated with ISMs or simply oxide: one side of the ISM in contact with the SSCM, the other side in contact with the sample solution (Figure 2-4a). The principle of both ISM and oxide SSCM ISEs are rather similar in terms of buffering the targeted ion, here we briefly introduce that of oxide coated ISEs.

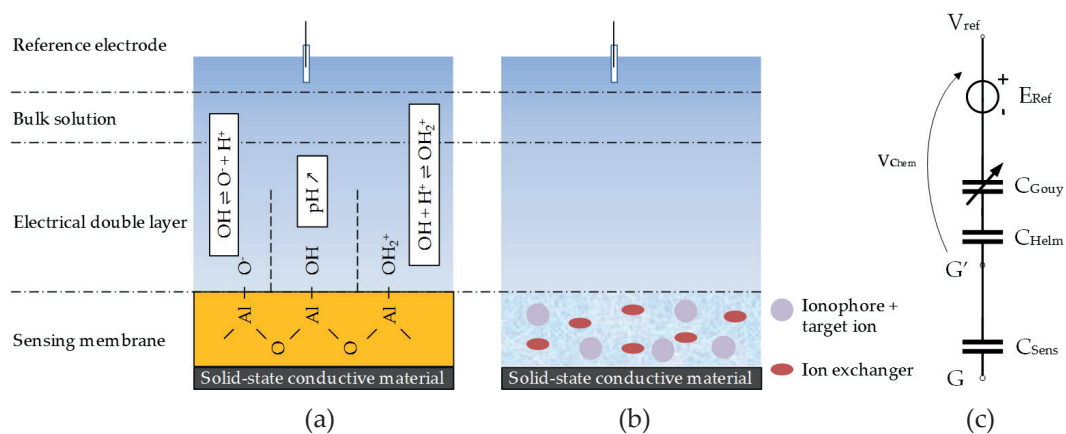


Figure 2-4 a) An example of a SS-ISE coated with oxide for pH sensing:  $Al_2O_3$  sensing layer is in contact with a sample solution of certain pH. b) An example of a SS-ISE coated with ISM for charged ion sensing. c) Equivalent circuit schematic of SS-ISEs in potentiometric measurement.

Although initially prompted by an interest in the coagulation and rheological behavior of colloidal suspensions, the research into the interface between metal oxide and aqueous electrolyte (Oxide-Solution) resulted to be useful for ion sensing as well. In the beginning, researchers presumed a Nernstian behavior across the electrical double layer (EDL) at the oxide-solution interface, which related the total potential drop across the EDL to the  $H^+$  (or  $OH^-$ ) activity in the bulk solution. However, this was proved incomplete with the site-binding model proposed by Yates et al. [74]. The site-binding model suggested that with pH changing from acidic to basic, the oxide-solution interface changes from positively charged ( $OH_2^+$ , protonized) to negatively charged ( $O^-$ , deprotonized) (Figure 2-4a). Further study accredited the ability to form  $OH_2^+/O^-$  surface charge groups to a value  $\beta_s$ , which is then named surface (proton) buffer capacity.  $\beta_s$  is related with surface potential  $\Psi$  through the double layer capacitance ( $C_s$ ), which is mainly determined by the ion concentration of the bulk solution. Finally, these studies resulted in a simple modified Nernst equation [75], describing the potential  $\Psi$  across the EDL at solution-oxide interface.

Equation 2.5

$$\Psi = 2.3\alpha \frac{kT}{q} (\text{pH} - \text{pH}_{\text{pzc}})$$

Where  $\alpha = \frac{1}{(2.3kT/q^2)(C_s/\beta_s)+1}$ ,  $\text{pH}_{\text{pzc}}$  is the pH value when the oxide-solution interface is electrically neutral. Therefore, only when the oxide exhibits a large  $\beta_s$ , and immersed in a solution with low ion concentration (small  $C_s$ ),  $\alpha \approx 1$ , the surface potential is related to the bulk pH by  $2.3 \frac{kT}{q}$  per pH unit (Nernstian limit,  $\sim 59.2$  mV/pH at 25 °C). Otherwise when  $\alpha < 1$ , the oxide-solution interface exhibits a sub-Nernstian response.

Same derivation is applicable to achieve sensitivity for an ISM-to-solution interface, where the ISM is engineered to exhibit selectively high buffer capacity for a specific charged species (ions, charged molecules, etc.). And this resulted in SS-ISEs without an internal solution and internal RE (Figure 2-3b). Combining Equation 2.4 and Equation 2.5, the potential difference from the RE to an SS-ISE immersed in the same solution can be written as

Equation 2.6

$$V_{Chem} = \gamma - 2.3\alpha \frac{kT}{zq} \log((a_A)_{samp})$$

Where  $\gamma$  is a grouping of chemically related constant potentials that includes the interface potentials at the reference electrode. The equivalent circuit of the SS-ISE in potentiometric measurements is shown in Figure 2-4c.

### 2.3.3 Ion Sensitive Field Effect Transistors (ISFETs)

The invention of ISFETs [76] is almost at the same time when researchers started to consider the reasons of sub-Nernstian response at oxide-solution interface [74], [77]. Indeed, ISFETs and ISEs are close relatives, in the sense that the electrochemical transduction principles at the interface are essentially the same. In order to make a quick impression to the readers about the relationship between ISFETs and ISEs, an ISFET can be understood as an ISE connected to the gate terminal of a MOSFET. Therefore, in order to have a better understanding of ISFET, it is necessary to briefly introduce MOSFET, which is a purely electronic device with 4 terminals (drain, source, gate, and bulk in Figure 2-5a). There are different types of MOSFETs, we take the most common one (n-type MOSFET) as an example to explain the basics that is related to the ISFET application. For more detailed principles regarding MOSFETs, the readers are referred to [78]. Shown in Figure 2-5a is the structure of a typical n-type MOSFET. It consists of a bulk (pink) which is silicon with light doping of acceptors, symmetrical source / drain region (orange) which is silicon with heavy doping of donors, a gate oxide layer (blue) serving as insulator where the “field effect” is applied. Each terminal is connected electrically through one or more conductive layers (metal layer and polysilicon layer in this case). By applying a voltage  $V_G$  on the gate metal, the electrical field across the gate oxide is controlled by the voltage difference between  $V_G$  and  $V_S$  ( $V_{GS}$ ). The electrical field repels the positively charged carriers in the bulk (although the real principle is more complicated). Thus when  $V_{GS}$  is above a threshold  $V_{th}$ , the channel in Figure 2-5b is depleted and affinitive to negatively charged carriers (electrons). As  $V_{DS}$  increases, the electrons will fill the channel and generate a current  $I_D$  through from drain to source (Figure 2-5d).



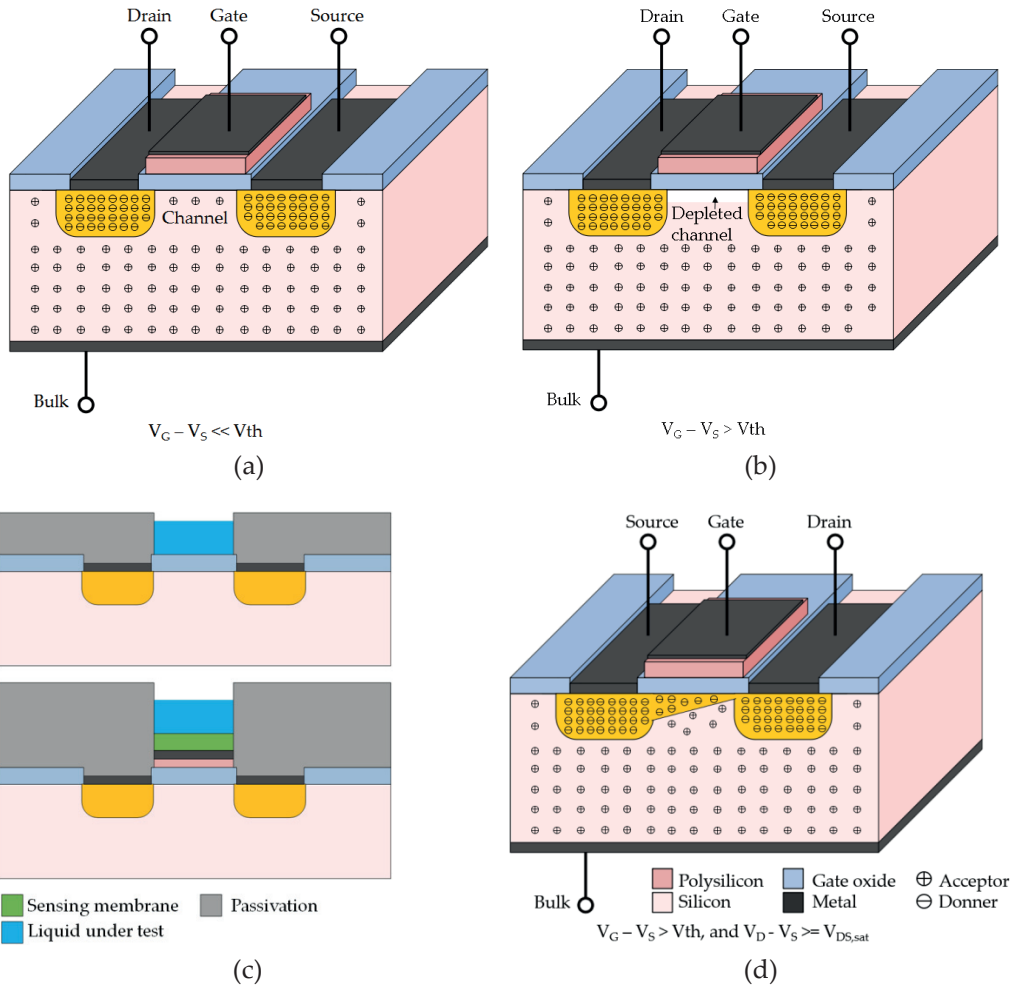


Figure 2-5 a) A typical n-type MOSFET. b) The channel of an n-type MOSFET is depleted. c) Two drawings of typical ISFETs, constructed by combining SS-ISE and MOSFET techniques. d) An n-type MOSFET working in saturation, conducting a current from drain to source.

### 2.3.3.1 ISFET, ISE and capacitance divider model

There is another working mode of MOSFETs called the subthreshold conduction mode, namely,  $V_{GS}$  is smaller than  $V_{th}$ . Later we will briefly introduce several key parameters of it. However, it is now a good time to draw the readers' attention back to the ISFETs. No

matter in which mode is the MOSFET working, a simple law is that the  $V_{GS}$  can modulate  $I_D$ . Interestingly, we learnt that the surface potential of ISEs is keen to vary with the concentration of target ions in the solution. Thus it is logical to integrate a SS-ISE into the MOSFET structure, by two means: *i.* cover the gate metal with sensing membrane (ISM, oxide, etc). *ii.* remove the polysilicon and metal over the gate, and use the combination of gate oxide + bulk as a SS-ISE. When the new device is immersed in liquid (Figure 2-5c),  $I_D$  is correlated with  $V_G$  which is directly affected by different target ion concentrations. This new device is called ISFET.

Above all, an ISFET can be viewed as a SS-ISE connected in series with the gate of a MOSFET.

Shown in Figure 2-6 is the schematic of an equivalent capacitance divider model, modeling the electrical behavior of an ISFET, including both solution phase and semiconductor phase. It includes the equivalent circuit model of an SS-ISE as shown in Figure 2-4c, as well as the voltage offset introduced by trapped charges in the gate oxide and sensing membrane layer ( $E_{TC}$ ), and the model of a MOSFET. In the inset, the MOSFET model is further simplified into a series of gate oxide capacitance ( $C_{ox}$ ) and surface depletion capacitance ( $C_d$ ). This simplification is useful for the determining of ISFET's sensitivity.

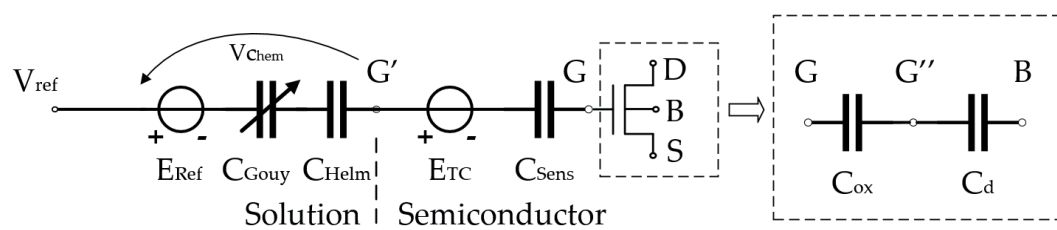


Figure 2-6 Schematic of a capacitance divider model that models the electrical behavior of an ISFET. Inset: simplified capacitance divider to model the MOSFET.

From Figure 2-4 and Equation 2.6, we know that the potentiometric sensitivity of SS-ISEs appears at the interface  $G'$  as a voltage variation of  $V_{G'}$ . During standard open circuit potential (OCP) measurement experiments, the voltage  $V_G$  at the interface  $G$  equals  $V_{G'}$ . However, in the case of an ISFET, as shown in Figure 2-6,  $V_G$  is determined by

Equation 2.7

$$V_{GB} = \left( V_{ref} - \gamma + 2.3\alpha \frac{kT}{zq} \log((a_A)_{samp}) - E_{TC} \right) \frac{C_{Sens}}{C_{Sens} + (C_{ox}C_d/(C_{ox} + C_d))}$$

Where  $V_{GB} = V_G - V_B$ .

Capacitance divider model of the MOSFET oxide-channel interface leads to further degradation of the sensed signal. The voltage variation at the interface  $G''$  reflects the actual sensitivity of an ISFET, and is derived as follows

Equation 2.8

$$V_{G''B} = \left( V_{ref} - \gamma + 2.3\alpha \frac{kT}{zq} \log((a_A)_{samp}) - E_{TC} \right) \frac{C_{Sens}}{C_{Sens} + (C_{ox}C_d/(C_{ox} + C_d))} / n$$

Where  $n$  is a slope factor defined by

Equation 2.9

$$n = 1 + \frac{C_d}{C_{ox}}$$

From Equation 2.8, sensitivity of ISFET is highest when  $C_{sens}$ ,  $C_{ox}$  are maximized and  $C_d$  minimized.

### 2.3.3.2 Subthreshold conduction mode

The ISFET's drain current  $I_D$  is a multi-function of  $V_{ref}$  and the solution-sensor interface. According to MOSFET's principle, it is preferred to bias the ISFET into a work mode called subthreshold conduction mode, due to the interest in exploiting log-domain computation featuring low power consumption and high dynamic range [79]. In subthreshold (or weak inversion) mode, MOSFET's  $V_{GS}$  is slightly smaller than the threshold voltage  $V_{th}$ , thus the drain current  $I_D$  is usually considered to be 0. However, it is

not 0 due to diffusion and recombination of the minority carriers [78]. Instead,  $I_D$  is exponentially dependent on the terminal voltages as follows [80]:

Equation 2.10

$$I_D \propto e^{V_{GB}/nU_T} (e^{-V_{SB}/U_T} - e^{-V_{DB}/U_T})$$

Where  $U_T$  is the thermal voltage.

The exponential dependency of  $I_D$  over  $V_G$  leads to the famous definition of subthreshold swing (SS), which is a critical parameter that symbolizes the power consumption of a FET-type device. By definition

Equation 2.11

$$SS = \frac{dV_G}{d[\log(I_D)]} = 2.3U_T \cdot n$$

This definition leads to a conclusion that, under room temperature (300 K, 25 °C), as long as  $C_d$  and  $C_{ox}$  have the same sign,  $SS \geq 59.2$  mV/dec (59.2 millivolts variation in  $V_G$  when  $I_D$  is varied by 10 times). This is a feature that should be clearly distinguished from the Nernstian limit discussed in Equation 2.4. Low SS is desired for a FET based device, since it fundamentally results in low power consumption [81].

### 2.3.3.3 Theoretical limits for ISFET sensitivity

The sensitivity of an ISFET is defined in two ways.

Voltage sensitivity (unit: mV/dec[X])

Equation 2.12

$$S_V = \frac{dV_{G''}}{d[\log((a_A)_{\text{samp}})]} = 2.3\alpha \frac{kT}{zqn}$$

Current sensitivity (unit: dec/dec[X])

Equation 2.13

$$S_I = \frac{d[\log(I_D)]}{d[\log((a_A)_{\text{samp}})]} = \frac{dV_G}{d[\log((a_A)_{\text{samp}})]} \frac{d[\log(I_D)]}{dV_G} = \frac{\alpha}{zn}$$

Where dec stands for decade-of- $I_D$ -variation, dec[X] stands for decade-of-target-ion-activity change. Therefore the  $S_V$  has a theoretical maximal value which is the Nernstian limit, and the theoretical maximum of  $S_I$  is  $\frac{1}{z}$ , given two conditions are fulfilled at the same time: *i.* the surface buffer capacity  $\beta_s$  in Equation 2.5 is infinitely high; *ii.* the slope factor  $n$  is equal to 1.

### 2.3.4 ISEs vs. ISFETs

The slope factor introduced by the capacitance divider model is an interesting feature shedding light on the advantages of ISFETs over standalone SS-ISEs, due to the existence of similar non-idealities (capacitance divider effect) with ISEs when they are integrated with a differential amplifier for the readout of voltage variations. We are going to discuss about this in the following.

Operational amplifier readout is a commonly adopted solution [45], [48] when developing wearable ISE readout circuits. A typical configuration is utilizing a differential amplifier to measure the voltage difference between  $V_{\text{ref}}$  and  $V_G$ , as shown in Figure 2-7. However, a well-designed amplifier requires a large input transistor pair [82], which inevitably introduces large input capacitance in the order of several pico Farads 3 pF [48], or more 11 pF [45]. This capacitance is usually not a problem in the applications of standalone ISEs, where electrode sizes of around 10 mm<sup>2</sup> (large  $C_{\text{sens}}$ ) are adopted. Nevertheless, in wearable sensing systems where integration of a larger array of sensors is required, sensor size of about 100  $\mu\text{m}^2$  or less is desired [83]–[85]. In these cases, the capacitance of the

sensing layer  $C_{\text{sens}}$  becomes smaller than the input capacitance  $C_{\text{in}}$ , resulting in more than 50% degradation of the sensed signal. The degradation of readout sensitivity has been reported by [44] when developing a wearable  $\text{Na}^+$  sensor with a standalone SS-ISE (standalone: 57 mV/dec; readout: 25 mV/dec). ISFETs are more desirable than standalone ISEs, due to the flexibility of optimizing the size of the underlying MOSFET as well as less parasitic capacitance thanks to the highly compact structure of ISFET.

Another advantage of ISFETs is that they directly convert the high impedance output terminal of an ISE into a low impedance output terminal. This conversion makes it less susceptible to noise [86] in the environment such as electromagnetic interference, therefore eliminating the need to shield the signal lines.

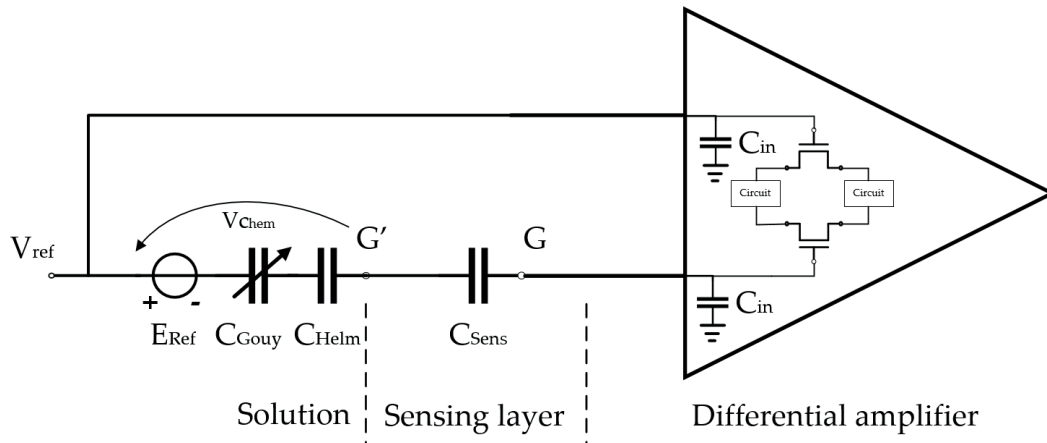


Figure 2-7 Differential amplifier readout configuration for ISE potentiometric sensing.

## 2.4 Summary

In this chapter, we first categorized the existing electrochemical sensing methods, in an family tree to intuitively show the relative complexity amongst them. With this family tree, we rationalized the motivations for exploring potentiometric methods. Next, we introduced the principles of potentiometric methods and conventional ISEs. Finally, we introduced the ISFETs and their performance limit. By comparing the similarity of ISFETs

and ISEs, we summarized the advantages of using ISFETs instead of ISEs in wearable applications where miniaturization is highly demanded.





## Chapter 3 3D-Extended-Metal-Gate-ISFET

---

ISFETs form a very attractive solution for wearable sensors due to their capacity for ultra-miniaturization, low power operation and very high sensitivity, supported by CMOS integration. ISFETs made ad hoc in laboratory clean rooms show excellent results in terms of sensitivity, but their production is expensive and the yield is often low. On the other hand, when reported ISFETs adopt unmodified CMOS process flow, they achieve high yield and high robustness, however, the performance of the sensing devices is rather limited.

This chapter introduces a high performance, high yield, high robustness ISFET, 3D-Extended-Metal-Gate ISFET (3D-EMG-ISFET), realized by the post-processing of a conventional 0.18  $\mu\text{m}$  CMOS technology node. In the first section, the 3D-EMG-ISFET is demonstrated with its performance in pH sensing. Afterwards, we introduce the detailed processing steps, including a method to eliminate the device-to-device variations. Then, ISMs are casted on the devices, making them sensitive to different cations ( $\text{Na}^+$ ,  $\text{K}^+$ ,  $\text{Ca}^{2+}$ ). Finally, we conclude this chapter with a table, benchmarking the performances of our 3D-EMG-ISFET to state of the art. Part of the work in this chapter has been published in IEEE International Electron Devices Meeting (IEDM) 2018 [87] and ACS sensors [88].

The processing steps of fabricating MOSFETs into 3D-EMG-ISFETs are developed by Mr. Francesco Bellando and Ms. Maneesha Rupakula, the sensor characterization setup is developed by Dr. Fabien Wildhaber, the ISMs cocktails are prepared by Dr. Johan Longo. The author's contribution is the idea of using commercial CMOS process to fabricate high performance ISFET sensors, design of sensor ASICs, HSPICE simulation of the behavioral model, development of method to eliminate the device-to-device variation, as well as experimental characterizations.

### 3.1 Introduction

The most common device architectures for wearable sweat sensors are based on standalone Solid State Ion-Selective Electrodes (SS-ISEs) [44], [46], [48], [89], [90]. However, they usually have a large form factor (on the order of millimeters). Thus, a large number of such electrodes in a sensor array could inhibit system integration. Moreover, due to their large size, they require the collection of relatively large amount of biofluid to cover the whole sensor area. Other considerations are related to electrical performance degradation introduced in Sections 2.3.3 and 2.3.4. When SS-ISEs are scaled down: *i.* their high output impedance makes them more susceptible to noise. *ii.* the usual voltage amplifier readout schemes degrade the sensitivity due to non-ideal capacitance divider effect. In contrast, ISFETs are very scalable as they are based on advanced CMOS technologies [91], offer ultra-low power operation [92] and large scale integration of functionalized sensor arrays with multiple metabolite and parameters detection capability [93]–[96]. Further, due to their small size, they require much lower sample volume and can be easily integrated with microfluidic channels [62]. E. Stern et al. [97], demonstrated label-free detection of femtomolar concentrations of antibodies as well as real-time monitoring of the cellular immune response. C. Toumazou et al. [84] in 2013, developed an ISFET-based simultaneous DNA amplification and detection sensor array. F. Bellando et al. [98] reported in 2017, an ultra-thin body SOI ISFET sensing array that enable nanoWatt sweat sensing together with a passive microfluidic channel, for sweat volume down to nanoliter range. All these previous works and demonstrations support the unique advantages of ISFETs as integrated biosensors and motivate the developments reported in this work.

Nevertheless, the fabrication of high performance ISFETs requires dedicated non-foundry processes, which has the drawbacks of high cost, low yield, low robustness and difficulty of integration, especially when multi-analyte sensing is required. Having this in mind, commercial CMOS process has been exploited in its Back-End-of-the-Line (BEOL) for more than 2 decades [99]–[104], in order to realize cost-efficient, high performance ISFETs (CMOS ISFETs fabricated in un-modified CMOS processes). However, the performance of CMOS ISFETs is limited in terms of low sensitivity, spread in threshold voltage ( $V_{th}$ ), drift rate and power consumption. (Table 3-1 summarizes key performances of state of the

art CMOS ISFETs in comparison with ISFETs fabricated with dedicated non-foundry process flow).

Even so, thanks to the aforementioned irreplaceable advantages, researchers are still striving hard [104] to remedy CMOS ISFETs' poor performances, at the cost of system complexity and power consumption. Thus, it will be extremely interesting to have an ISFET sensor that resolves the cost, yield, robustness versus performance dilemma from device level.

In the next section, we present the fabrication process of a high performance, high yield, high robustness, low cost, tridimensional Extended Metal Gate ISFET (3D-EMG-ISFET) for pH and multi-analyte ( $\text{Na}^+$ ,  $\text{K}^+$ ,  $\text{Ca}^{2+}$ ) sensing.

Table 3-1. Performance summary of state of the art devices from both un-modified CMOS processes and dedicated non-foundry processes

Fabrication technology	Sensitivity (mV / pH)	Drift Rate (mV / h)	Vth Spread (V)	Min. Power per Sensor	Device dimensions ( $\mu\text{m}$ )
0.35 $\mu\text{m}$ CMOS ISFET sensing with $\text{Si}_3\text{N}_4$ [105]	9.2	30	$1.5 \pm 0.9$	20 $\mu\text{W}$ *	5 x 0.35
0.35 $\mu\text{m}$ CMOS ISFET sensing with $\text{Si}_3\text{N}_4$ [103]	26.95	5.8	$-3.3 \pm 6$	NG	10 x 10
0.18 $\mu\text{m}$ CMOS ISFET sensing with $\text{Si}_3\text{N}_4$ [102]	26.2	NG	NG	NG	10 x 10
FinFET sensing with $\text{HfO}_2$ [91]	57	0.3	NG	3 nW *	8 x 0.04 x 0.12
SiNW sensing with $\text{HfO}_2$ [106]	55.3	1.88	NG	NG	10 x 0.2 x 0.2
ISFET sensing with $\text{Al}_2\text{O}_3$ [107]	56	0.3	NG	NG	1000 x 100
<b>This work (0.18 <math>\mu\text{m}</math> CMOS ISFET)</b>	57.2	0.67	$0.354 \pm 0.028$	2 pW	10 x 20

NG: Not Given

\* Calculated from published figures.

### 3.2 Fabrication and Post-processing

The 3D-EMG-ISFETs are fabricated by post-processing MOSFET devices designed in a commercial 0.18  $\mu\text{m}$  CMOS technology [108]. The gate of the MOSFET ( $10\text{ }\mu\text{m} \times 20\text{ }\mu\text{m}$ ) is vertically extended in 3D to the top metal layer through stacks of vias and metal layers with  $\text{SiO}_2$  as inter-metal dielectric (IMD), as shown in the cross section in Figure 3-1a and Figure 3-2. A Reactive Ion Etching (RIE) [108], [109] post-process is utilized to open the passivation layers ( $\text{Si}_3\text{N}_4$  and  $\text{SiO}_2$ ) sitting above the top metal. The exposed top metal (Aluminum) is oxidized to form a thin  $\text{Al}_2\text{O}_3$  layer which is used as a pH sensing layer (Figure 3-1b and Figure 3-3). The sensing area of this device is the same as that of the MOSFET, i.e.  $10\text{ }\mu\text{m} \times 20\text{ }\mu\text{m}$ . These post-process steps can easily be replaced by using a passivation opening mask in the layout design phase before sending to foundry fabrication, thus making the fabrication of 3D-EMG-ISFET an unmodified commercial CMOS process. Advanced CMOS technology nodes use copper as the interconnect material, which is not bio-compatible. However, introducing one CMOS compatible fabrication step will solve this problem. That is to cover the top metal with a thin layer of oxide ( $\text{HfO}_2$ ,  $\text{Ta}_2\text{O}_5$ , or  $\text{Al}_2\text{O}_3$  which are common in biosensor applications).

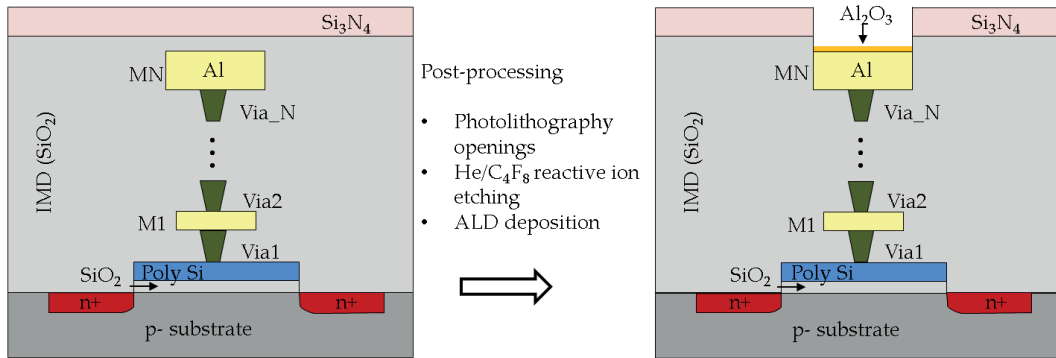


Figure 3-1 Cross-sectional view showing the fabrication of a 3D-EMG-ISFET from post-processing of a MOSFET.

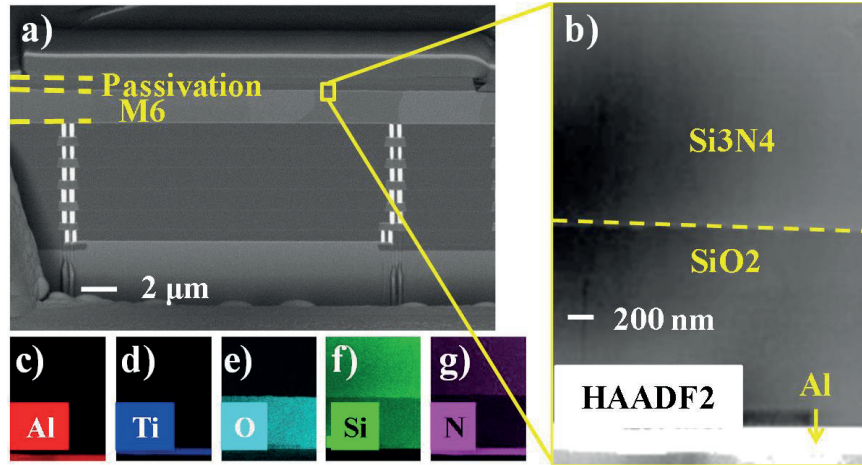


Figure 3-2 a) FIB Cross section of CMOS ISFET before RIE, b) HAADF STEM indicating passivation  $\text{Si}_3\text{N}_4/\text{SiO}_2$  layers above the top metal. c) – g) EDX analysis confirm constituent elements of Al, Ti, O, Si, N in the cross section.

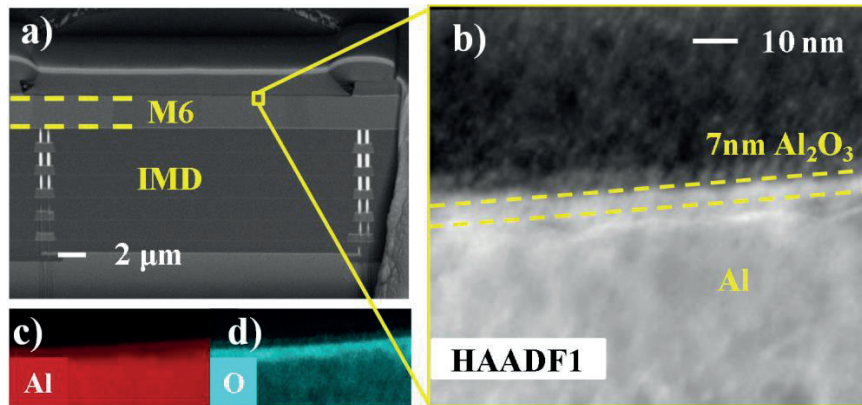
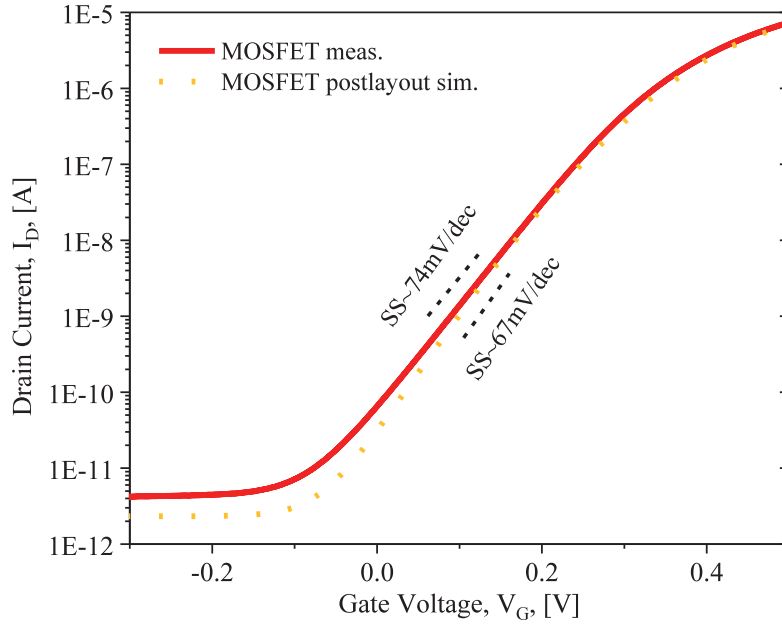
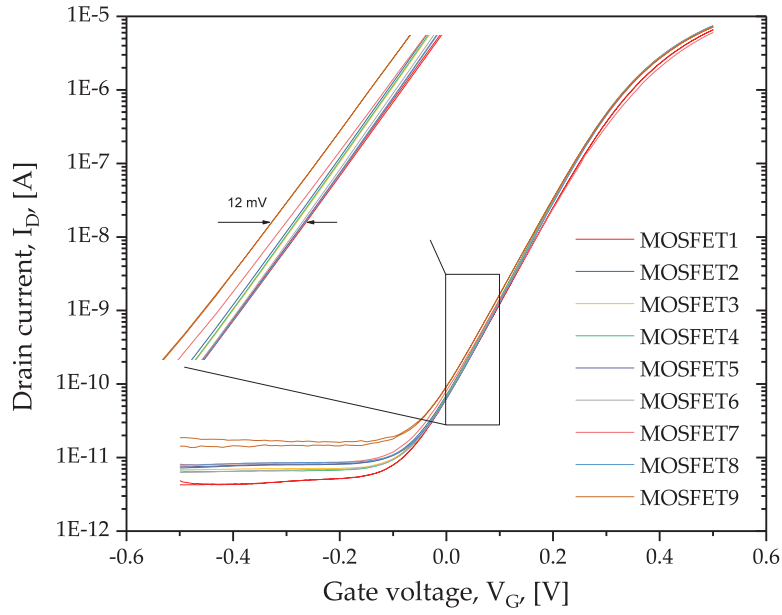


Figure 3-3 a) FIB cross section of 3D-EMG-ISFET with RIE etched openings. b) HAADF STEM image indicating 7nm native oxide on exposed top metal used for sensing. c) – d) EDX analysis confirms elemental composition of  $\text{Al}_2\text{O}_3$ .



(a)



(b)

Figure 3-4 DC characteristics of the MOSFET devices. a)  $I_D$ - $V_G$  characteristics when  $V_D = 0.1 \text{ V}$  and  $V_S = 0 \text{ V}$  for the MOSFET (measurement and post-layout simulation). b)  $I_D$ - $V_G$  characteristics of different MOSFET devices from 9 CMOS chips, showing maximum device variation  $\Delta V_{th} = 12 \text{ mV}$ .

### 3.3 pH Sensing

The 3D-EMG-ISFET is first characterized electronically as a MOSFET under dry condition. The MOSFET  $I_D$ - $V_G$  characteristics are reported in Figure 3-6a, showing a perfect fit with predicative model-based simulations. Measurements of the MOSFET have been carried out both before and after the etching steps, to validate the assumption that post processing has negligible impact on the device characteristics. The on-off current ratio is shown to be about 6 orders of magnitude. Post-layout simulated level of  $I_{off}$  is around 115 fA/ $\mu\text{m}$ , which is slightly lower than the measured 225 fA/ $\mu\text{m}$ . The subthreshold swing ( $SS$ ) is 67 mV/dec and 74 mV/dec in simulation and measurement, respectively. In the CMOS chip, MOSFETs/3D-EMG-ISFETs are connected to bias lines and readout circuits. Therefore, the post-layout simulation and measurement results in Figure 3-4a have taken into account the parasitic components due to bias and readout circuits. MOSFET simulations without these parasitic components show even lower  $I_{off}$  of around 20 fA/ $\mu\text{m}$ . In Figure 3-4b are  $I_D$ - $V_G$  characteristics of nine MOSFET devices from different CMOS chips, and they are not all the same. The device-to-device variation is caused by the charges trapped in the gate oxide and semiconductor interface. And it is characterized by the shift of the  $I_D$ - $V_G$  curve in the x-axis ( $\Delta V_{th}$ ). The MOSFET exhibits a maximum  $\Delta V_{th}$  of 12 mV.

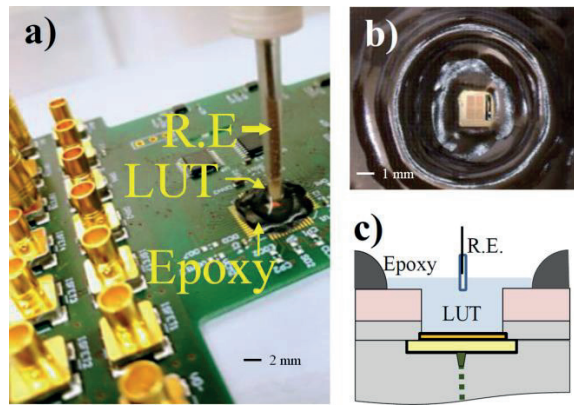
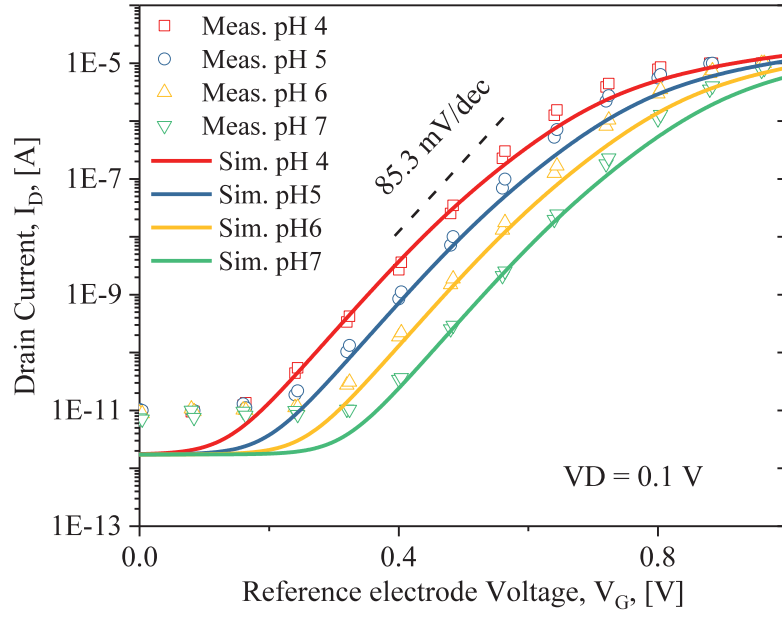
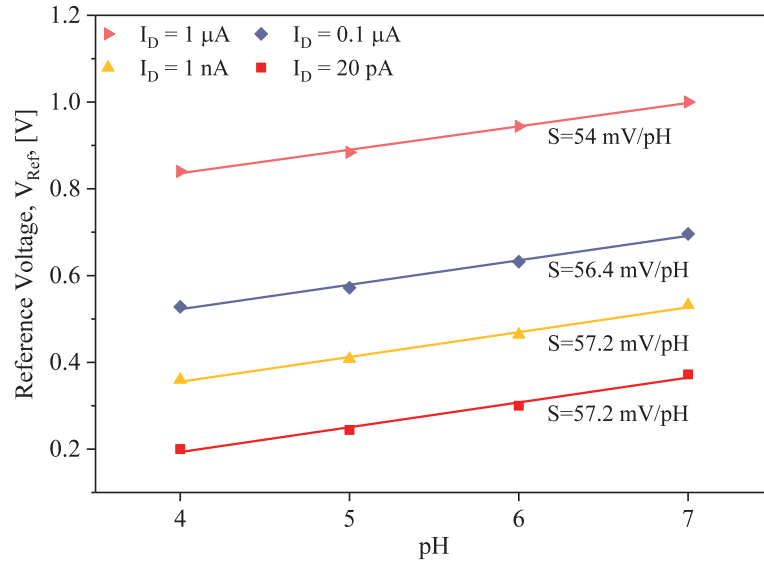


Figure 3-5 Measurement setup. a) A photo with the measurement setup, PCB with test connectors. b) Zoom in of the epoxy well created to contain a drop of  $\sim 100 \mu\text{L}$  LUT. c) Sketch of the measurement setup. R.E: Reference electrode.



(a)



(b)

Figure 3-6 DC characteristics and sensitivity for pH sensing. a)  $I_D$ - $V_G$  characteristics of the 3D-EMG-ISFET in various pH buffers, together with simulation results from a SPICE behavioral model [110]. b) pH sensitivities extracted from the shift in  $I_D$ - $V_G$  curve, at different  $I_D$  levels.



The CMOS chip is bonded to a PCB, with a specific setup for measurements of a drop of  $\sim 100\mu\text{L}$  liquid under test (LUT), as shown in Figure 3-5. We get measurement results of the 3D-EMG-ISFET's  $I_D$ - $V_G$  characteristics by applying a voltage sweep (Instrument: HP 4156, integration time: medium) on the reference electrode (RE). Compared to the  $I_D$ - $V_G$  characteristics of the MOSFET devices, the 3D-EMG-ISFET exhibits an offset in threshold voltage and degradation in  $SS$  value (85.3 mV/dec). The offset is due to the interface potential at the sensing membrane and RE, as well as to trapped charges in the sensing layer (See more details in the next section). The  $SS$  degradation is caused by the capacitance divider effect introduced by the sensing layer (Section 2.3.3.1). As expected, the resulting  $I_D$ - $V_G$  curve shifts monotonically with different pH value of the corresponding LUT (Figure 3-6a). This shift is contributed by the change of  $V_{\text{Chem}}$  defined in Figure 2-6. If we fix the drain current  $I_D$ , and extract the corresponding shift in  $V_G$ , we obtain the 3D-EMG-ISFET's sensitivity to pH (Figure 3-6b). The pH sensitivity is around 57.2 mV/pH, very close to the Nernstian limit. From Figure 3-6b, we can also see that the sensitivity doesn't degrade for  $I_D$  as low as 20 pA. This evidences that the proposed 3D-EMG-ISFET sensor can be operated with the lowest power consumption among all reported ISFETs to date.

### 3.4 Trapped charge elimination

In the previous section we have demonstrated a CMOS foundry fabricated ISFET that exhibits excellent performance in pH sensing. In modern foundry processes, the behavior of integrated circuits can be accurately simulated with a SPICE model. By incorporating effect of the proton buffer capacity of the sensing layer and the capacitance divider introduced from the sensing layer, S. Martinoia et al. developed a SPICE behavioral model [110] for simulating ISFETs. We used this model to simulate the equivalent circuit shown in Figure 2-6, and obtained the simulation results shown in Figure 3-6a. The simulation results agree well with the measurement results, in terms of  $SS$  value and pH sensitivity.

Given an ISFET with fixed dimensions, the absolute position of the  $I_D$ - $V_G$  curve on the  $x$ -axis is determined by the liquid-sensor interface, the amount of trapped charge in the gate oxide, the oxide/semiconductor interface, and the sensing layer. The effects of the first two kinds of trapped charges have been experimentally shown as MOSFET device variation ( $\Delta V_{\text{th}}$ ) in Figure 3-4. And they are already optimized by the foundry process. Therefore, in

order to improve the predictability of the CMOS ISFETs, we introduce a way to eliminate the trapped charges in the sensing layer.

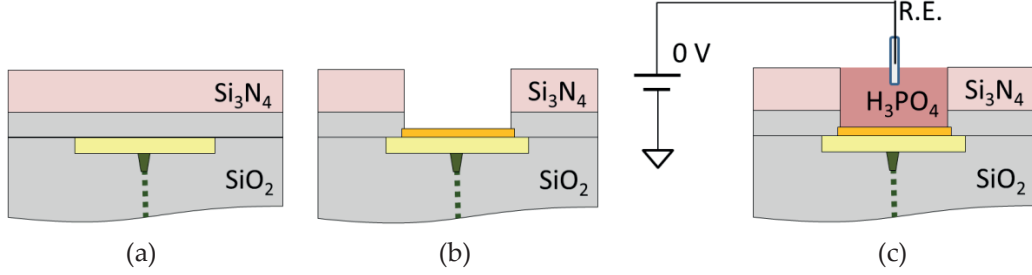


Figure 3-7 Process steps for removing trapped charge. a) Before RIE: the Si<sub>3</sub>N<sub>4</sub> passivation layer is used as sensing dielectric. b) After RIE: the Al<sub>2</sub>O<sub>3</sub> layer is used for sensing. c) Wet etching.

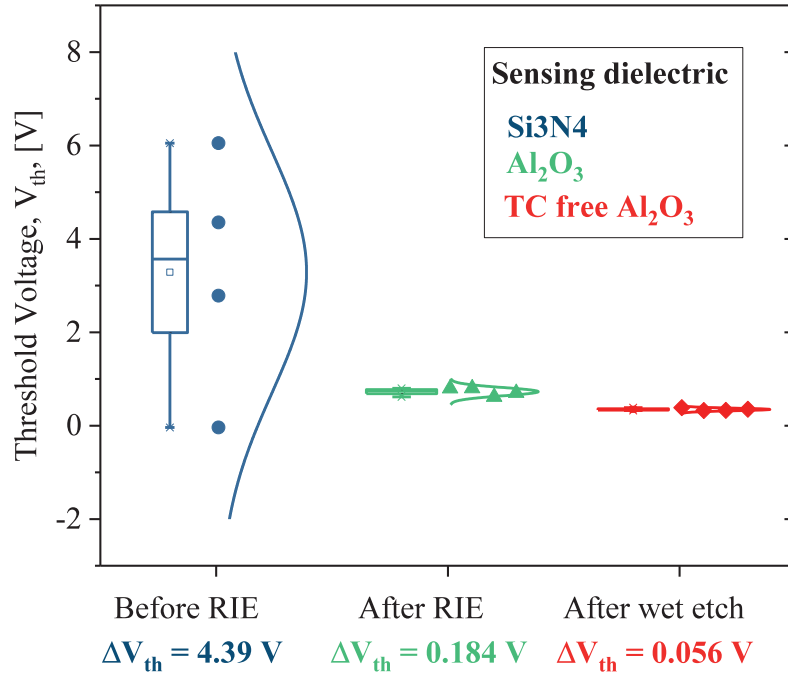
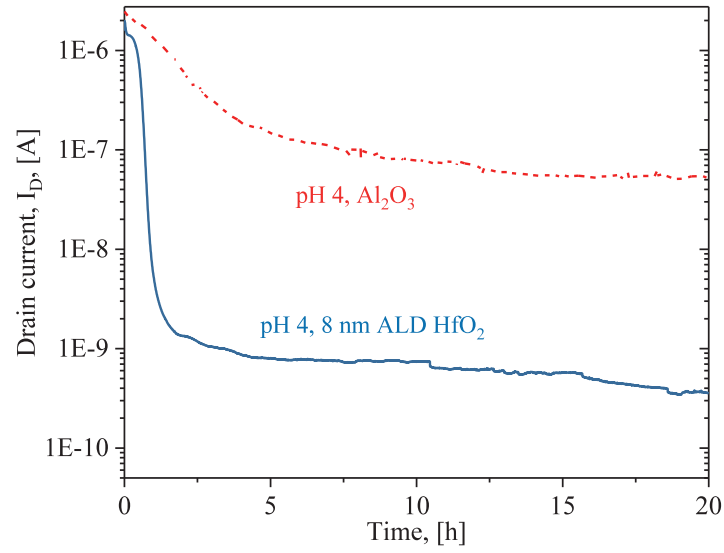


Figure 3-8 Threshold variation results after removing the trapped charges.  $\Delta V_{th}$  of the ISFETs measured in pH 7 buffer solution.

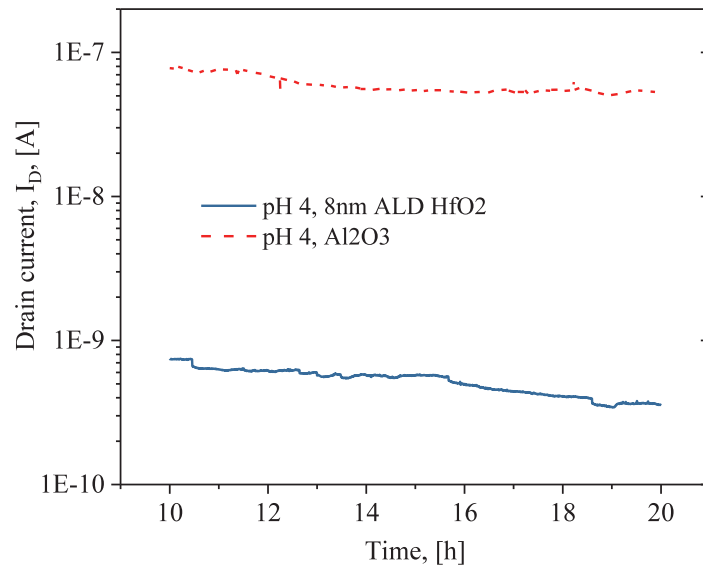
As introduced before, conventional CMOS ISFETs utilize the  $\text{Si}_3\text{N}_4$  passivation layer for pH sensing. Therefore, they inevitably introduce a large amount of trapped charges in the  $\text{Si}_3\text{N}_4$  and  $\text{SiO}_2$  passivation layers [109], [111], resulting in large  $\Delta V_{\text{th}}$  when they are directly used for pH sensing. Our 3D-EMG-ISFETs, before being processed through the RIE step, belong to the category of conventional CMOS ISFETs. Therefore, we characterized their  $\Delta V_{\text{th}}$  in pH 7 buffer solution. Among four CMOS ISFET devices before RIE (Figure 3-7a), the resulted  $\Delta V_{\text{th}}$  is 4.39 V, as shown in Figure 3-8 in blue. This variation is seen to be greatly reduced just after the RIE step (Figure 3-7b), due to removal of the trapped charges in the passivation layers,  $\Delta V_{\text{th}}$  decreased to 184 mV (Figure 3-8 in green). Finally, we introduced a wet etching step (Figure 3-7c): phosphoric acid (85% wt. in  $\text{H}_2\text{O}$ ) diluted in de-ionized (DI) water with a ratio 1:1 is deposited onto the chip surface at room temperature, while it is biased at 0 V with a commercial Ag/AgCl reference electrode (16-702, Microelectrodes Inc.) for 2 minutes. A trapped-charge free (TC-free)  $\text{Al}_2\text{O}_3$  is grown afterwards. The wet etching step affirms our hypothesis that the RIE step has introduced new trapped charges in the  $\text{Al}_2\text{O}_3$  layer, and that we succeeded in removing them. The final device-to-device variation is  $\Delta V_{\text{th}} = 56$  mV (Figure 3-8 in red), which is two orders of magnitude improvement from the conventional ISFET, and comparable to that of the MOSFET devices in Figure 3-4b. State of the art attempts to remove the trapped charge using UV radiation also have given satisfactory results [112], however, by a device to device calibration process (17 hours of UV radiation for each device). In contrast, the experimental achievements reported in our work can be a batch process and require only a few minutes.

There also have been other reported attempts to reduce the threshold voltage variation by RIE [101], [109], however, they didn't etch through the  $\text{SiO}_2$  layer. They finally utilized the  $\text{SiO}_2$  as sensing layer for pH, although it is well known that  $\text{SiO}_2$  is characterized by a large drift [113].

Therefore, the trapped charge elimination method introduced in this section, supported by SPICE calibrated behavioral model simulations results, are expected to greatly enhance the predictability of high performance ISFETs, which is a big step towards ISFET sensor system mass production.



(a)



(b)

Figure 3-9 Stability study of the ISFET, comparison between native  $\text{Al}_2\text{O}_3$  and 8 nm  $\text{HfO}_2$  deposited with ALD as sensing layer. a) Long term  $I_D$  drift of the 3D-EMG-ISFET in a period of 20 hours. b) Zoom in of the drift characteristics from 10<sup>th</sup> hour to 20<sup>th</sup> hour.

### 3.5 Drift

Long term stability is a key figure of merit for sensors. ISFET sensors' threshold voltage undergoes drift due to surface potential changes caused by interactions between the liquid and sensing dielectric. And the stability of an ISFET sensor is characterized by the drift rate of its threshold voltage (unit: mV/h).

It can only be measured indirectly [114]: one of the ways is to bias the ISFET's terminals at constant voltages, and record the time dependent behavior of  $I_D$ . The  $V_{th}$  drift rate can be converted from  $I_D$  drift by using the  $I_D$ - $V_G$  characteristic curve.

Two kinds of 3D-EMG-ISFET sensors are compared in terms of long term stability. They are different only in the sensing dielectric: 1. native oxide (7 nm  $Al_2O_3$ ), 2. controlled oxide (7 nm native  $Al_2O_3$  + 8 nm Atomic Layer Deposited  $HfO_2$ ). The 3D-EMG-ISFETs are immersed in pH 4 buffer solution with constant bias voltages, while  $I_D$  is monitored from the first minute that the sensing area gets in contact with the liquid. Shown in Figure 3-9a is the  $I_D$  drift of the 3D-EMG-ISFET in a 20 hours long term measurement. As have been exhaustively reported by other researchers [113], [115], the rapid decreasing of  $I_D$  in the first hours, is due to the hydroxyl group diffusion in the oxide. After the 14th hour, a drift rate of 0.67 mV/h is calculated for the ISFET with native oxide, whereas 2 mV/h is extracted for the ISFET with controlled sensing surface (ALD  $HfO_2$ ) for the same period of time (Figure 3-9b). This comparison shows that the native oxide layer manifests itself as a qualified sensing layer.

### 3.6 Multiple Cation Sensing

#### 3.6.1 Functionalization

As mentioned earlier, the 3D-EMG-ISFETs use the  $Al_2O_3$  dielectric layer for pH sensing, as shown in Figure 3-10a. In order to make it selectively sensitive to different ions, the 3D-EMG-ISFET is smartly functionalized with an Ion Selective Membrane (ISM) for each ion species. The ISM is an effective functionalization method for chemical sensing, made through the embedding of a specific ion receptor (called ionophore) in a polyvinyl chloride (PVC) based membrane. It is drop-casted on top of the 3D-EMG-ISFET's sensing

dielectric. The ionophore from the membrane selectively interacts with its target ion while weakly interacting with interfering ions. The interactions result in development of a junction potential (affects the ISFETs' gate bias) that is proportional to the ion activity at the liquid-to-ISM interface. In this work, there are three types of membranes deposited for  $\text{Na}^+$ ,  $\text{K}^+$  and  $\text{Ca}^{2+}$  sensing, resulting in 3D-EMG-( $\text{Na}^+$ ,  $\text{K}^+$ ,  $\text{Ca}^{2+}$ ) sensitive FET, respectively (Figure 3-10b-d).

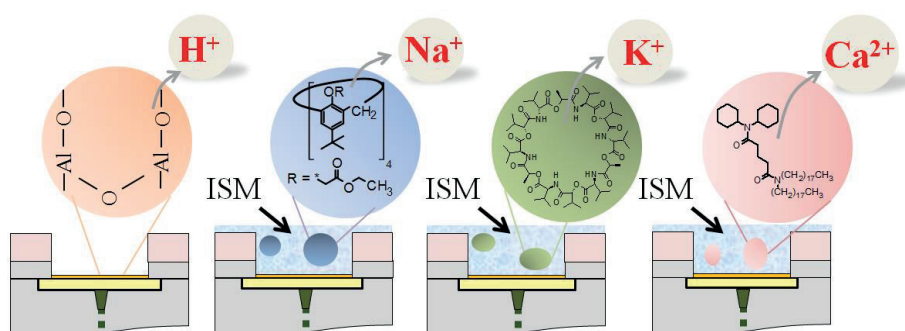


Figure 3-10 3D-EMG-ISFET with different functionalization for sensing different ions. a) 3D-EMG-ISFET with  $\text{Al}_2\text{O}_3$  as the sensing layer. b) 3D-EMG- $\text{Na}^+$  sensitive FET. c) 3D-EMG- $\text{K}^+$  sensitive FET. d) 3D-EMG- $\text{Ca}^{2+}$  sensitive FET. All ion sensitive FETs use a specific ISM.

The Sodium-selective membrane was prepared by mixing Na ionophore X (1% w/w), Sodium tetrakis[3,5-bis(trifluoromethyl)phenyl] borate (Na-TPPB) (0.55% w/w), polyvinyl chloride (PVC) (33% w/w), and bis(2-ethylhexyl) sebacate (DOS) (65.45% w/w). 100 mg of the membrane cocktail was dissolved in 660  $\mu\text{l}$  of tetrahydrofuran (THF). The Potassium-selective membrane cocktail was composed of valinomycin (2% w/w), Sodium tetraphenylborate (NaTPB) (0.5% w/w), PVC (32.7% w/w), and DOS (64.7% w/w). 100 mg of the membrane cocktail was dissolved in 350  $\mu\text{l}$  of cyclohexanone. The Calcium-selective membrane was composed of calcium ionophore IV (1.2% w/w), 2-nitrophenyl octyl ether (66% w/w) and PVC (32.5% w/w), Na-TPPB (0.3% w/w). 100 mg of the membrane cocktail was dissolved in 660  $\mu\text{l}$  of THF. Ion-selective membranes were then prepared by drop-casting 10  $\mu\text{l}$  of the membrane cocktails onto the respective groups of ISFETs. The author acknowledges Dr. Johan Longo for making the ISM cocktails.

Sodium ionophore X is chosen due to the reason that the best  $\text{Na}^+$  selectivities have been achieved with calix[4]arene derivatives. The success of these calix[4]arenes can be ascribed to the phenolic oxygens, which provide for a scaffold on which various functional groups can be attached, giving an optimum cavity for the complexation of  $\text{Na}^+$  [116]. Valinomycin, an antibiotic from cultures of *Streptomyces fulvissimus*, was reported to form crystalline complexes with  $\text{K}^+$  [117]. Valinomycin based  $\text{K}^+$  ionophore is selected because it has been applied to ISEs to show a quick response time and a very good selectivity [118]. A  $\text{Ca}^{2+}$  ionophore (ETH 5234) based on diamides is adopted due to its high selectivity and long lifetime [54]. The preference for  $\text{Ca}^{2+}$  over monovalent cations and larger cations is enhanced by a large dipole moment of the substituents; very bulky substituents shift the selectivity toward monovalent ions [116].

### 3.6.2 Sensitivity and Selectivity

The DC characteristics of 3D-EMG-( $\text{Na}^+$  /  $\text{K}^+$  /  $\text{Ca}^{2+}$ ) sensitive FETs are measured by immersing them in various salt solutions<sup>1</sup> of different concentrations, and measuring the corresponding  $I_D$ - $V_G$  characteristics curve. The curves are shown in Figure 3-11a, Figure 3-12a, Figure 3-13a, respectively. Sensitivities of each sensor to the corresponding ion species (main ion) are extracted at  $I_D = 10$  nA, and shown in Figure 3-11b, Figure 3-12b, Figure 3-13b, respectively. Three  $I_D$ - $V_G$  measurements are taken to extract the sensitivities, and their mean values as well as standard deviations are shown in the same figures with error bars. Excellent sensitivities (-56.9 mV/dec[X] for  $\text{Na}^+$ , -48.1 mV/dec[X] for  $\text{K}^+$ , -25.7 mV/dec[X] for  $\text{Ca}^{2+}$ ) are achieved with the 3D-EMG-( $\text{Na}^+$  /  $\text{K}^+$  /  $\text{Ca}^{2+}$ ) sensitive FETs, respectively. The “low” sensitivity of the  $\text{Ca}^{2+}$  sensitive FET is due to its divalent nature, resulting in a Nernstian limit of 29.6 mV/dec[X] (Equation 2.12), instead of 59.2 mV/dec[X] for monovalent ions ( $\text{H}^+$ ,  $\text{Na}^+$ ,  $\text{K}^+$ , etc).

Since there are many different ions in sweat, such as  $\text{H}^+$ ,  $\text{Na}^+$ ,  $\text{K}^+$ ,  $\text{NH}_4^+$ ,  $\text{Ca}^{2+}$ , and so on, the ideal sensor for sensing one ion (main ion) in sweat should at the same time be insensitive to the others (interfering ions). Therefore we designed a series of experiments in order to quantify the selectivity/cross sensitivity of our sensors. First,  $I_D$ - $V_G$  characteristics of the sensor are measured when the sensor is immersed in different drops of salt solution with

---

<sup>1</sup> Salt solutions used in this chapter are prepared with the corresponding ion's chloride salt dissolved in deionized (DI) water.

various concentrations of the interfering ions. Second, sensitivity of this ISFET to the interfering ions is extracted by setting  $I_D = 10$  nA, this is called the selectivity or cross sensitivity. Finally, plot them in the right-Y axis of Figure 3-11b, Figure 3-12b and Figure 3-13b.

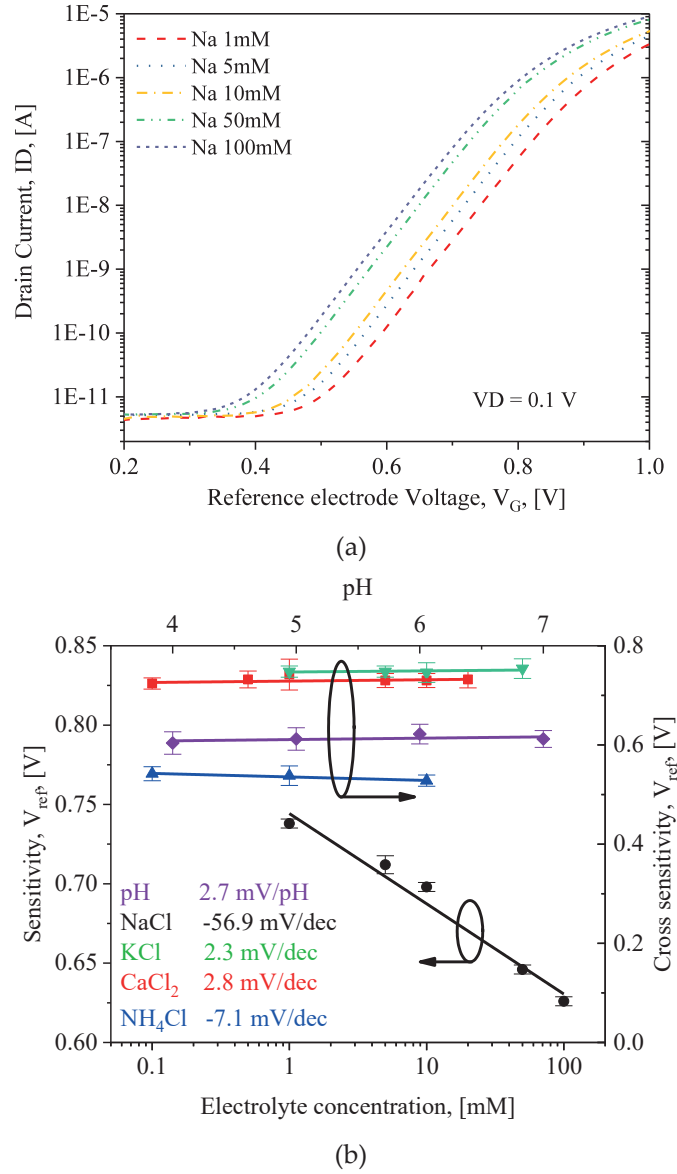


Figure 3-11 DC characteristics and sensitivity for  $\text{Na}^+$  sensing. a)  $I_D$ - $V_G$  characteristics of the 3D-EMG- $\text{Na}^+$  sensitive FET, in NaCl solutions of various concentrations. b) Sensitivity and Cross sensitivity plot for the  $\text{Na}^+$  sensitive FET.



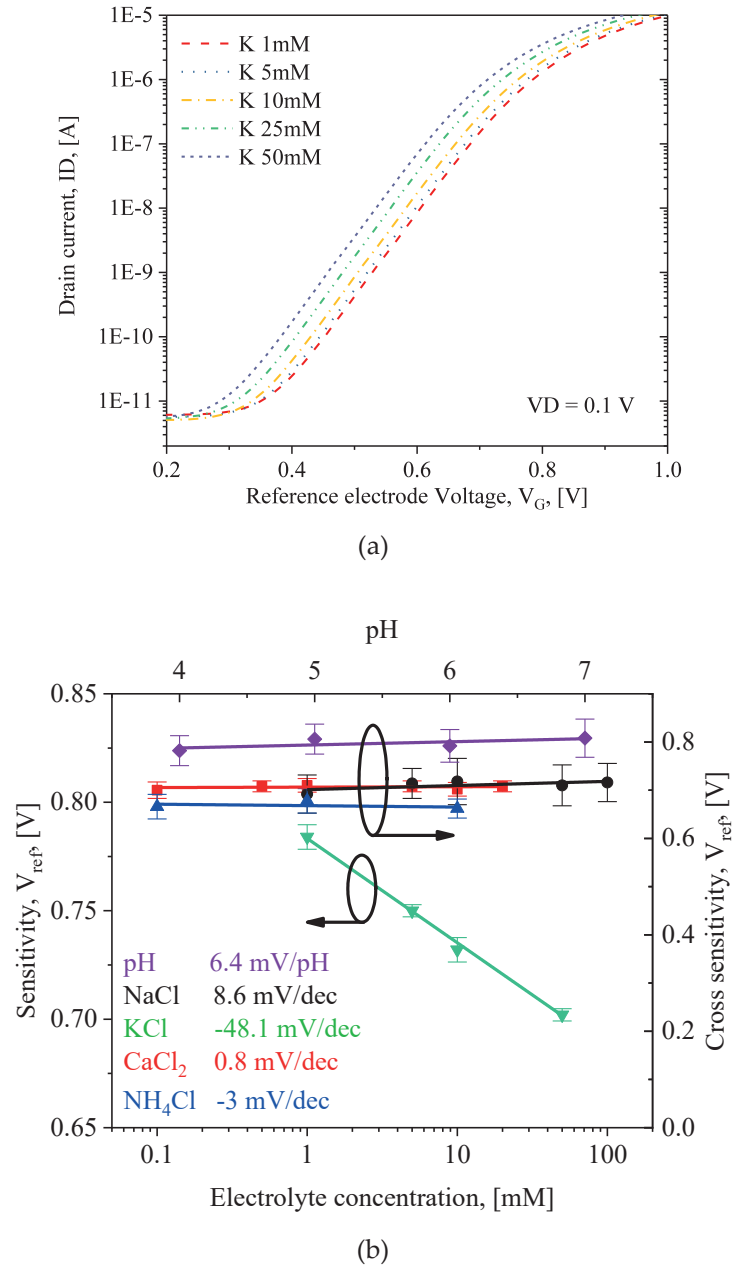


Figure 3-12 DC characteristics and sensitivity for K<sup>+</sup> sensing. a)  $I_D$ - $V_G$  characteristics of the 3D-EMG-K<sup>+</sup> sensitive FET, in KCl solutions of various concentrations. b) Sensitivity and Cross sensitivity plot for the K<sup>+</sup> sensitive FET.

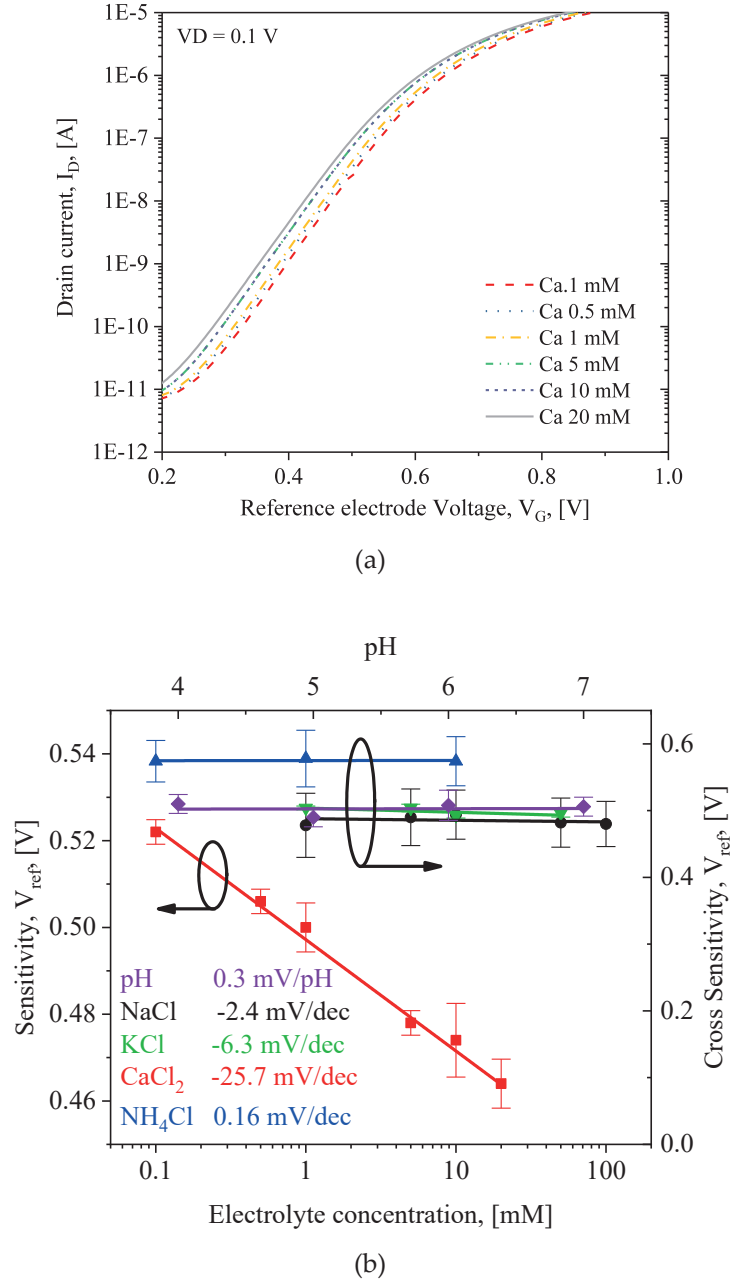


Figure 3-13 DC characteristics and sensitivity for  $\text{Ca}^{2+}$  sensing. a)  $I_D$ - $V_G$  characteristics of the 3D-EMG- $\text{Ca}^{2+}$  sensitive FET, in  $\text{CaCl}_2$  solutions of various concentrations. b) Sensitivity and Cross sensitivity plot for the  $\text{Ca}^{2+}$  sensitive FET.

It is worth to note that different research groups have achieved ISFETs with comparable or even lower cross sensitivity [98], [119], at the cost of more area (for a control electrode)

and extra computation, e.g. differential measurement. The requirement for the control electrode to behave exactly the same as the sensing electrode makes the differential measurement difficult (if not impossible) to implement.

### 3.7 Dynamic Response

The 3D-EMG-ISFET's dynamic response in pH sensing is studied by measuring time dependent  $I_D$  response of the sensor, at constant bias voltages:  $V_{SB} = 0$  mV,  $V_{DS} = 100$  mV and  $V_{GS} = 500$  mV. As shown in Figure 3-14, the pH sensing exhibits excellent repeatability and rapid response ( $< 5$  s). Similar dynamic measurements for the 3D-EMG-( $Na^+ / K^+ / Ca^{2+}$ ) sensitive FETs are shown in Figure 3-15, Figure 3-16 and Figure 3-17, respectively. From these dynamic response plots, we further confirm that the 3D-EMG-ISFET sensors are capable of operating down to pico-Amperes range without degrading sensitivity. Especially from Figure 3-16, we observe that the 3D-EMG- $K^+$  sensing FET shows a drain current that is responding negatively to the  $Na^+$  concentration, which is a collateral evidence of the cross sensitivity characterized in Figure 3-12b. Current sensitivity  $S_I$  of the 3D-EMG- sensors to  $H^+$ ,  $Na^+$ ,  $K^+$ ,  $Ca^{2+}$  ions, are extracted from each dynamic response plot, respectively:  $S_{I_{H^+}} = 0.59$  ,  $S_{I_{Na^+}} = 0.78$  ,  $S_{I_{K^+}} = 0.7$  ,  $S_{I_{Ca^{2+}}} = 0.5$  . The achieved sensitivities are excellent compared to state of the art current sensitivities and shown in Table 2.

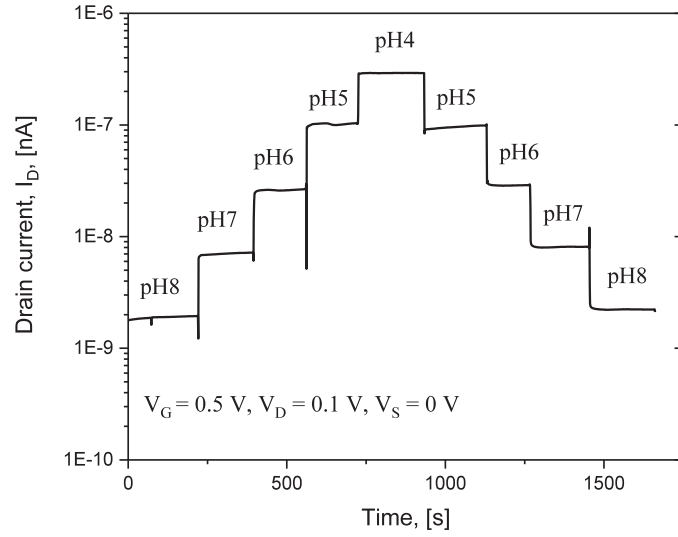
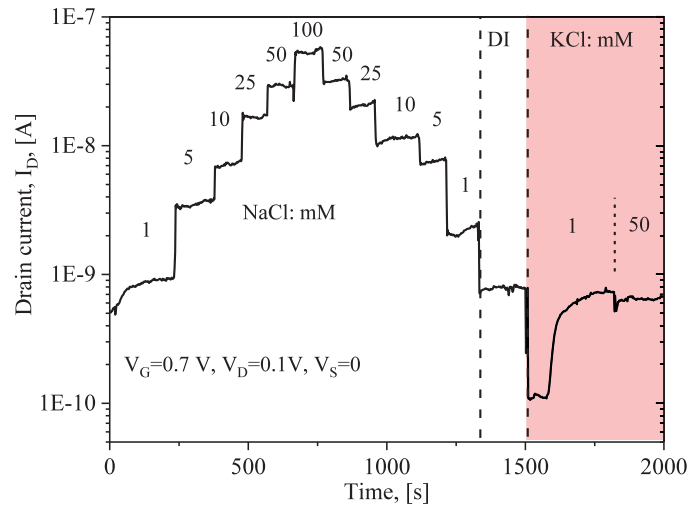


Figure 3-14 Dynamic response of the 3D-EMG-ISFET pH sensor.

Figure 3-15 Dynamic response of the 3D-EMG-ISFET  $\text{Na}^+$  sensor.

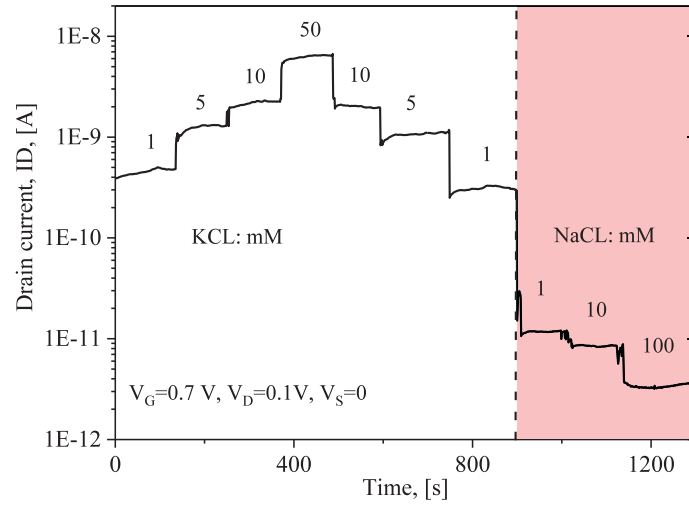


Figure 3-16 Dynamic response of the 3D-EMG-ISFET  $K^+$  sensor.

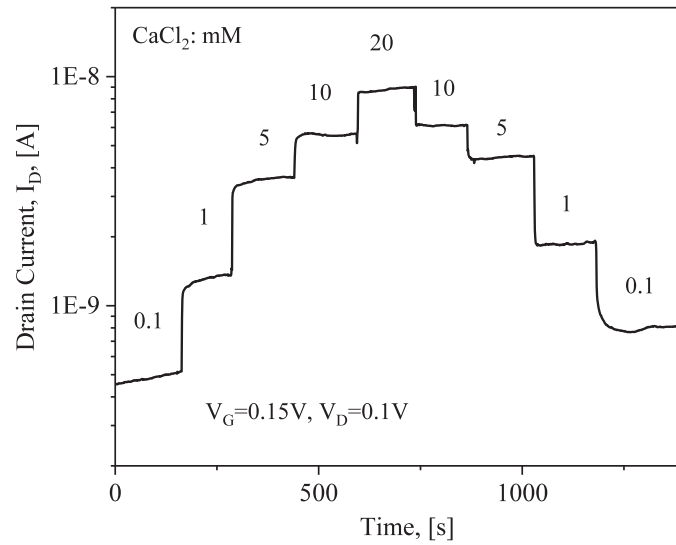


Figure 3-17 Dynamic response of the 3D-EMG-ISFET  $Ca^{2+}$  sensor.

We have quantitatively examined the selectivity of each 3D-EMG-ISFET's selectivity against interfering ions in Figure 3-11, Figure 3-12 and Figure 3-13. It is still of interest to

know how they perform when simultaneously working in a solution that contains multiple ions, in terms of tracking their corresponding ions as well as rejecting the interferences from other ions. Therefore, we designed another experiment to examine this, with the measurement setup shown in Figure 3-18 and Figure 3-19. As shown in Figure 3-18a, the sensing system is a  $0.18\ \mu\text{m}$  foundry fabricated CMOS sensor chip containing five groups of 3D-EMG-ISFET sensors, each group contains nine ISFETs, dedicated to sense one type of ion. Only one sensor in each group is needed to complete the sensing. This redundancy is made for the convenience of checking reproducibility. The large distance between different ion sensors is due to the fact that there is a minimum size limit of membrane made by drop-casting. The drain, source, and gate terminals of all the ISFETs are connected through metallic wires and metalized inter-metal vias to pads in the peripherals of the chip. The bulk terminals are all connected to the p-doped substrate and biased through the aluminum base shown in the inset of Figure 3-19. Figure 3-18b shows two groups of ISFETs covered by  $\text{K}^+$  and  $\text{Na}^+$  ISMs, respectively. The ISMs are casted on top of the sensing area, but we are also working on inkjet printing of ISMs, in order to make the fabrication of ion sensors more controllable and occupy less area.

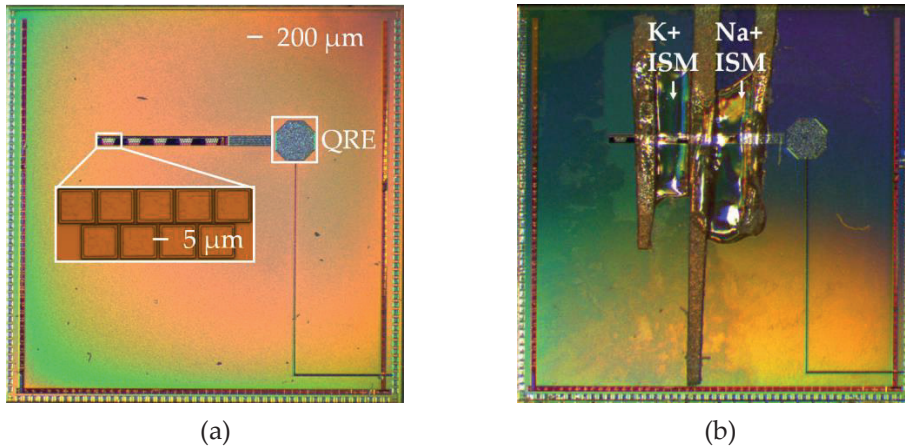


Figure 3-18 CMOS sensor chip functionalized to simultaneously monitor  $\text{K}^+$  and  $\text{Na}^+$ . a) CMOS sensor chip containing five groups of 3D-EMG-ISFET sensors. QRE (quasi reference electrode): will be introduced later. b) A drop of  $\text{K}^+$  and  $\text{Na}^+$  ISM is casted on top of two groups of ISFET, respectively.

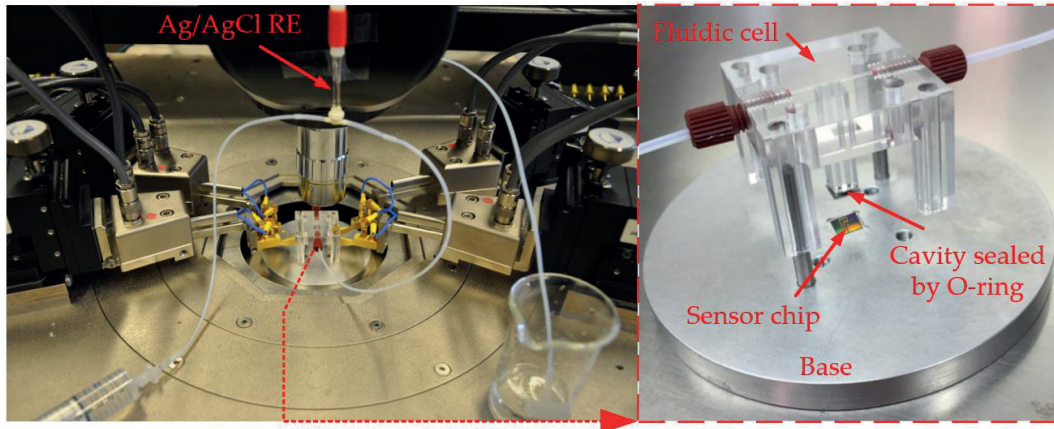


Figure 3-19 Measurement setup for simultaneously measuring the two different ion sensors in the CMOS sensor chip shown in Figure 3-18. Inset: Exploded view of the fluidic cell configuration.

The measurement setup is shown in Figure 3-19. The LUT is biased with a commercial Ag/AgCl RE (16-702, Microelectrodes Inc.) through plastic tubes. A fluidic cell (Figure 3-19 inset) is used to deliver the LUT to the surface of the sensors. The fluidic cell is constructed with PMMA by laser cut fabrication. There is a cavity at the end of the fluidic cell allowing the LUT to cover the area of the sensors. The cavity is filled with 6  $\mu\text{L}$  of LUT when a measurement is undergoing. We randomly chose one of the 3D-EMG-ISFET sensors in each group covered by the ISMs, and measured their dynamic response by probing the corresponding drain and source terminals. Setting  $V_s = V_B = 0$  mV,  $V_D = 100$  mV and  $V_{RE} = 500$  mV, the dynamic drain currents of both sensors ( $I_{D,Na^+}$  and  $I_{D,K^+}$ ) are recorded simultaneously, and shown in Figure 3-20. The LUTs are prepared by dissolving various concentrations of two salts (NaCl and KCl) in DI water. From this plot, the sensors show rapid and repeatable response to the concentration changes in the main ions, and at the same time exhibit negligible response to the interfering ions.

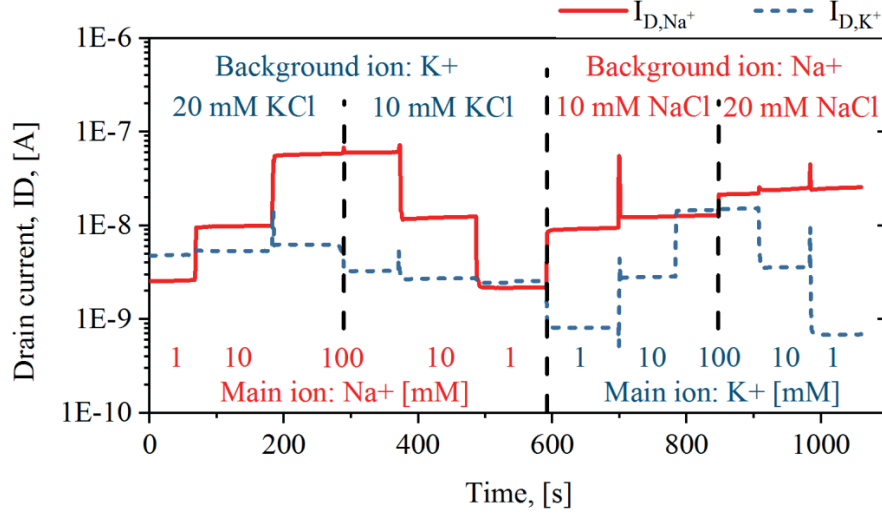


Figure 3-20 Simultaneous dynamic response of the 3D-EMG-Na<sup>+</sup> and 3D-EMG-K<sup>+</sup> sensitive FETs, in solutions with varying concentrations of both Na<sup>+</sup> and K<sup>+</sup>.

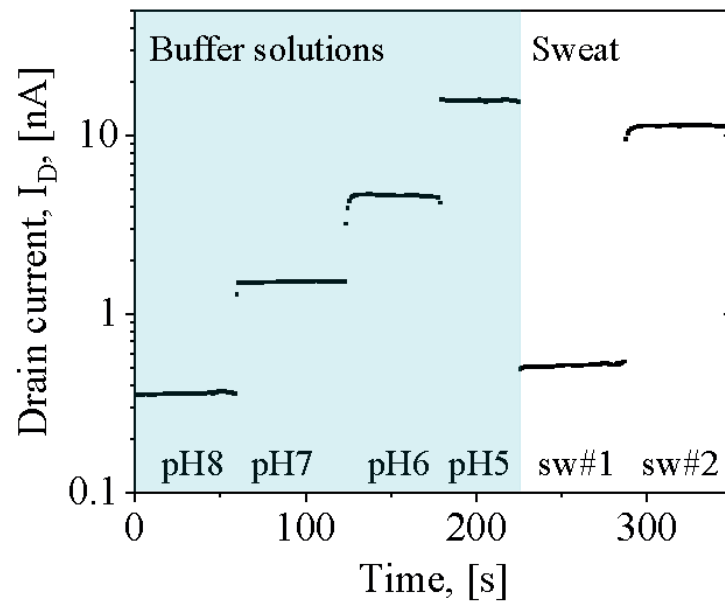
### 3.8 In-vitro Sweat Tests

We have designed an in-vitro sweat test experiment to prove the validity of our sensors in sweat sensing application, using the same setup as described in Figure 3-19 to measure samples of unspiked human sweat. The results are introduced in section 3.8.1, and the detailed experiment steps and calibration methods are described section 3.8.2.

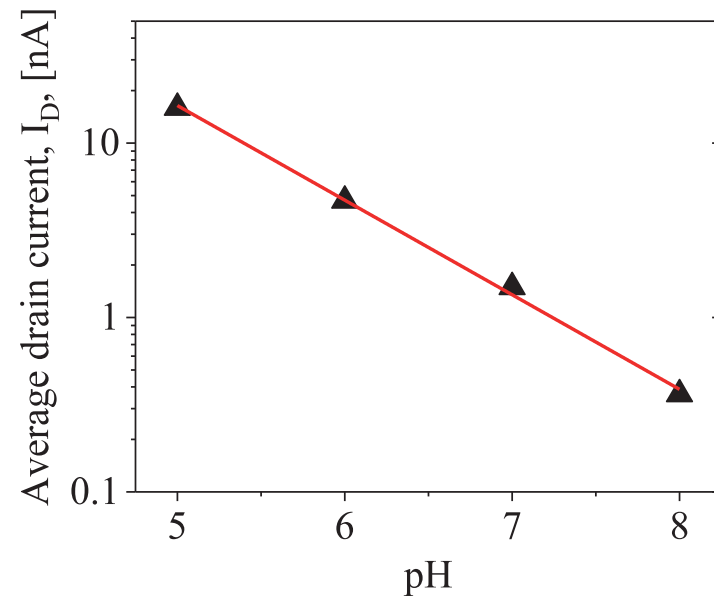
#### 3.8.1 Results and Discussions

The dynamic measurements of artificial sweat buffers and unspiked sweat samples are shown in Figure 3-21a and Figure 3-21c. The calibration curves are extracted and shown in Figure 3-21b and Figure 3-21d. We can see that the drain current of our 3D-EMG-ISFET sensors are, as expected from Equation 2.13, exponentially related to pH or, in general, to the logarithm of ion concentrations. Na<sup>+</sup> concentrations and pH values of the sweat samples are calculated with the aid of the calibration curve.





(a)



(b)

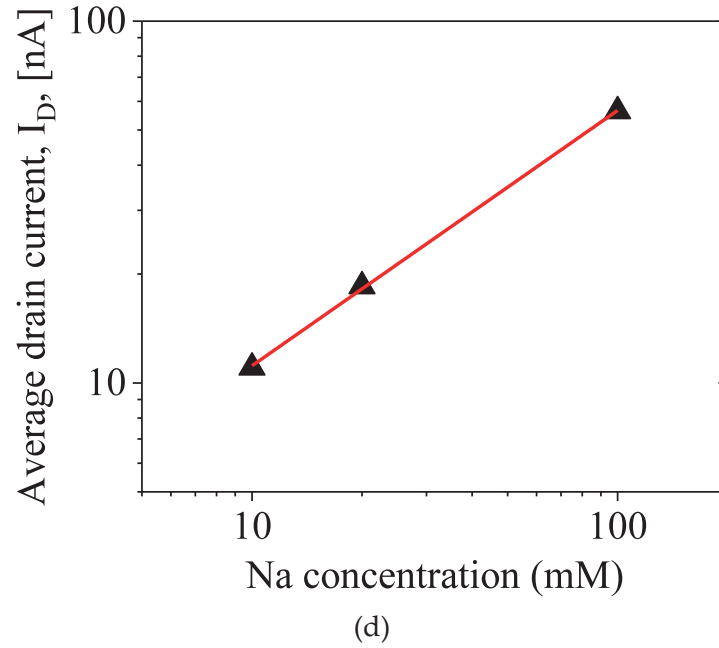
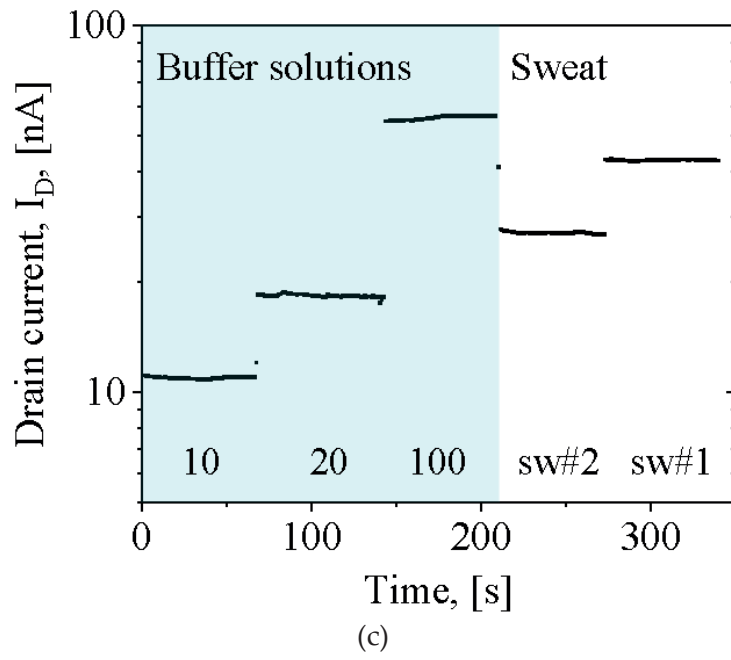


Figure 3-21 a) Dynamic measurements with sweat samples and various pH buffers to extract b) calibration curve for 3D-EMG-pH sensors, and calculate sweat pH values. c) Dynamic measurements with sweat samples and various NaCl solutions to extract d) calibration curve for 3D-EMG-Na<sup>+</sup> sensors, and calculate sweat Na<sup>+</sup> concentrations.

The dynamic measurement results for extracting calibration curve and calculating sweat electrolyte concentration show a maximum time-dependent standard deviation of 1.95% in 3D-EMG-Na<sup>+</sup> sensor, and 1.36% in the 3D-EMG-pH sensor, with respect to their average value. We measured the same sweat samples with three 3D-EMG-Na<sup>+</sup> sensors and three 3D-EMG-pH sensors. The standard-deviation-to-average-value-ratios of the measurement results from sensor to sensor are characterized to be 9.3% for our Na<sup>+</sup> sensors, and 2.3% for our pH sensors. Compared to the results from the commercial Na<sup>+</sup> meter and pH meter, our sensors' measurement results deviate from them by maximum 12% and 2.8%, respectively. These standard deviations and variations from commercial sensors are small enough to be neglected compared to the large range of Na<sup>+</sup> concentration and pH in sweat during daily activities.

### 3.8.2 Experimental Methods

Sweat samples were induced and collected from two healthy volunteers, when sitting in a sauna, for off-body evaluation. Sweat samples were initially tested with a commercial ISE (HORIBA LAQUAtwin-Na-11) to measure Na<sup>+</sup> concentration, and a commercial pH meter (HORIBA LAQUAtwin-pH-22) to measure pH, and the results were compared with the 3D-EMG-ISFET sensor readings for the same sweat samples. Results measured by the 3D-EMG-ISFET sensors were computed using three point calibrations for [Na<sup>+</sup>] and four point calibrations for pH.

The calibration curve for pH was obtained from Phosphate buffers of pH value varying from 5 to 8. The terminals of the 3D-EMG-ISFET sensor were biased at constant voltages, while the dynamic current response is recorded for different pH buffers as well as the sweat samples (Figure 3-21a). The dynamic response current values were extracted, and averaged, to achieve the calibration curve shown in Figure 3-21b. pH values of the sweat samples were calculated from the average dynamic current values, with the calibration curve and listed in Table 2.

Similar method was applied to the 3D-EMG-Na<sup>+</sup> sensor to extract calibration curve (Figure 3-21c and Figure 3-21d). The calibration curve for [Na<sup>+</sup>] was obtained from measuring artificial sweat containing 10 mM KCl with 10 mM, 20 mM and 100 mM NaCl concentrations in DI water.

Table 3-2. Na<sup>+</sup> concentrations in two sweat samples measured by three 3D-EMG-Na<sup>+</sup> sensors and a commercial Na<sup>+</sup> Meter; pH values of the same samples measured by three 3D-EMG-pH sensors and a commercial pH Meter. Na<sup>+</sup> Meter results were converted from open-circuit-potential readings.

[Na <sup>+</sup> ] (mM)				
	3D-EMG-Na <sup>+</sup> sensor 1	3D-EMG-Na <sup>+</sup> sensor 2	3D-EMG-Na <sup>+</sup> sensor 3	HORIBA Na <sup>+</sup> Meter
sweat #1	74.7	69.2	68.2	77.5
sweat #2	33.9	29.7	35.7	33.2
pH				
	3D-EMG-pH sensor 1	3D-EMG-pH sensor 2	3D-EMG-pH sensor 3	HORIBA pH Meter
sweat #1	7.76	7.69	7.43	7.65
sweat #2	5.28	5.24	5.16	5.16

### 3.9 Conclusions

In this work, Ion Sensitive Field Effect Transistor (ISFET) arrays are realized with 3-dimensional extended gate in a CMOS technology, and enable multiple biomarker detection on a single die. The sensor introduced here has the following breakthrough novelties and improvements compared to state of the art ISFETs (summarized in Table 3-1 and Table 3-3):

- Nowadays, advanced ISFETs using 1D or 2D semiconducting materials, may require non-trivial processing steps, resulting in low yield, low robustness devices. The proposed 3D-Extended-Metal-Gate ISFETs (3D-EMG-ISFETs) are fabricated in a foundry process. Different from other ISFETs fabricated in foundry process (CMOS ISFET), our sensors have extraordinary high performance, which we summarized and compared with state of the art in Table 1 of the main text. At the same time, the 3D-EMG-ISFETs maintain the virtues of standard foundry-made ISFETs, which include high yield, high robustness, low cost and up-scalability.
- The sensors' power consumption is a record low. Down to picoWatt per sensor (3 orders of magnitude lower than state of the art), without degradation of the sensitivity.

- Significantly reduced threshold voltage variation, from sensor to sensor. Threshold voltage of an ISFET is keen to vary from device to device, mostly due to immaturely controlled fabrication steps and trapped charge in the passivation layers. A CMOS ISFET often exhibit threshold variation on the order of volts, while we achieved a variation of  $\pm 28$  mV.

Table 3-3. State-of-the-Art (SoA) in electrochemical ion sensors

	Ion	$S_V$	Cross sensitivity: $CS_V$				$S_I$	min. Power <sup>1</sup>	RT <sup>2</sup>	DR <sup>3</sup>	CMOS Int <sup>4</sup>
			H	Na	K	Ca					
This work	H	-57		NG	NG	NG	0.59	2 pW	<5	0.7	Yes
	Na	-57	2.7		2.3	2.8	0.78				
	K	-48	6.4	8.6		0.8	0.7				
	Ca	-26	0.3	-2.4	-6.3		0.5				
[91]	H	-57		NG	NG	NG	0.4	8 nW	<5	0.1	No
[98]	Na	-38	-46 **		NG	NG	0.01	1 nW *	<5	NG	No
[120]	K	-64	NG	-8 *		0 *	0.02	320 $\mu$ W *	NG	NG	No
[46]	Ca	-32	NG	NG	NG		NG	NG	<5	0.7	No

1. min. Power: Minimum power consumption per sensor

2. RT: Response time (s)

3. DR: Drift rate (mV/h)

4. CMOS Int: All integrated in CMOS

NG: Not Given

\* by calculation from published figures

\*\* Nullified CS with differential meas

CMOS Back-end-of-line post-processing, as proposed in this work, is the most versatile and promising technique for obtaining highly stable core transistors and perform the

surface functionalizing/modifying on top of the interconnect layer of ISFETs. While surface functionalization/modification has been demonstrated both experimentally and theoretically by other groups, here we achieve a 4-analyte functionalization on top of a CMOS chip with excellent combined sensitivity and selectivity by dedicated Ion selective membranes, which is the first result of this kind.

- We generated with the existing sensors the first simultaneous data recording for two different ions within an ultra-small area – showing the outstanding selectivity of our sensors. The design and technology solution that we provided with 3D EMG-ISFET will objectively change the way ISFETs are used in practical applications.
- We demonstrated the functionality of ex-situ sensing of unspiked human sweat samples, with a high repeatability and coherence with established measurement methods.

## Chapter 4 Microfluidic Channel for Sweat Collection and Analysis

---

In this chapter, we introduce the integration of a microfluidic channel on an ISFET sensor chip. The microfluidic channel enables sampling of sweat at a low sweat rate down to 500 nL/min/cm<sup>2</sup>, with extremely low dead volume of < 100 nL, demonstrating drop-to-drop sweat analysis capability. We demonstrate continuous, long-term (> 50 h), low flow rate monitoring through the drop-to-drop modulation of channel impedance. The microfluidic prototype presented in this section is mainly developed by Dr. Fabien Wildhaber and Dr. Erick Garcia Cordero, the conductance and optical measurements are carried out by Mr. Marc Joho and Mr. Pietro Clement. The author's contribution is the idea of leveraging the drop-to-drop resolution characteristics of the microfluidic channel to electronically readout the sweat rate, the theoretical analysis and data processing.

## 4.1 Introduction

Electrochemical sensors have been widely employed for decades, so is the topic of sweat biomarkers' correlation to health status. However, for a long time, researchers who are interested in sweat sensing have been limited to use sweat collection systems (e.g. Macroduct® [121]) or even more complicated methods such as whole body wash down. In the sweat collection methods, sweat is induced (chemically or thermally). 10-300  $\mu\text{L}$  of sweat is collected with a collector, and sent to the hospitals for analysis in a dedicated machine. This kind of separated collecting and analyzing is time consuming, and most of the time not much more attractive than the blood test. Most important of all, the degradation of some biomarkers starts as soon as the sweat is collected.

One of the first demonstrations of a truly non-invasive, continuous monitoring device: a wearable, Bluetooth-enabled flexible sweat sensing band [48] triggered the interest of the community in developing reliable sweat sensors with in-vivo bio-data streaming capability. The sensors in this band are exposed directly to the skin, therefore only suitable for using under very high sweat rate conditions, and for a long time. The first evolution of wearable sweat sensors has been naturally directed to include sweat inducing functions. For example, the same group from Berkeley included a chemical sweat inducing system [122] in the wearable band, in order to achieve rapid sweat collection under motionless conditions. However, questions remain about the biomarker composition of chemically induced sweat versus heat-induced sweat, and no publications to date have characterized analyte variations between the two methodologies.

Therefore, the interest of the community shifted to a more immature yet interesting area of research, i.e. the capillary passive microfluidics. The interest in microfluidics is the promising capability of analyzing a much smaller amount of sweat, at the same time *i.* to protect the sweat from being contaminated and *ii.* to prevent the sensor from being damaged due to direct contact with skin.

In order to develop the microfluidics for sweat collection, let's start with a brief introduction to the sweating mechanism of the sweat gland. Shown in Figure 3-5 is a simplified sketch of the skin cross section showing the structure of human sweat glands. It starts in the hypodermis layer with the secretory coil collecting water from interstitial



fluid due to osmotic pressure. Then it extends through the dermis layer to the epidermis layer, in which the sweat ducts contribute to partitioning of ions, small molecules, and metabolites into the sweat. Finally, the upper coiled duct emerges at the surface of the epidermis, bringing sweat together with the rich bio-information to the surface. However, as soon as sweat gets in contact with the skin surface, it suffers from *i.* evaporation. *ii.* contamination from dead skin cells, microbes, old sweat, etc. *iii.* degradation of biomarkers due to chemical instability. Moreover, many biomarkers' concentrations in sweat are known to be closely related to sweat rate. These made it difficult to accurately analyze sweat composition and its relevance to health. Therefore, it is necessary to develop reliable sweat sampling and analysis techniques that limits contamination and evaporation, while analyzing biomarkers as well as sweat rate at the same time.

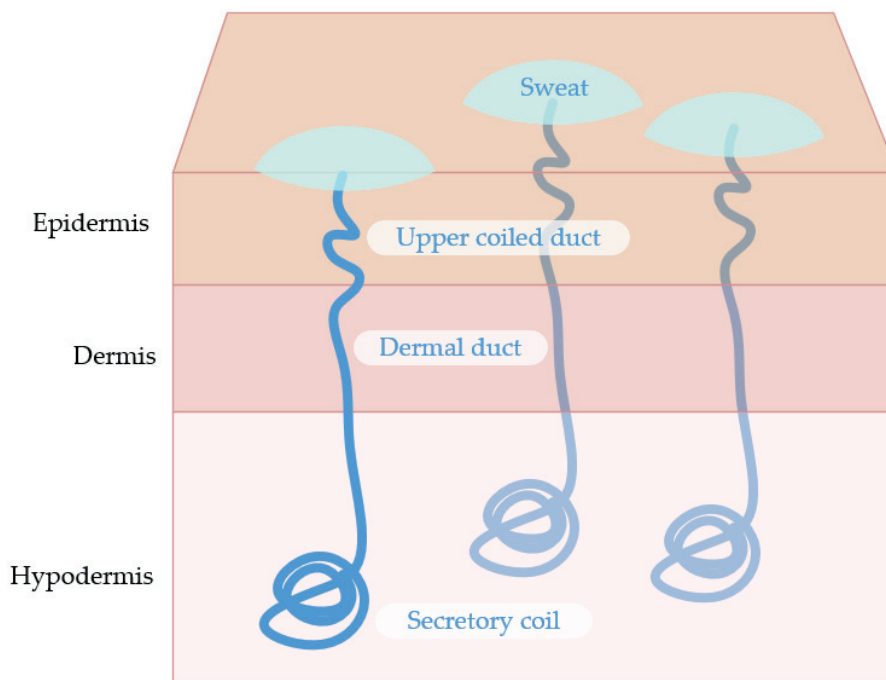


Figure 4-1 Simplified skin cross section showing the structure of human sweat gland. Adapted from [19].

Table 4-1. Figure of merit comparison table for state of the art sweat sensors integrated with microfluidic channel.

Ref	Sensing reservoir volume ( $\mu\text{L}$ ) and material	Collecting reservoir volume ( $\mu\text{L}$ ) and material	Collect reservoir area ( $\text{mm}^2$ )	Continuous functioning time (h)	Dead time (min)	Averaging time (min)	Sweat rate monitor	Results obtained at sweat rate ( $\mu\text{L}/\text{min}/\text{cm}^2$ )	Fluidic size with and without absorbent material ( $\text{cm}^2$ )
[49]	5.9, PDMS	1.3, medical adhesive	13	NG	NG	6	Yes	5.2	NG, 4
[66]	7.8, PDMS	7.8, PDMS	19.6	NG <sup>i</sup> , 1 <sup>ii</sup>	2 <sup>i</sup> , 12 <sup>ii</sup>	10	Yes	2	NG, 6
[123]	80, PDMS	NG, PDMS	NG	0.7	NG	20	Yes	NG	NG, 10
[67]	1.1, hydrophilic plastic film	66, hydrophilic plastic film	660	6 <sup>iii</sup> , 44 <sup>iv</sup>	NG	6 <sup>iii</sup> , 46 <sup>iv</sup>	No	1.6	100, 6.6
[62], [63]	4 $\times$ 10 <sup>-4</sup> , hydrophilic SU-8	10, hydrophilic SU-8	100	NG	1 <sup>i</sup> , 1 <sup>ii</sup>	0.3	Yes	2.5	4, 1
i. Electrolyte sensor;      ii. Sweat rate sensor; iii. Sweat rate = 1.6 $\mu\text{L}/\text{min}/\text{cm}^2$ ;      iv. Sweat rate = 0.2 $\mu\text{L}/\text{min}/\text{cm}^2$ .									

Rapid development in flexible material and micro-fabrication has made it possible for several research groups to realize microfluidics that enable collecting and analyzing of sweat in real-time, with capabilities to limit contamination and evaporation [49], [51], [62], [63], [66], [67], [123], [124]. However, only a few most recent studies demonstrated capability of simultaneous sweat biomarker and sweat rate monitoring. Among them a large proportion are colorimetric sensors [49], [51], [67], [124], which inevitably have the drawbacks such as needs of high amount of sweat to be analyzed, and needs of mixing sweat with specific dyes or fluorescent materials in order to visualize the progress of sweat collection. There also exists electronic methods for monitoring sweat rate, however, operates only at relatively high sweat rate ( $> 1 \mu\text{L}/\text{min}/\text{cm}^2$ ) conditions and within a short period ( $< 1 \text{ h}$ ) [66], [123]. In Table 4-1 we summarize several most representative works and compare the integrated microfluidic channel in terms of size, volume and performance. It is common sense that dead volume is a key parameter that determines the dead time between starting of sweat flow ( $t_F$ ) and starting of sensor response ( $t_S$ ). However, the proper measurement of dead time is not straight forward and has not yet received a unified definition. Among the referenced publications in Table 4-1, [49] did accurately record the start of sweating by colorimetric method, and observed the complete filling of the sensing reservoir in about 6 min, at a flow rate of  $5.2 \mu\text{L}/\text{min}/\text{cm}^2$ . However, the sensors usually start responding earlier than the complete filling [66]. Unfortunately, that paper didn't report the  $t_S$  of their sensors. The authors of [66] reported that sensors started responding 8 min before the complete filling of the sensing reservoir, and dead time was reported to be 2 min, at an average flow rate of  $2 \mu\text{L}/\text{min}/\text{cm}^2$ . The start time of sweating was recorded by simultaneously applying a Macroduct sweat collector to the skin while optically observing the start of sweat flow. However, due to the different sweat collection areas (Macroduct vs. the sensor's collecting reservoir) as well as different collector-skin interface properties, the reported dead time was not accurate. Moreover, there are many factors that can affect the actual dead volume of a sensor, such as sensor surface material, sensor shape, sensor size, fluidic channel material, etc. Therefore, it is not easy to quantify the dead time as a figure of merit to compare different sensors' integrated microfluidics.

However, dead time is positively correlated with another equally important factor, the averaging time ( $t_a$ ), which is the minimum time resolution between old and new sweat. It can be defined and measured more accurately. According to definition, the averaging time is determined by the volume of sensing reservoir ( $V_S$ ), volume of collecting reservoir

( $V_c$ ), Volume of sweat drop ( $V_d$ ), sweat rate ( $v_{sw}$ ), and sweat collection area ( $A_c$ ), by Equation 4.1.

Equation 4.1

$$t_a = \frac{\max\{V_s, V_c, V_d\}}{v_{sw} \cdot A_c}$$

$V_d$  is a parameter determined by the hydrophilicity of skin surface and microfluidic surface, as well as distance between the two surfaces. We can get some intuitive rules of thumb from Equation 4.1 and Table 4-1, about how to decrease  $t_a$ . They are: *i.* minimize the volume of sensing reservoir and collecting reservoir; *ii.* maximize the area of collecting reservoir; *iii.* decrease the distance between the skin surface and collecting reservoir; *iv.* enhance the hydrophilicity of material for the collecting reservoir and microfluidic channels. The first two rules are obvious from Equation 4.1. Yet the third and fourth rules will be made clear with the following discussions.

When a drop of liquid is in contact with a solid surface, there are three phases present at the interface (Figure 4-2): vapor phase ( $v$ ), liquid phase ( $l$ ), and solid phase ( $s$ ). The long-ranged intermolecular forces determine an equilibrium state where the surface tensions ( $\gamma_{sv}$ ,  $\gamma_{lv}$ ,  $\gamma_{sl}$ ) and contact angle ( $\theta$ ) follow the Young's equation:

Equation 4.2

$$\gamma_{sv} = \gamma_{sl} + \gamma_{lv} \cos \theta$$

The surface tension  $\gamma_{sv}$  increases with the hydrophilicity of the solid surface.

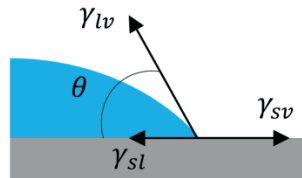


Figure 4-2 Young's equation interpreted as a force balance at the interface.

Therefore, the edge of the droplet forms a certain contact angle (C.A. =  $\theta$ ) with the surface of a certain hydrophilicity. When  $\gamma_{sv} < \gamma_{sl} + \gamma_{lv}$ , the droplet's edge has a finite C.A. with the solid surface. On the other hand, when  $\gamma_{sv} = \gamma_{sl} + \gamma_{lv}$ , i.e. on a very hydrophilic surface, the C.A. is zero and the droplet will ultimately result in a uniform liquid layer covering the whole solid surface [125].

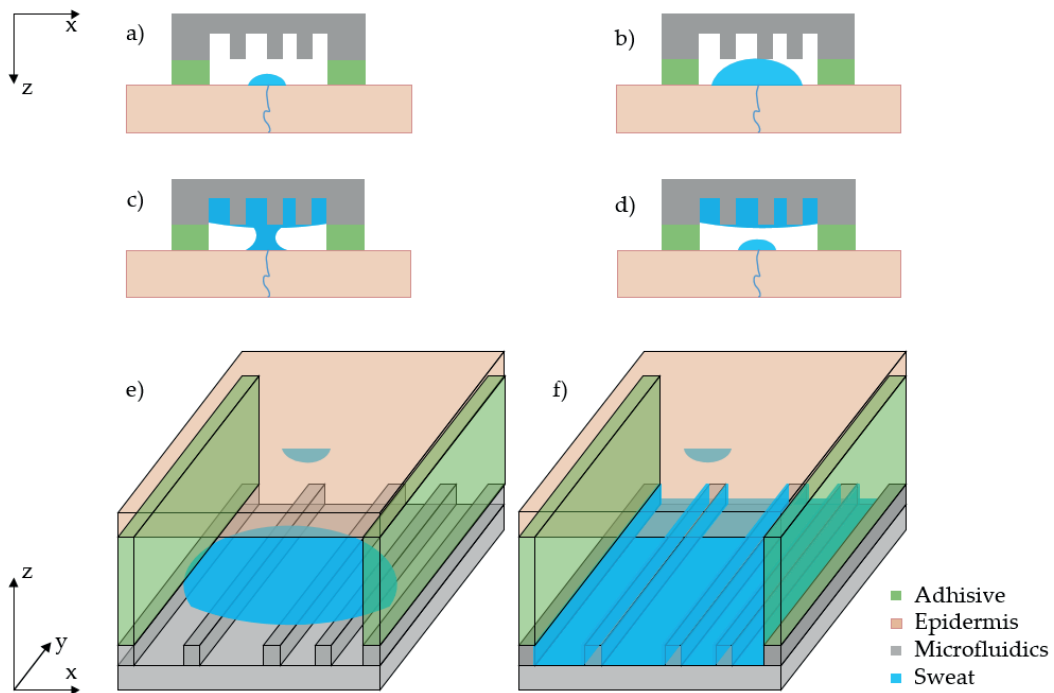


Figure 4-3 Sketch of the microfluidic channel: showing the principle of the passive capillary pump. a) A drop of sweat emerges from the epidermis. b) Sweat drop grows to be in contact with the microfluidic surface. c) Sweat drop forming the equilibrium contact angles on the two surfaces. d) The sweat droplet breaks into two parts: the upper one caught in the channel, the lower one stays on the skin. e) 3-D drawing of the previous subplot (upside down). f) The ultra-hydrophilic channel surface spreads the upper drop evenly in the microfluidic channel.

After learning about the contact angle, we know that when a drop of water is in between two surfaces of different hydrophilicity, it will spread on both surfaces and form different

contact angles at equilibrium state. Figure 4-3 illustrates the behavior of a drop of sweat at the interface of the skin (C. A.  $\sim 40^\circ - 100^\circ$  [126], [127]) and a very hydrophilic microfluidic surface (C. A.  $\sim 0^\circ$ ). A sweat drop emerges from a gland and grows (Figure 4-3a, b). Once it gets in contact with both surface of the skin and surface of the microfluidic channel, the surface energy difference results in surface tension that makes the drop spread on the microfluidic surface (Figure 4-3c). If the spread speed is faster than the sweat growing speed, the sweat droplet will ultimately be separated into two parts (Figure 4-3d, e), one spreads evenly on the microfluidic surface (Figure 4-3f), and the other stays on the skin and grows again for a new droplet. According to ref [128], the spread speed can be optimized by tuning the microfluidic structure as well as material properties.

One may have noticed that, in the conventional understandings of dead volume, as analyzed in [49], [67], researchers calculate the volume of the collecting reservoir ( $V_c$ ) as the dead volume. However, it is not true in the case illustrated in Figure 4-3 and references [67], [129], where *i.* the microfluidic channel is highly hydrophilic; *ii.* the channel-to-skin distance is small enough to allow sweat droplet touch the skin surface before filling up the whole collecting reservoir. If the “evenly spread” sweat droplet can be removed before the next drop forms, then the dead volume should be seen as the volume of the droplet. The removal of sweat is fulfilled by a capillary drain attached at the outlet of the microfluidic channel (to be shown in section 4.3). The drop-to-drop sweat resolution is one of the advanced features of the work to be presented in the rest of this chapter. On top of that, we demonstrate sweat rate monitoring through the drop-to-drop modulation of channel impedance, resulting in sweat-rate-to-frequency-modulation (SRFM) and sweat-rate-to-duty-cycle (SRDC) readout, which we believe are the first reports of electronic methods that are capable of continuously monitoring sweat rate for more than 54 hours.

## 4.2 Results and Discussions

In order to monitor the sweat collection performance in real time with optical microscope, we fabricated a dedicated microfluidic chip on float glass as shown in Figure 4-4a. The microfluidics was designed to be integrated with the sensor chip presented in one of our previously published works [62]. Therefore, we also fabricated another version of the microfluidic chip with conductive routing of a metallic layer made from silver (Figure

4-4b), duplicating the routing of the sensor chip. This chip with metal layer will be used for channel conductance study experiments. The detailed fabrication steps are described in section 4.3.1.

There are two separate yet symmetric microfluidic structures on this microfluidic chip, each consisting of 1) collection zone; 2) delivery zone; and 3) outlet. In fact, the terminology is not exact enough because a drop of sweat can be collected by any part of the channel. But due to the large ratio of collection zone area to the rest of the channel, the assumption that sweat is always collected from the collection zone is valid to the extent of concerns of this work.

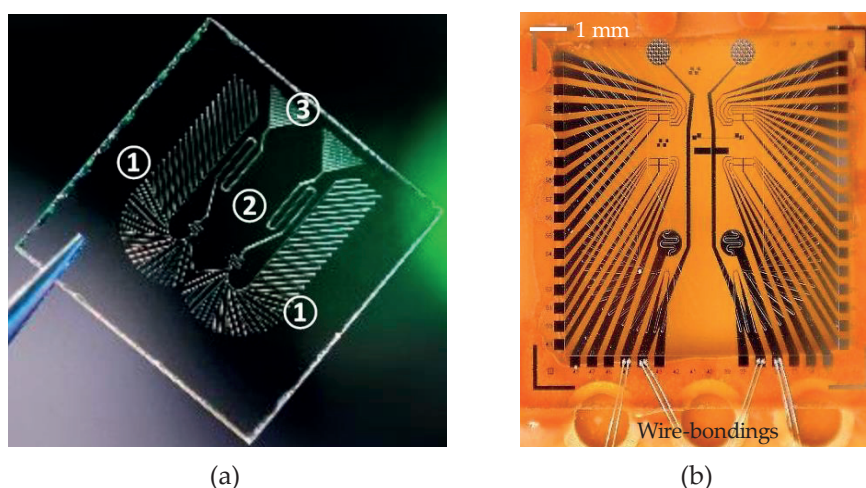


Figure 4-4. SU-8 microfluidic patterned on a glass chip (a) without and (b) with dummy metallic layer.

The microfluidic chip is mounted on a setup to be interfaced with a flow-rate-controllable artificial skin. In this setup, the outlet part of the channel is attached to a piece of drain material. The transport of drops of liquid is monitored continuously with optical method (see details in section 4.3.2). Several snapshots of this transport process at flow rate of 500 nL/min are shown in Figure 4-5.

In Figure 4-5a,  $t = 0$  s, a drop of liquid emerges from the artificial skin and starts to be in contact with the channel surface. In Figure 4-5b,  $t = 0.104$  s, the drop spreads evenly on the



ultra-hydrophilic channel surface. In Figure 4-5c,  $t = 0.325$  s, the drop breaks into two parts and the part that stays in the channel continues spreading, resulting in a slightly lower luminescence in the channel. In Figure 4-5d,  $t = 0.675$  s, front of the drop touches the 'drain', causing the liquid in the channel get sucked, further lowering the luminescence in the channel. At the same time, another drop is forming in the pore.

As expected, the transportation and adsorption of liquid drop take place almost instantly after it touches the channel surface. This phenomenon results in an interesting observation: every drop of liquid is removed before the appearance of the second drop, which is intuitive for the following introduction of sweat rate monitoring method – sweat rate to frequency readout.

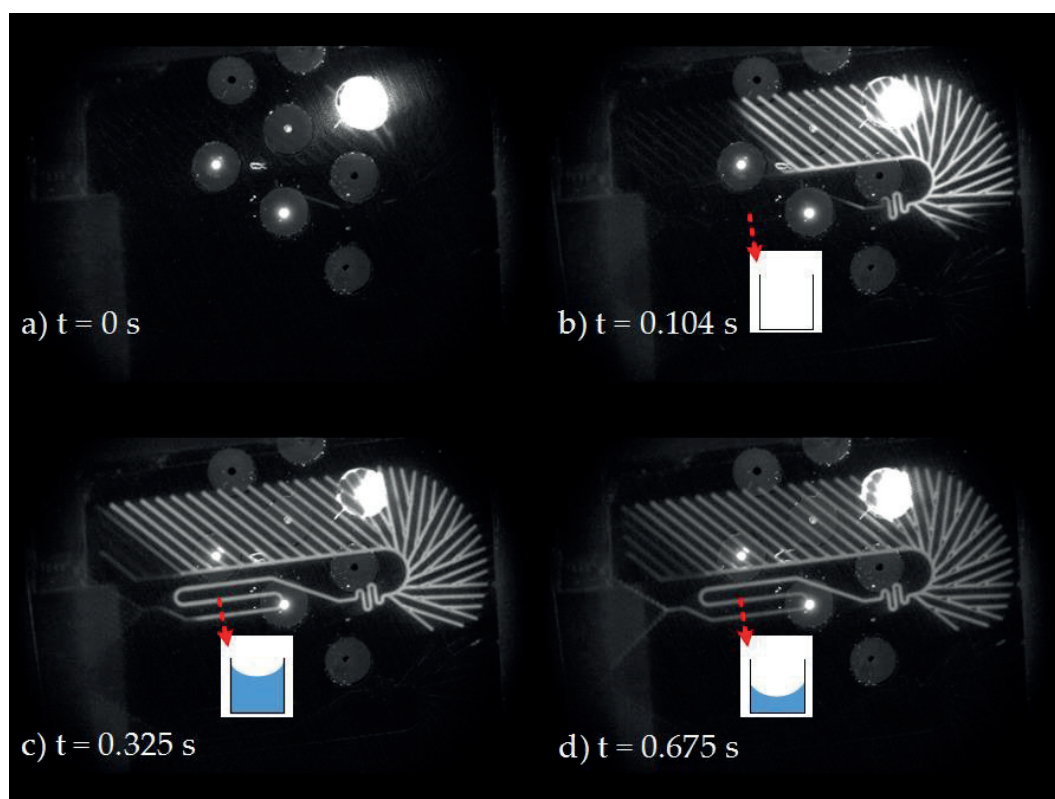


Figure 4-5. Time stamped snapshots of liquid transporting through the SU-8 microfluidic chip.



Next, we are going to monitor the impedance of the fluidic channel. There is one circular Ag electrode situated at each of the 'in' and 'out' ends of the channel's delivery part. Each time a drop of liquid gets collected, it passes through the channel and electrically connects the two electrodes, resulting in a high channel conductance. The absolute value of the channel conductance is modulated by *i*. The ion concentration. *ii*. The liquid depth in the channel (see insets of Figure 4-5c, d). Therefore, when a drop of sweat is transporting in the channel, there are four states of the channel conductance, i.e., low conductance during the formation of a drop before the liquid touches the channel (formation, Figure 4-5a) and during droplet transport until the liquid covers both Ag electrodes (transportation, Figure 4-5b), high conductance when the channel is filled by the droplet (contact, Figure 4-5c), low conductance after the drop is partially removed from the channel by the drain (removal, Figure 4-5d). The channel conductance ( $G_{ch}$ ) is hence modulated periodically, as shown in Figure 4-6a, by the drop formation time ( $t_f$ ), transportation time ( $t_t$ ) and removal time ( $t_r$ ): from  $t = 0$  to  $t = t_t$ ,  $G_{ch}$  is low; from  $t = t_t$  to  $t = t_t + t_r$ ,  $G_{ch}$  is high; and from  $t = t_t + t_r$  to  $t = t_t + t_f$ ,  $G_{ch}$  is low again. In the periodic behavior described above, an assumption was made:  $t_f > t_t + t_r$ , which was always the case in our sweat rate experiments. This assumption is valid because there is always a gap between the epidermal pores and the channel, due to the thickness of skin adhesive material as well as skin roughness, making the  $t_f$  dominating over the capillary driven transportation time  $t_t$  and removal time  $t_r$ .

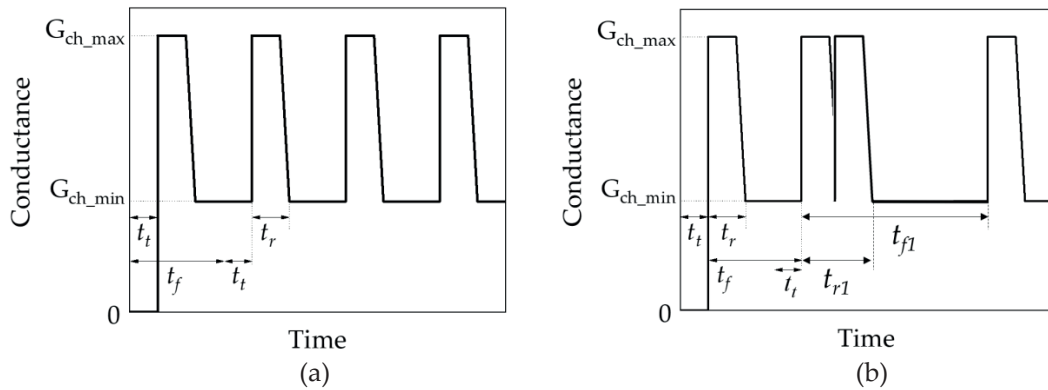


Figure 4-6. Channel conductance periodically modulated by the formation, transportation and removal of sweat droplets.

We are now going to deduct the relationship between sweat rate ( $v_{sw}$ ) and  $t_f$ . Assume that *i.* the hydrophilicity of the skin surface doesn't change over time (constant contact angle  $\theta_{skin}$ ); *ii.* the skin roughness is constant over time (here we assume it is flat to facilitate calculation); *iii.* the effective gap between the epidermal pore and the microfluidic channel is constant over time ( $g_{eff}$ ). With the above assumptions, the droplet is a spherical cap whose height is  $g_{eff}$ . We can calculate the volume ( $V_{drop}$ ) of the droplet at the moment just before it gets in contact with the channel.

Equation 4.3

$$V_{drop} = \pi \times g_{eff}^2 \times \left[ \frac{g_{eff}}{1 - \cos(\theta_{skin})} - \frac{g_{eff}}{3} \right]$$

Therefore,  $V_{drop}$  is a constant.

If only a single pore is sweating, sweat rate  $v_{sw}$  can be calculated from

Equation 4.4

$$v_{sw} = V_{drop}/t_f$$

In Equation 4.4,  $v_{sw}$  is inversely proportional to the droplet forming time  $t_f$  (equals the period of conductance rising edges), or, to put in another way, proportional to the frequency of the conductance variation ( $f_{cond}$ ).

Equation 4.5

$$v_{sw} = V_{drop} * f_{cond}$$

The key assumptions in achieving Equation 4.5 are *i.*  $V_{drop}$  is constant; *ii.* there is only one pore generating the sweat flow. The first assumption can be achieved by fine tuning the channel material and interface properties. However, for the second assumption, in reality,

the microfluidic channel's collection zone covers an area of roughly 0.2 cm<sup>2</sup>. Average sweat gland density on human skin ranges from 100 to 550 per cm<sup>2</sup>[19]. Hence, there are always multiple pores sweating at the same time, and their timings are neither synchronized nor predetermined. This causes the conductance rising edge being masked by the former droplet's falling edge, and results in that the frequency of the  $t_f$  will not follow Equation 4.5 anymore.

An observation is made from Figure 4-6b, when multiple drops mask each other, the required removal time ( $t_{r1}$ ) will experience the same increase as experienced by  $t_{f1}$ , due to the need to remove a larger amount of liquid. Therefore, the duty cycle of the conductance signal will keep unchanged with a certain sweat rate. Equation 4.5 can be modified as below to a sweat-rate-to-duty-cycle (SRDC) relationship, in order to calculate sweat rate for multiple drops, Equation 4.6. It is still valid to single drop scenarios.

Equation 4.6

$$v_{sw} \propto t_r/t_f$$

The key assumption in achieving Equation 4.6 is that the channel is capable to remove droplets of different sizes at constant velocity. This assumption can be achieved by fine tuning the channel structure and material. Therefore, the SRDC method is a more realistic model for sweat rate monitoring. We designed experiments in order to validate the theoretical analysis from Equation 4.5. As shown before in Figure 4-4b, we fabricated a glass chip with patterned SU-8 microfluidic channels and silver (Ag) electrodes to monitor the conductance of the channel. Detailed experiment methods are introduced in section 4.3.2.

We have run the experiment with three glass chips, in order to demonstrate the repeatability. With the first chip (chip #1), we swept the flow rate from 100 nL/min to 500 nL/min, as shown in the right-Y axis plot of Figure 4-7. And the channel conductance is monitored during the sweeping, and shown in the left-Y axis of Figure 4-7. The same sweeping measurement has been repeated continuously over 57 hours, resulting in nine repetitions in total.

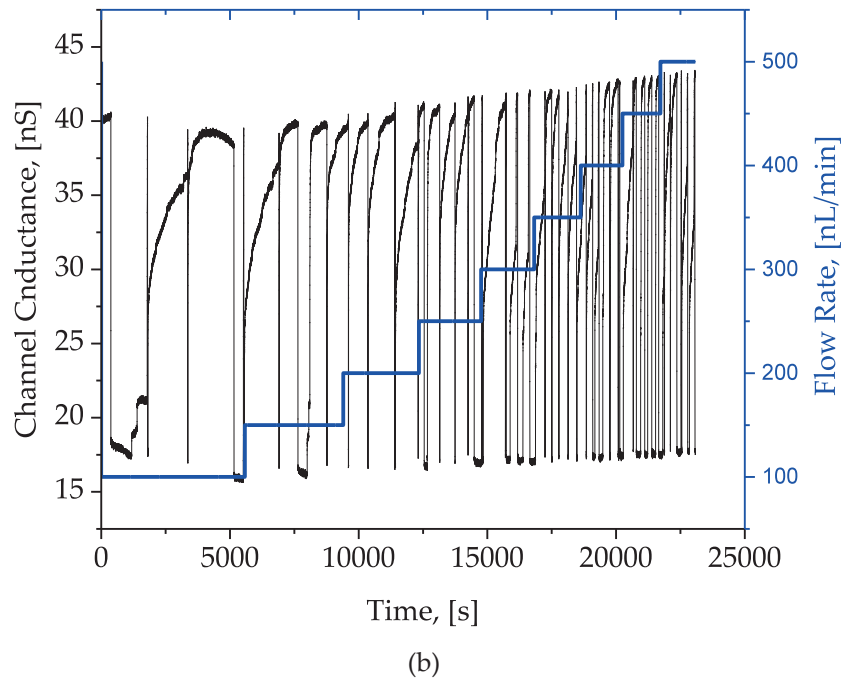
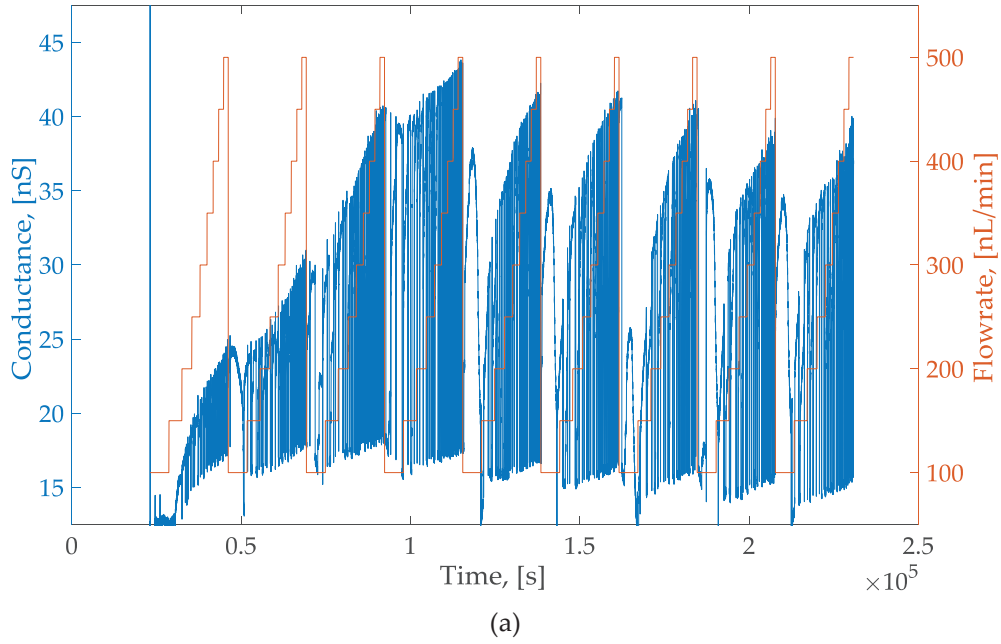
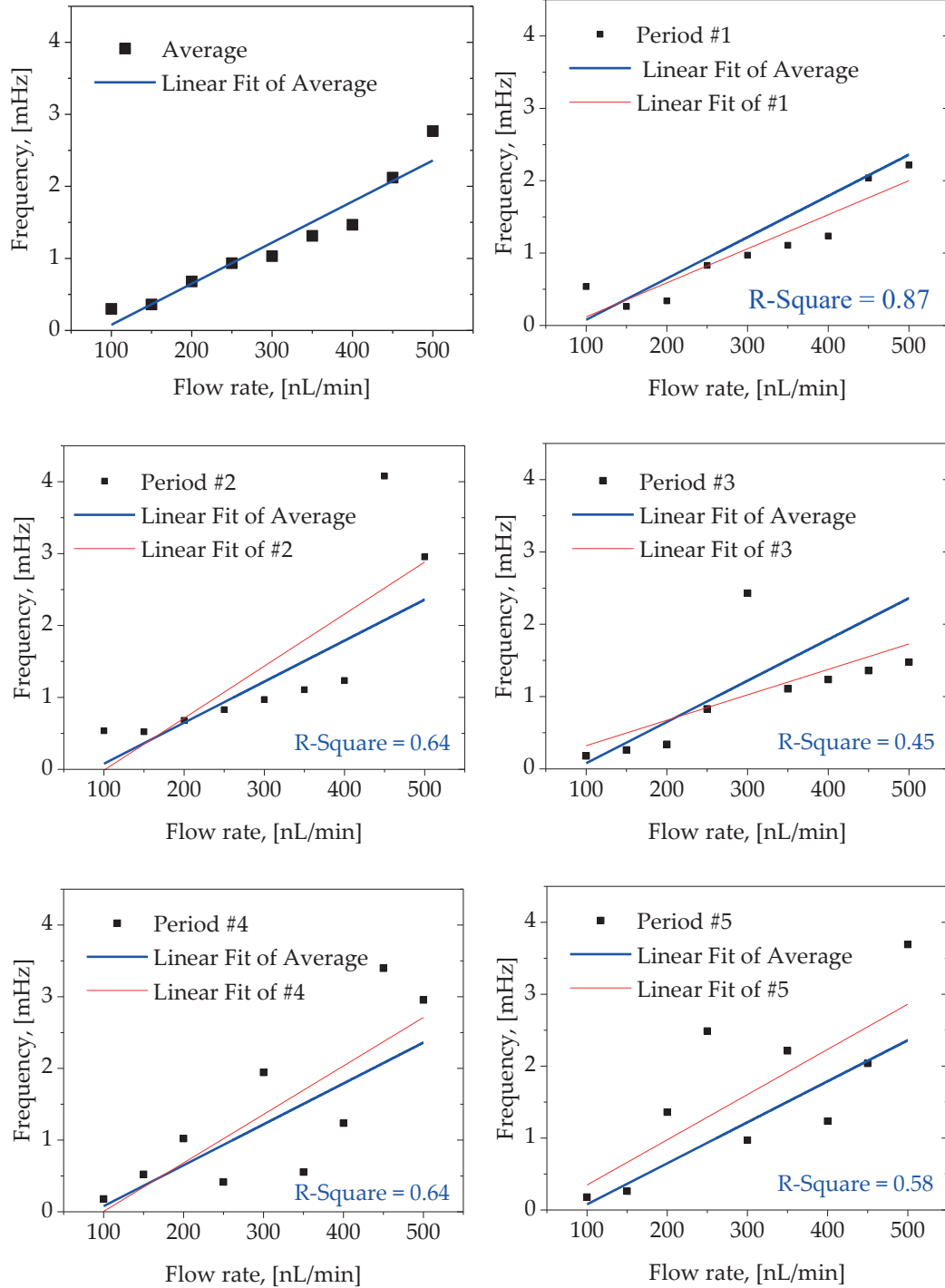


Figure 4-7. Time domain variation of channel conductance, showing that it is periodically modulated by the flow rate from 100 nL/min to 500 nL/min. a) Conductance vs. Time plot for nine repetitions of the sweep. b) Zoom-in of the 4<sup>th</sup> repetition.



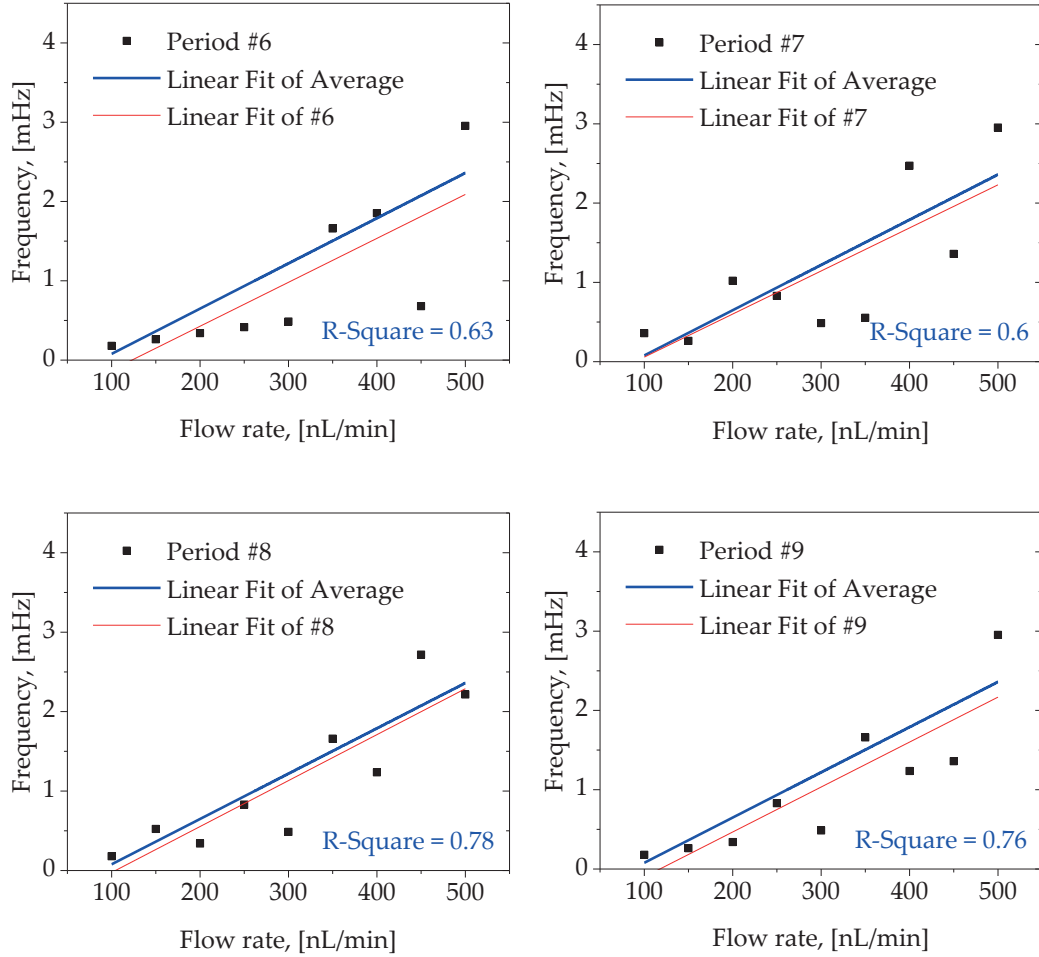


Figure 4-8. Channel conductance variation frequency versus flow rate for every repetition of sweeping of flow rate, showing the flow-rate-to-frequency modulation.

We analyzed data from every flowrate step in the sweeps, and applied Fast Fourier Transform (FFT) to analyze their frequency of maximum spectrum density ( $f_{max\_power}$ ).

With the FFT data processing, we were expecting to derive the  $f_{cond} = f_{max\_power}$ , which is correspondingly modulated by the flow rate, according to Equation 4.5. This has been confirmed by plotting (Figure 4-8)  $f_{cond}$  against flow rate for each period of flowrate sweep (black dots), together with the corresponding linear fitted curves (red lines). The average  $f_{cond}$  (of all the nine sweeps) versus flow rate is also calculated and shown in the

figures as blue lines. The average slope is 0.57 mHz per 100 nL/min of flow rate, and this is defined as the sensitivity ( $S_f$ ) of  $f_{cond}$  to flow rate. Among the nine repetitions of flow rate sweepings, the standard deviation of  $S_f$  is 19.4% with respect to the average value. This is tolerable due to the large range of 'normal' sweat rate and biomarker concentrations.

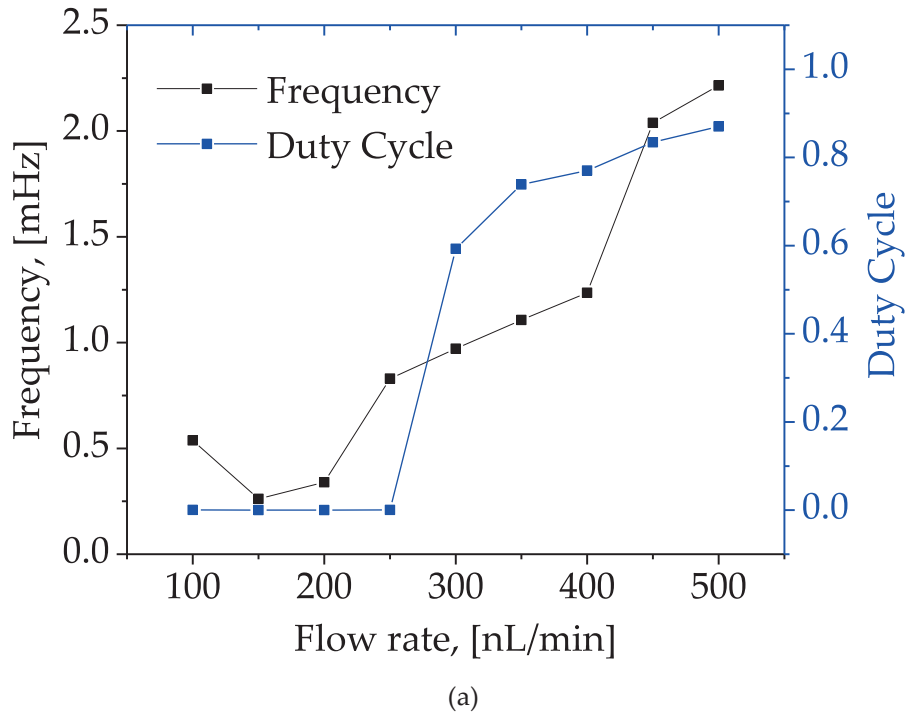
Even though the linear fit of frequency sensitivity is more or less acceptable, we observe that there is large deviation from the  $f_{cond}$  of each sweat rate to the linear fitted line, except the first period (having a coefficient of determination R-Square = 0.87). This is due to gradual change of hydrophilicity, both in the microfluidic channel and on the artificial skin surface. Therefore, oxygen-plasma-treated SU-8 (introduced in section 4.3.1 in order to enhance the channel hydrophilicity) cannot be used for stable microfluidics, but it is still a choice for demonstrating the proof of concept for hydrophilic microfluidic channels. For the same reason, only the results in the first period of flowrate sweep can be considered to be reasonably reflecting the real properties of our concept of sweat-rate-to-frequency-modulation (SRFM) in a hydrophilic microfluidic channel. We ran more experiments with another two glass chips (chip #2 and chip #3), in order to back our theory deduction with more solid proofs.

With the experiment results in Figure 4-9, we are going to make it evident that both the SRFM concept and SRDC concept are valid. First, we analyzed the data from Figure 4-7a, by calculating the duty cycles of the pulsed conductance signal in the first sweep period (period #1), and plotting them against the flow rate on the right-Y axis of Figure 4-9a. Also plotted in Figure 4-9a, is the  $f_{cond}$  versus flow rate, on the left-Y axis. Then with chip #2, we swept the sweat rate from 100 nL/min to 1  $\mu$ L/min, monitored the conductance, calculated its  $f_{cond}$  and duty cycle, and plotted them in Figure 4-9b. Finally with chip #3, the sweat rate was swept from 100 nL/min to 600 nL/min, and the  $f_{cond}$  and duty cycle are plotted in Figure 4-9c. Several observations are made:

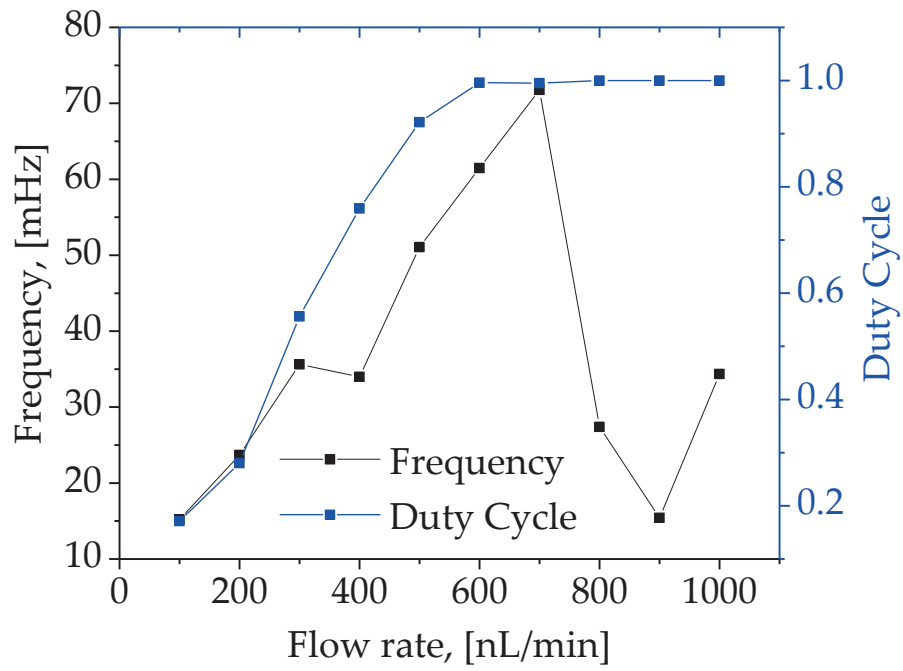
I. At a certain flowrate, the  $f_{cond}$  versus flowrate curves show different frequency values from chip to chip. According to Equation 4.3 and Equation 4.5,  $f_{cond}$  is inversely proportional to  $V_{drop}$  when the flowrate is constant. We can tell from Figure 4-9 that  $V_{drop,chip\#1} \approx 30 * V_{drop,chip\#2}$ . This is caused by non-ideal conditions: *i.* the inevitable error of pore-to-channel distance ( $g_{eff}$ ) due to manual mounting of the drain and adhesive materials. *ii.* the variations of contact angle at the artificial-skin-to-air interface

due to different drop sizes. The latter has been confirmed by our contact angle measurement experiment to be shown in section 4.3.2.

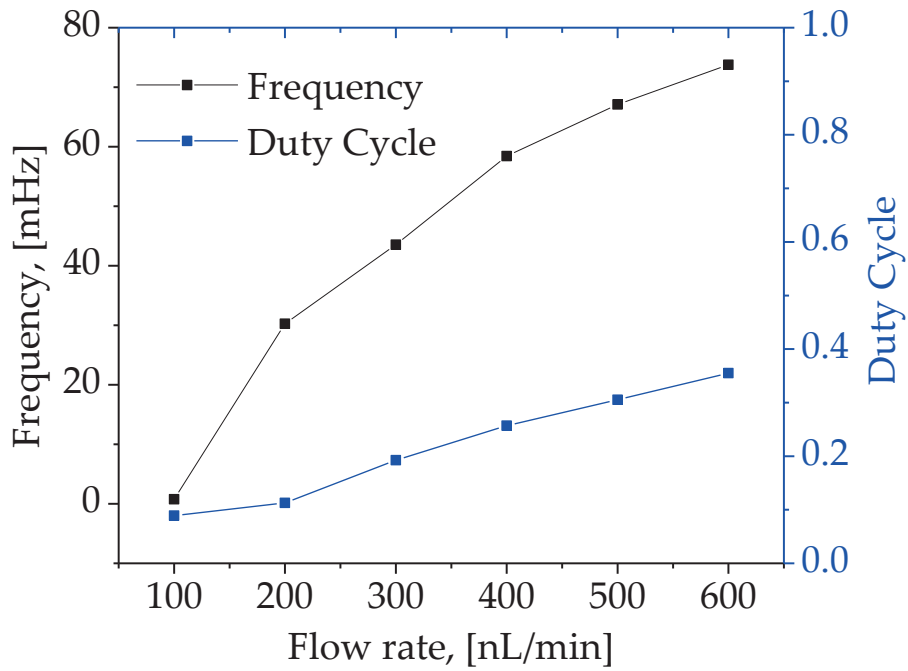
II. The  $f_{cond}$  versus flowrate curves generally show a monotonic increasing trend with increasing flowrate, except that of chip #1 when it is having a flowrate lower than 250 nL/min (Figure 4-9a), and that of chip #2 when it is subject to a flowrate higher than 700 nL/min (Figure 4-9b). The exceptions are again due to the difference in  $V_{drop}$ . The former is explained by the large  $V_{drop}$  in the experiment with chip #1, resulting in  $t_f$  much larger than  $t_r$  when the flowrate lower is than 250 nL/min. Therefore,  $f_{cond}$  could not be accurately determined. This is cross-validated by the duty cycle being zero in Figure 4-9a. The latter is explained by the ‘saturating’ duty cycle. With a flowrate higher than 700 nL/min, the channel of chip #2 is filled by liquid all the time, resulting in an always high channel conductance. The ‘saturating’ due to high flowrate is cross validated by the drop of  $f_{cond}$  and saturation of duty cycle in Figure 4-9b.







(b)



(c)

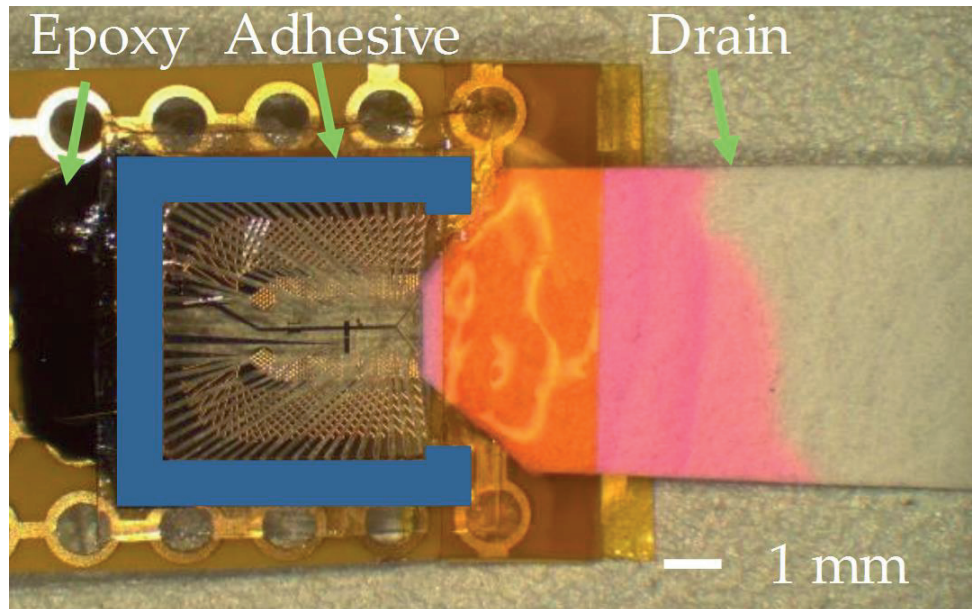
Figure 4-9. Channel conductance variation frequency versus flow rate for every repetition

## 4.3 Methods

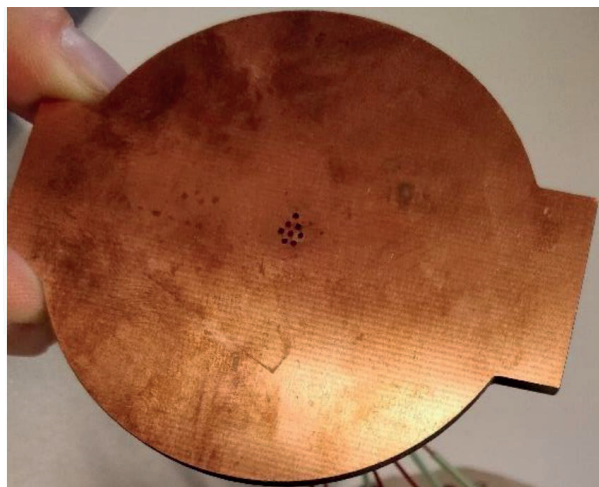
In this section, we introduce the fabrication processes as well as experimental methods for the results presented in this chapter.

### 4.3.1 Fabrication methods for the glass microfluidic chips

The fabrication steps of the glass chips have been discussed in detail in our previous publications [62], [63], therefore only a brief introduction is presented here. The fabrication process begins by pretreatment of a float glass wafer (Diameter: 100 mm, Thickness: 550  $\mu\text{m}$ , Resistivity:  $10^{9.7}$  [ohm.cm] @ 100 Hz, 25 °C, amorphous). In this step, the wafer is exposed to an  $\text{O}_2$  plasma treatment in a Tepla 300 machine (400 ml/min, 500 Watt power for 7 minutes). Afterwards, the Ag electrodes, wires, and pads (100 nm thickness) are fabricated through liftoff process on the float glass wafer. Subsequently, a 3  $\mu\text{m}$  passivation layer made of SU-8 (Gersteltec GM1050) is patterned on the wafer through photolithography. Only the peripheral pad ring and areas of the Ag electrodes are not passivated. Finally, a second layer of SU-8 (25  $\mu\text{m}$ , Gersteltec GM1070) is patterned via photolithography, on top of the passivation layer, in order to form the microfluidic channels. The channel width is 50  $\mu\text{m}$ , chosen after optimization. Ultra-hydrophilicity of the channel is achieved through short oxygen plasma treatment to the microfluidic chip.



(a)



(b)

Figure 4-10. Experiment setup. (a) The microfluidic chip wire-bonded to a flexible printed circuit board (PCB), attached to (b) artificial skin, with adhesive material as sealing and drain material to ensure a constant removal of liquid. The pink color is due to the drain material having absorbed drops of liquid containing a fluorescent dye.

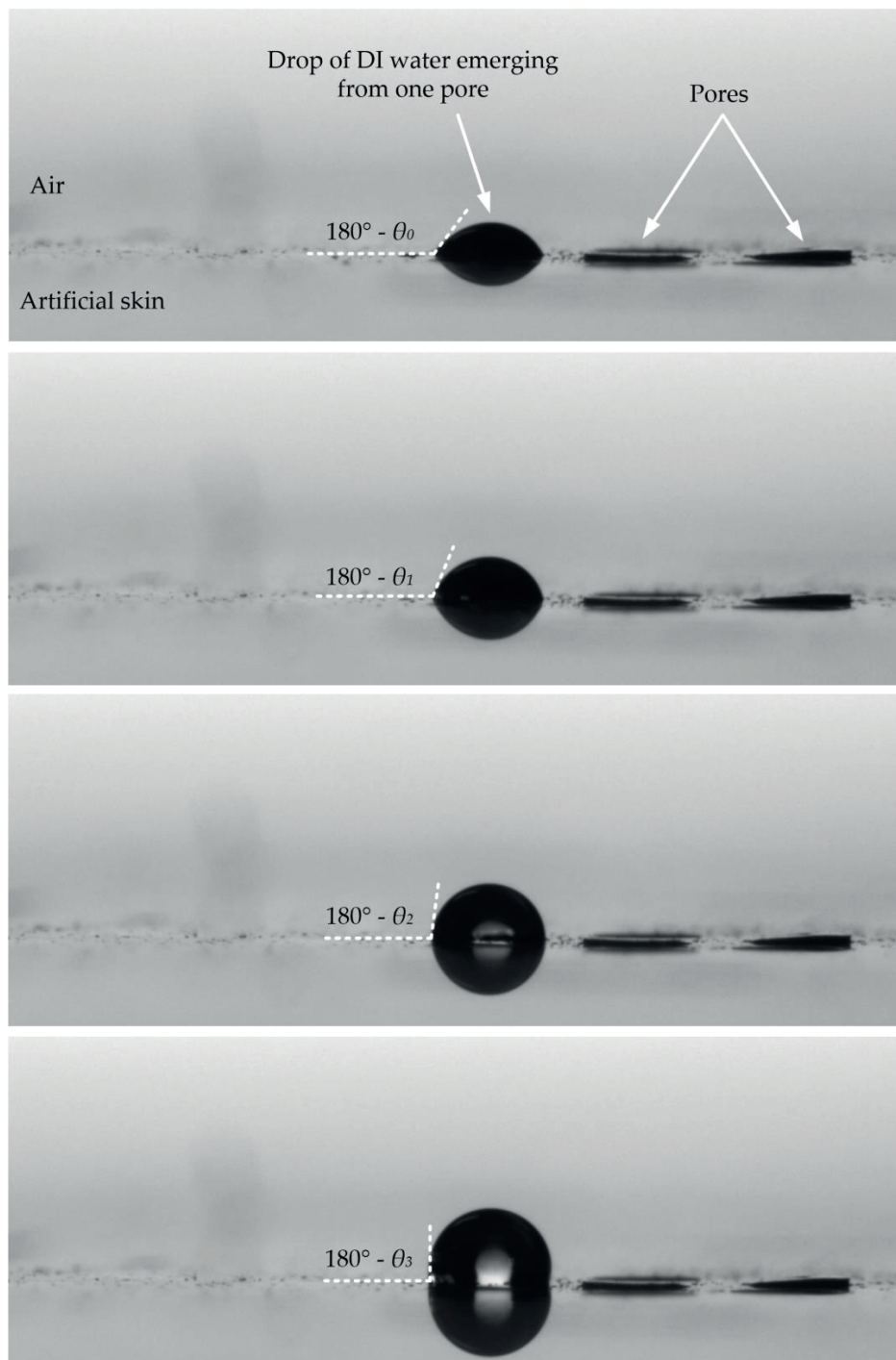


Figure 4-11. Artificial skin contact angle measurement, for different droplet sizes of DI water.

### 4.3.2 Experiment methods

The chip is wire-bonded on a flexible PCB (shown in Figure 4-4b), in order to make electrical connections from the Ag electrodes to an LCR meter. After passivation with epoxy (to protect the wire-bonds), a piece of drain material (thickness: 380  $\mu\text{m}$ ) is applied to the outlet part of the channel, while the rest of the chip's peripheral is covered by adhesive material (thickness: 100  $\mu\text{m}$ ). This setup is shown in Figure 4-10a. Then, this setup is adhered to a flowrate-controllable artificial skin (Figure 4-10b), with the aid of the adhesion material. The artificial skin is made of polymer and coated with copper. It has 8 pores with inner diameter of 250  $\mu\text{m}$ , and density of 20 pores /  $\text{cm}^2$ . In the experiments concerned in this work, all the liquid flow is conducted through one pore that is placed below the collection zone of the microfluidic chip (with a distance equal to  $g_{eff}$ ). This is emulating an extreme situation which isn't likely to happen in on-body tests, because there is always more than one pore sweating at the same time. However, this simplified experiment could result in more intuitive results in preliminary researches. Since only one pore is flowing liquid throughout our experiments, the flowrates in this work are addressed with a unit of nano-Litre per minute (nL/min). If the readers need to compare with standard unit, which is usually expressed in nL/min/ $\text{cm}^2$ , they should consider dividing the nL/min values by the half of the area surrounded by the adhesive and drain materials ( $\approx 0.2 \text{ cm}^2$ ). Since there are two symmetrical separate collection zones in the chip, that half area is approximately the area of a single collection zone.

In the optical fluorescence monitoring experiments, we flipped the experiment setup described in Figure 4-10, facing the backside of the microfluidic chip towards the objective of an inverted fluorescence optical microscope (Zeiss Axiovert 200). We deliver constant flow of liquid under test (LUT) through the pore(s) of the artificial skin. The LUT is DI water pre-mixed with a fluorescent dye (absorption peak: 553 nm, concentration: 100  $\mu\text{M}$ ), in order to monitor fluidic behavior through fluorescence. At the same time, the optical monitoring results were recorded in the form of a video. Typical fluorescent results are as shown in Figure 4-5, the higher light intensity corresponds to larger amount of fluorescent dye, i.e., more LUT.

In the conductance measurement experiments, we connected the wire-bonded pads to an LCR meter, and measured the channel conductance value by applying an AC voltage

(amplitude: 0.5 V, frequency: 1 kHz) to the ‘two-terminal’ channel resistor. The time dependent behavior of the conductance is recorded at a sampling frequency of 10 Hz.

We tested the contact angle of the artificial skin with Krüss DSA-30 Drop Shape Analyser. A constant flow of DI water was delivered from the automatic dispense system of Krüss DSA-30, through one of the pores embedded in the artificial skin, onto the skin-air interface. At the same time, we monitored the forming of the droplet on the artificial skin, and recorded this process in a video. This experiment was designed in order to keep the surface condition of the skin-air interface property maximally similar to that in our channel conductance measurement experiments. Snapshots of this process are shown in Figure 4-11, from where we can see that the contact angle increases as the droplet size grows.

## 4.4 Conclusions

In this chapter, we investigated a microfluidic pattern that has been directly integrated with an ISFET sensor chip in our previous publications. We focused on leveraging the drop-to-drop resolution of our ultra-hydrophilic passive microfluidic channel, for developing continuous, real-time, electronic readout of sweat rate. The microfluidics introduced in this chapter has counteracted the following technical and scientific challenges:

- Ultra-low dead volume of less than 100 nanoLiters, which is highly demanded for on-body sensing in low physical activity conditions.
- Capability of long term, real-time and continuous monitoring sweat rate via electronic methods.

We analyzed the sweat-rate to channel conductance variation, introduced novel and intuitive principles for reading sweat rate via the frequency and duty cycle of conductance variations, of hydrophilic microfluidic channels. We made the first, to the best of our knowledge, experimental demonstrations of two novel electronic readout methods for reading sweat rate.

- Sweat-Rate-to-Frequency-Modulation (SRFM)
- Sweat-Rate-to-Duty-Cycle (SRDC)

Experimental results were obtained with an artificial skin delivering liquid at certain rate through a single pore that is placed below the microfluidic channel, proving that both frequency and duty cycle of the channel conductance signal are positively correlated to the sweat rate. Future work should concern the following:

- Enhance the hydrophilicity property of the microfluidic channel by functionalization, in order to preserve the hydrophilicity for a longer period of time.
- Study the SRDC modulation in conditions where artificial skin is delivering liquid through multiple pores.
- On-body test for simultaneous monitoring sweat rate and sweat biomarkers.





## Chapter 5 Readout Circuits

---

This chapter introduces the circuits designed for ISFET sensor and sweat rate readout. The current outputs from 3D-EMG-ISFET CMOS chip characterized in Chapter 3 and the microfluidic channel conductance in Chapter 4 are targeted as the sensing signals to be read. In the first part, typical readout schemes for ISFETs are briefly introduced. After that, an ASIC with integrated multiplexer and current readout circuitry is designed for reading out ISFETs. A wearable sensor patch, wirelessly powered through Near Field Communication (NFC), is developed to demonstrate the readout capability. Finally, an implementation of sweat rate to frequency readout circuit is introduced.

In this chapter, the Android application for NFC communication is developed by Mr. Michael Heiniger and Mr. Bilguun Chinzorig, the microcontroller programming is done by Mr. Jérémie Willemin. The author's contribution is the design, simulation and measurements of the ASIC as well as the in-vitro measurements of the wearable system.

## 5.1 Typical Readout Circuits for ISFETs

There are two basic types of readout circuits for ISFETs: 1. Source follower readout. 2. Transconductance readout.

A typical source follower readout circuit is shown in Figure 5-1. The reference terminal voltage ( $V_{ref}$ ) is fixed, voltage across the resistors  $R_1$  and  $R_2$  is also a constant  $V_R$ . Since the negative feedback loop of the operational amplifier (OPA) tend to keep  $V_+ = V_-$ , the voltage across  $R_3$  is  $V_{R3} = V_{R1} = V_R * R_1 / (R_1 + R_2)$ . Therefore, the drain current is fixed to  $I_D = V_{R3} / R_3$ . So is the drain-to-source voltage ( $V_{DS}$ ),  $V_{DS} = V_{R2} = V_R * R_2 / (R_1 + R_2)$ . The bias conditions above is an equivalent of setting a source follower bias condition for MOSFETs, resulting in the source voltage ( $V_s$ ) to follow the change in the  $V_G$ . The definition of  $G'$  is the same as in Chapter 2. This is a popular readout type that many commercialized ISFET products adopt [99], [130], and the fact that ISFETs convert the high impedance of SS-ISEs into a low impedance output voltage ( $V_s$ ) at the source terminal of a transistor makes ISFETs less susceptible to noise. However, there are several limitations in it. One is that in commonly adopted low cost single well CMOS processes, the bulk of N-type MOSFETs should always be connected to ground to avoid latch-up [131]. That means the bulk terminal (not shown in the circuit) of the ISFET should always be connected to the ground. Another limitation is that the bulk of the device needs to be connected to the source, in order to eliminate any back-gate influence, i.e.,  $V_{SB}$  influences  $I_D$  (according to Equation 2.10). These two limitations end up in a limited choice of foundry CMOS processes for the fabrication of ASICs containing ISFET sensors.

The other type of readout circuit, the transconductance readout, is based on the measurement of  $I_D$  under constant voltage biases. As shown in Figure 5-2, the voltages at the terminals of the ISFET are all biased with constant DC voltage source. The change  $I_D$  is then only reflecting the change in the solution-membrane interface  $G'$ . In this case, the ISFET is configured as a transconductance amplifier, converting the electrochemical potential into a component of the drain current. For the sake of lowering power consumption,  $I_D$  is required to be as low as possible. So the readout circuits are usually designed to make a trade-off between data acquisition time and noise rejecting capability. In the readout circuit shown in Figure 5-2,  $I_D$  is converted into a voltage with an active integrator. With the integrator, high frequency noises are rejected due to the low pass filter nature, and white noise is suppressed.

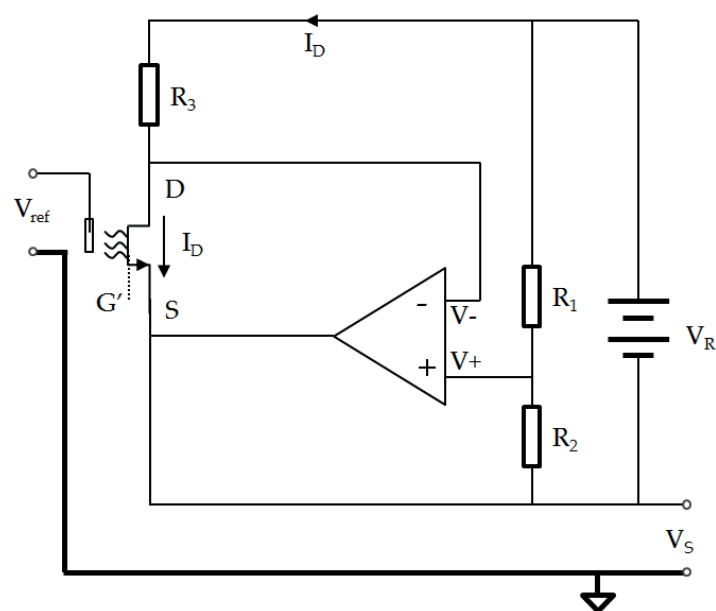


Figure 5-1 One type of readout circuit for ISFET: source follower readout.

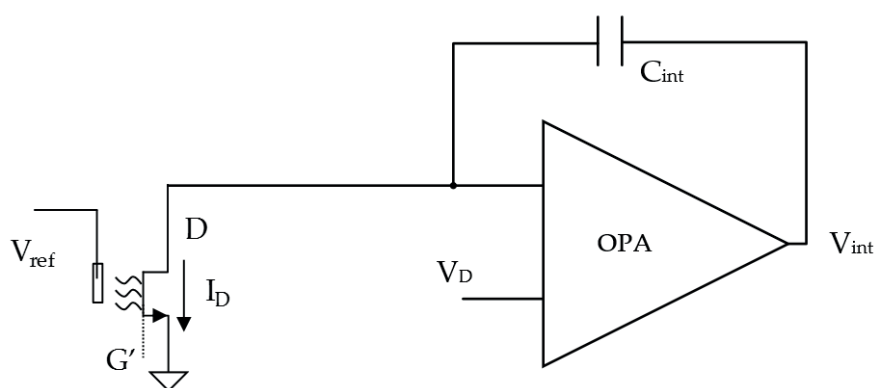


Figure 5-2 Another type of readout circuit for ISFET: Transconductance readout.

## 5.2 Multiplexed current readout implementation

In this section, we are going to introduce the implementation of transconductance readout circuit for the ISFETs characterized in Chapter 3.

### 5.2.1 Block diagram

The block diagram of the ASIC (Application-Specific Integrated Circuit) implementation is shown in Figure 5-3. We fabricated an ASIC in a CMOS 0.18  $\mu\text{m}$  process. The design of each consisting block will be detailed in sections 5.2.2 – 5.2.5. Now we are briefly introducing the overall function of the ASIC. It is consisted of an ISFET array, a 16:1 multiplexer (MUX), and an active integrator. The multiplexer is consisted of 16 CMOS switches, digitally addressable to connect one of the inputs to its output terminal. Each of the input terminals is connected to the drain of one ISFET in the array. The output of the MUX is connected to the active integrator.

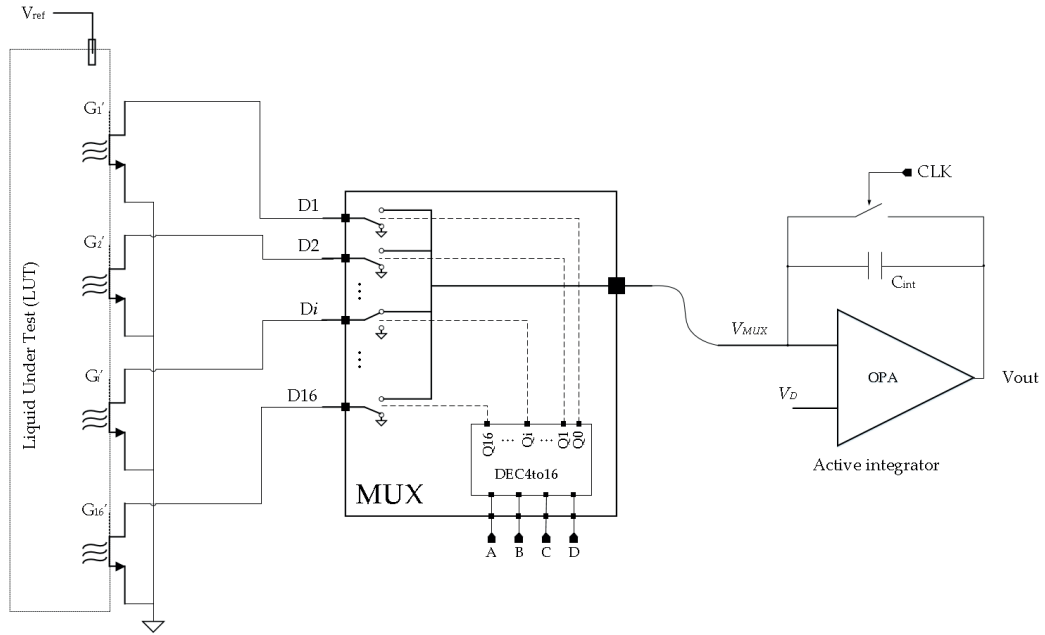


Figure 5-3 Block diagram of the ASIC implementation for the transconductance readout.  $G'_i$  is the liquid-to-sensing membrane interfaces,  $D_i$  is the drain terminal of the  $i$ th ISFET,  $i = 1, 2, \dots, 16$ .

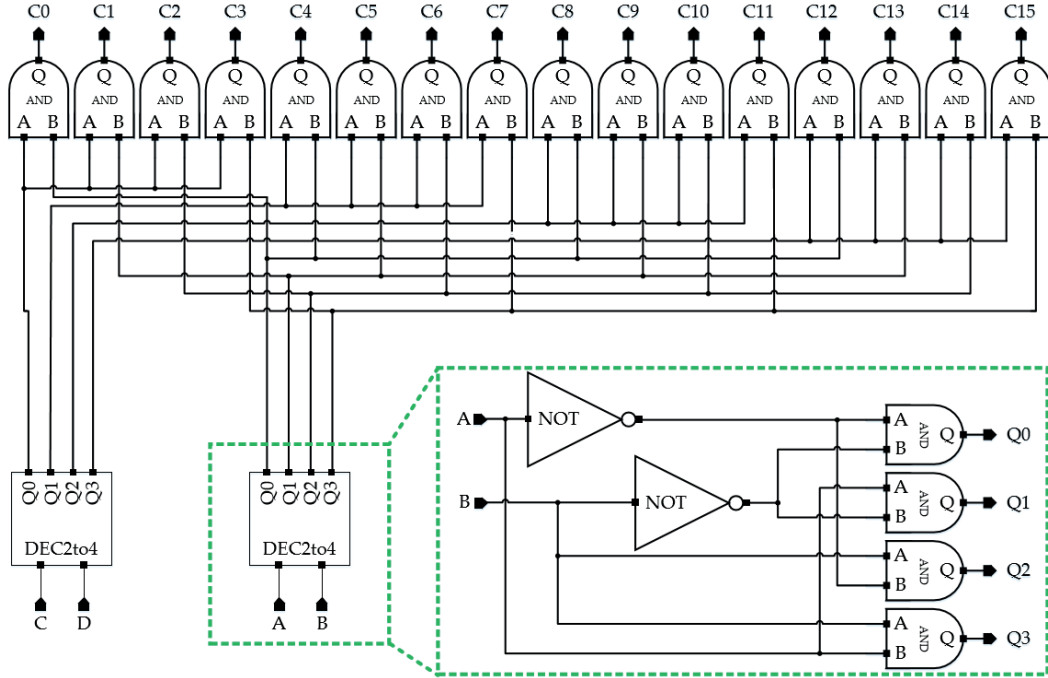


Figure 5-4 MUX implementation with CMOS gates

In the active integrator, an OPA is configured in feedback mode with a capacitor ( $C_{int}$ ) and a single pole single throw (SPST) switch connected in parallel, forming the feedback path. When the CLK signal is high, the SPST switch turns on, so that the drain voltage ( $V_{Di}$ ) of the selected ISFET  $i$  and the output voltage  $V_{out}$  is set to be equal to  $V_D$ . When the CLK signal gets low, the SPST switch turns off, the drain current ( $I_D$ ) starts integrating on  $C_{int}$ . Since the negative input of the OPA is kept constant equal to  $V_D$ ,  $V_{out}$  is determined by the  $I_D$ ,  $C_{int}$ , and time of integration ( $t$ ), through the equation below:

Equation 5.1

$$V_{out} - V_D = \frac{1}{C_{int}} \int_{t=0}^{T_{CLK}} I_D dt$$

In which,  $T_{CLK}$  is the period of the CLK signal. The switch is periodically reset by the CLK signal in order to avoid saturation of the  $V_{out}$ .  $V_D$  is generated by resistive dividing from a bandgap reference voltage generator (introduced in section 5.2.5).

Since  $I_D$  is correlated to the ion activity at the solution-sensor interface, Equation 2.7 - Equation 2.10, we can monitor the  $V_{out}$  and convert it back to the ion activity.

### 5.2.2 Multiplexer (MUX)

The 16:1 MUX is designed with a 4-to-16 decoder and 16 SPDT (single pole double throw) CMOS switches. The 4-to-16 decoder is realized with CMOS gates (AND and NOT), as shown in Figure 5-4. The digital inputs of the decoder are terminals A, B, C, D. They are decoded into a 16-bit digital output code ( $C<0:15>$ ), with only one digit being high at a time. Each of the digital outputs is connected to a single pole double throw (SPDT) CMOS switch (Figure 5-6).

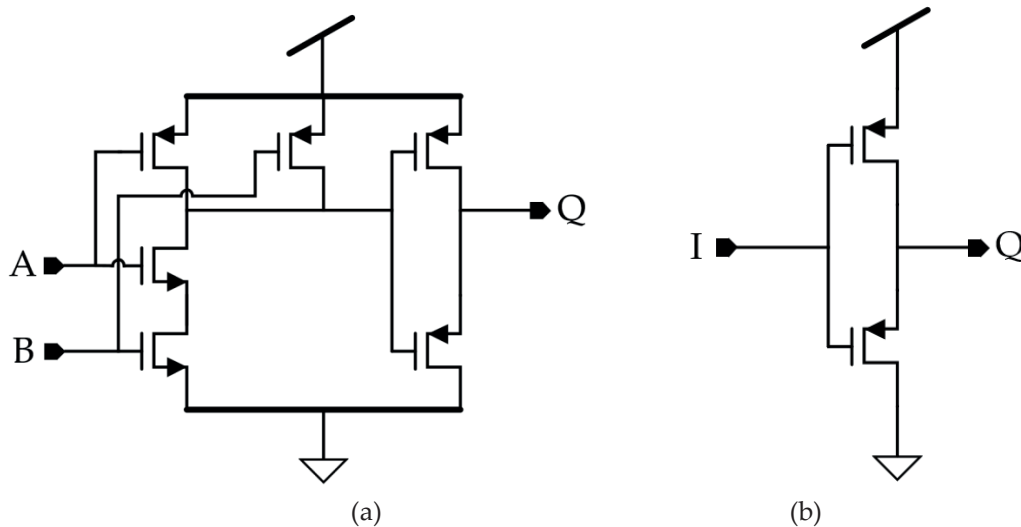


Figure 5-5 Implementation of a) AND and b) NOT gates

The design of AND gates and NOT gates are realized with CMOS configurations, as shown in Figure 5-5. The AND gate is realized by connecting a NAND gate and an

inverter in series, in order to provide a buffered digital output 'Q'. The NOT gate is realized with an inverter.

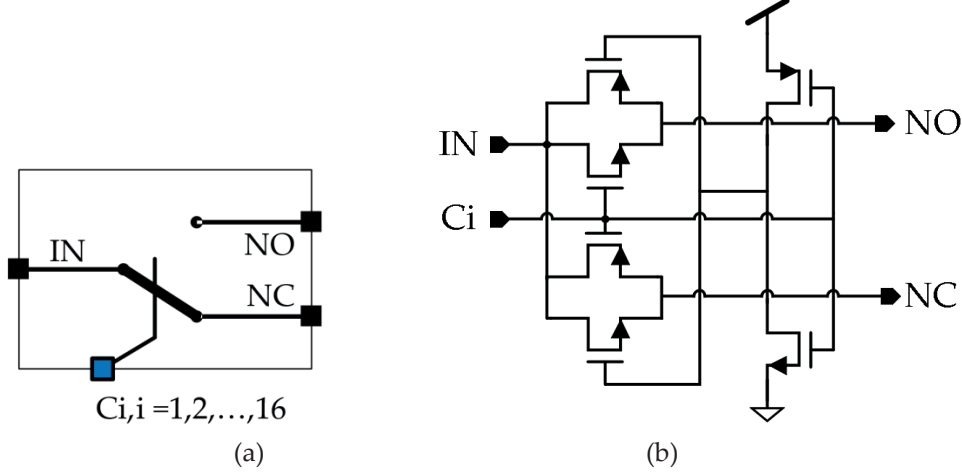


Figure 5-6 Implementation of CMOS SPDT switches, a) block diagram, b) CMOS circuit

The SPDT switches in the MUX are realized with a circuit shown in Figure 5-6b. The analog input is connected either to NC (normally connected) or NO (normally open) terminal, when the digital input  $C_i$  is either '0' or '1', respectively.

### 5.2.3 Current source

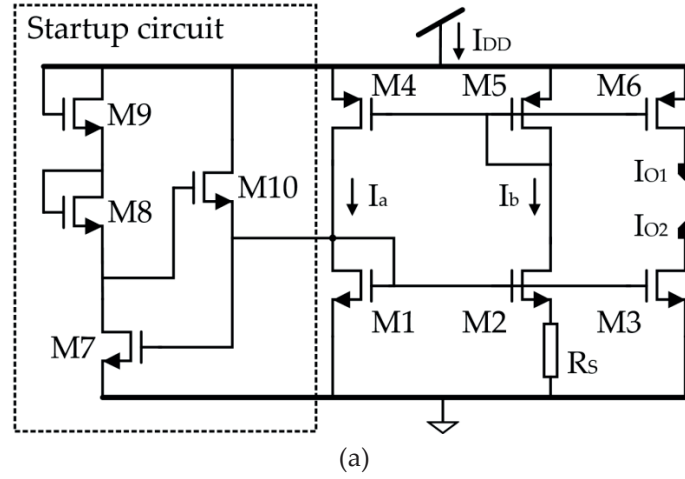
The current sources are realized with a Beta-multiplier structure as shown in Figure 5-7a. It is consisted of a startup circuit and a supply-independent current generating circuit. Since we need very low power consumption in our application, we are designing the current generating circuit with the MOSFETs operating in weak inversion. In this case, the output current is related to the design parameters through the following equation:

Equation 5.2

$$I_{O1} = I_{O2} = I_a = I_b = \frac{U_T \ln(k)}{R_S}$$

In which,  $U_T$  is the thermal voltage,  $k$  is the ratio of transistor M2 over M1.

The current generating circuit has two stable states, *i.* the output current  $I_a = 0$ ; *ii.*  $I_a = \frac{U_T \ln(k)}{R_S}$ . Therefore, a startup circuit is designed to always drive the circuit away from state *i.* When  $I_a = 0$ , the gate-to-source voltage of transistor M1 ( $V_{GS,M1}$ ) is 0, making  $V_A = 0$ . The voltage  $V_A$  being zero turns off the transistor M7, resulting in zero current through the branch consisting of M7, M8 and M9. Hence,  $V_{GS,M8} + V_{GS,M9} = 0$ . This results in  $V_B = V_{DD}$ . Therefore, M10 is turned on, and  $V_A$  is pulled up to a value close to  $V_{DD}$ . This results in a 'non-zero'  $I_a$ . The design parameters of all the MOSFETs are listed in Figure 5-7b.



	W ( $\mu\text{m}$ )	L ( $\mu\text{m}$ )
M1, M3	40	5
M2	160	5
M4-M6	40	5
M7	40	5
M8-M10	1	0.5

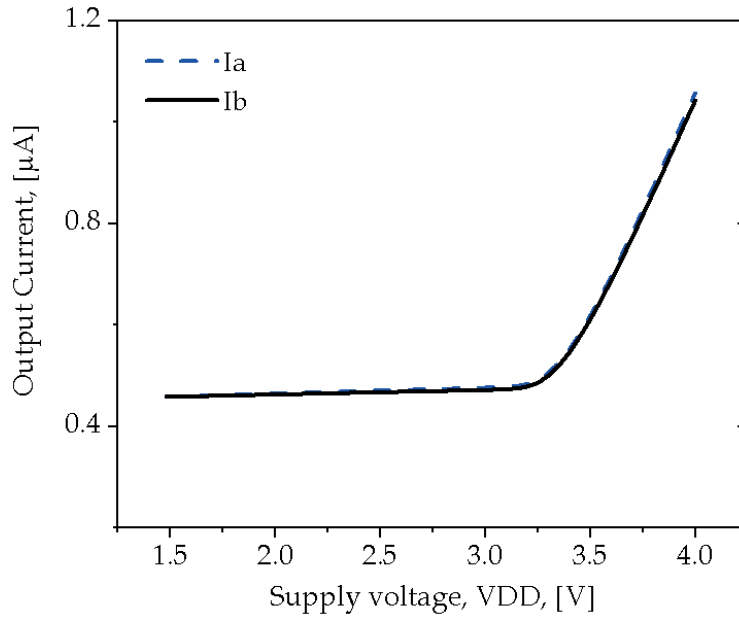
(b)

Figure 5-7 Beta-multiplier current source. a) Schematic diagram. b) Design parameters of the circuit,  $R_S = 100 \text{ k}\Omega$ .

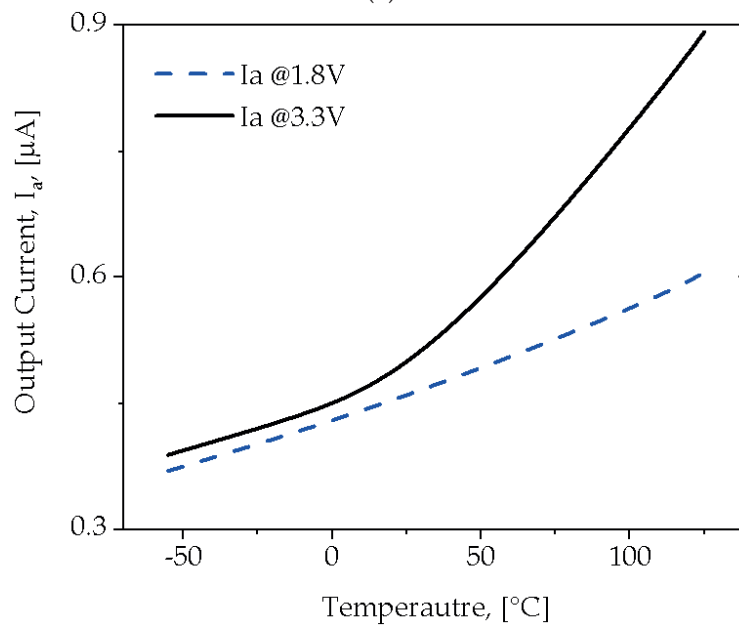
The simulation results for the current source are shown in Figure 5-8. When the supply voltage varies from 1.8 V to 3.3 V, the output current varies from 462 nA to 505 nA, showing a supply voltage resistivity of  $\Delta V_{DD}/\Delta I_{a,b} = 34.9 \text{ M}\Omega$ . The output current's



temperature sensitivity is 7203 ppm/°C at  $V_{DD} = 3.3$  V, and 3554 ppm/°C at  $V_{DD} = 1.8$  V. The supply current  $I_{DD} = 1.6$   $\mu$ A when  $V_{DD} = 3.3$  V at room temperature.



(a)



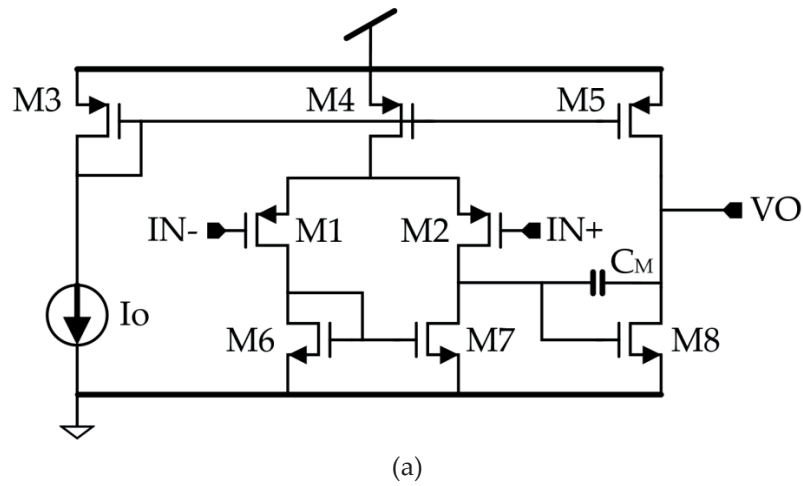
(b)

Figure 5-8 Simulation results of the Beta-multiplier current source. a) Output current varying with supply voltage. b) Output current varying with temperature.

### 5.2.4 Operational amplifier (OPA)

The OPA is realized with a two-stage topology Figure 5-9b, stabilized by miller compensation capacitor. The bias current  $I_0$  is generated from a Beta multiplier. The simulation results of the OPA's key performances are listed below and shown in Figure 5-10.

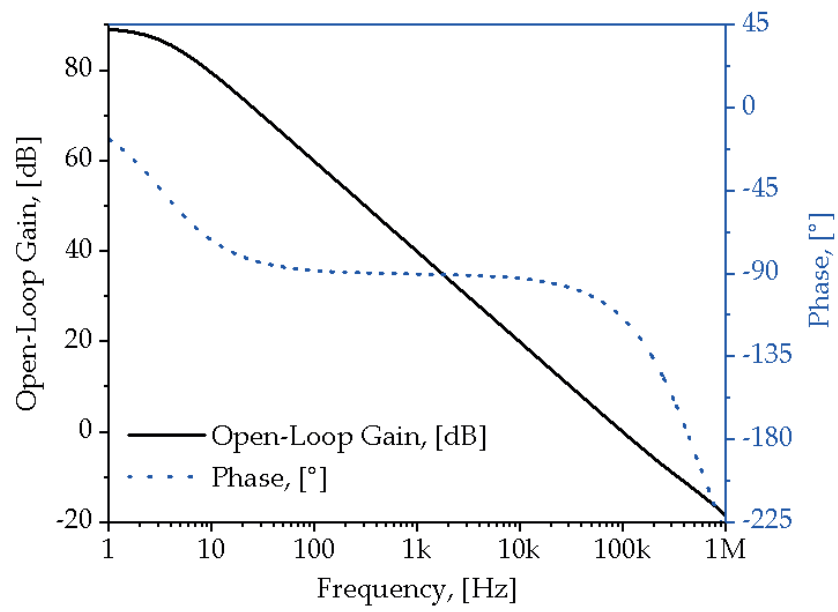
- Quiescent current:  $3.8 \mu\text{A}$  @  $V_{DD} = 3.3 \text{ V}$ ,  $25^\circ\text{C}$
- Open-loop gain: 89 dB
- Phase margin:  $65^\circ$
- Gain bandwidth product: 100 kHz
- Input referred noise:  $73 \text{ nV}/\sqrt{\text{Hz}}$  @ 1 kHz



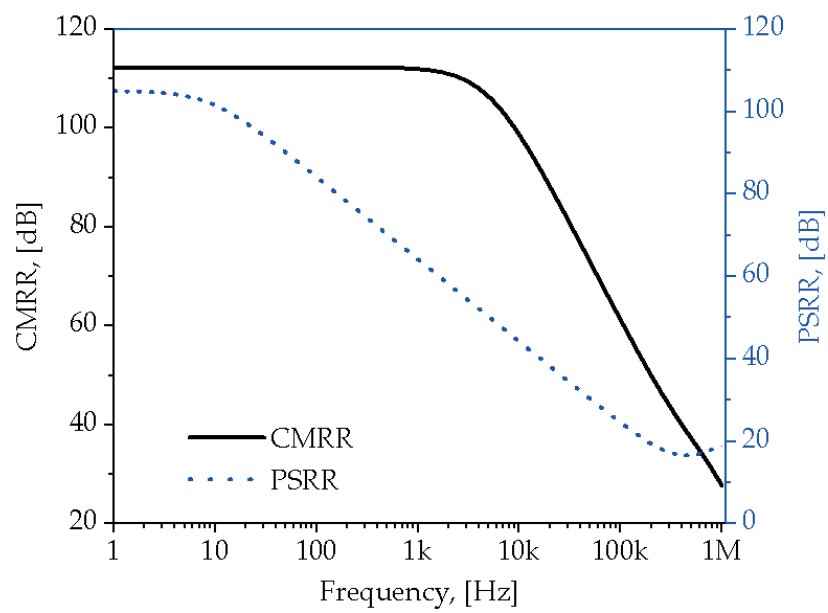
	W ( $\mu\text{m}$ )	L ( $\mu\text{m}$ )
M1, M2	100	2
M3, M4	50	5
M5	100	5
M6, M7	40	5
M8	140	5

(b)

Figure 5-9 Two stage operational amplifier. a) Schematic diagram. b) Design parameters of the circuit,  $C_M = 11 \text{ pF}$ .



(a)



(b)

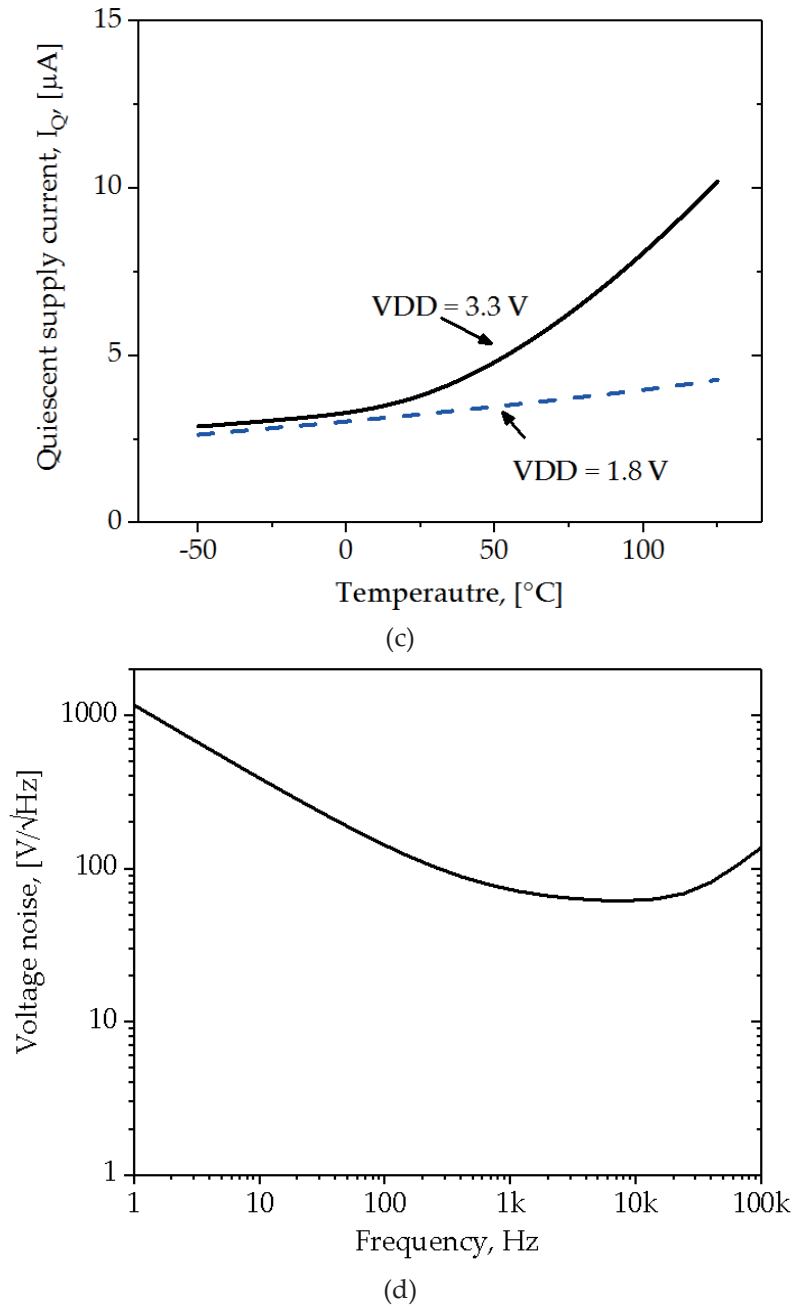
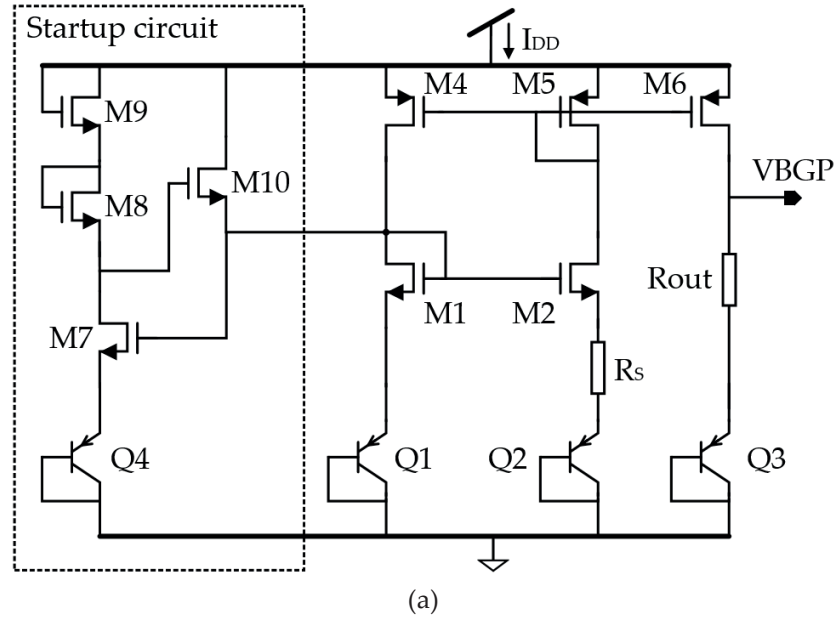


Figure 5-10 Simulation results for the key performances of OPA. a) Open-loop gain and phase margin. b) Common-mode rejection ratio (CMRR) and power supply rejection ratio (PSRR). c) Quiescent supply current varying with temperature at different supply voltages. d) Input referred voltage noise spectrum.

### 5.2.5 Bandgap reference (BGP)

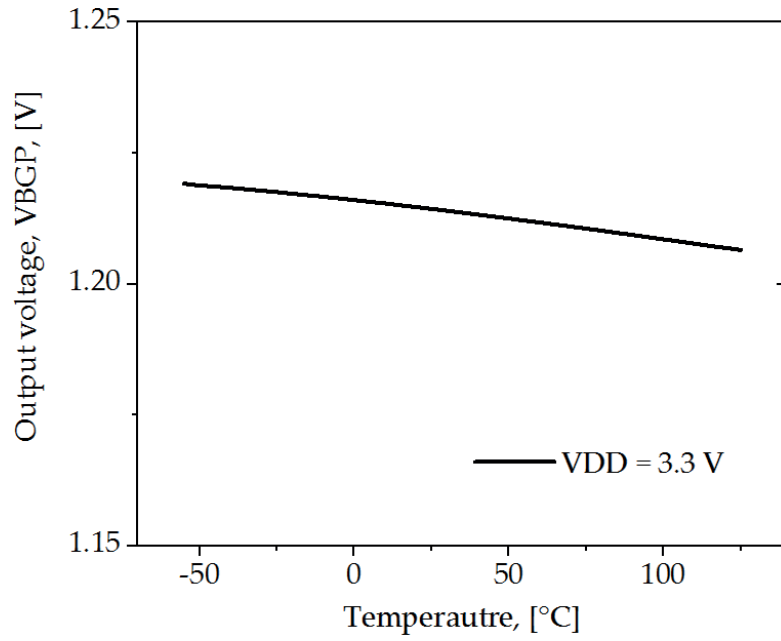
The BGP is designed with a schematic diagram as shown in Figure 5-11b. Similar to the Beta multiplier current source, the BGP circuit is consisted of a startup circuit that drives the circuit outside of the 'zero' state, and a voltage generating circuit. The voltage generating circuit adds up two voltages, *i.* diode voltage that is complementary to absolute temperature (CTAT); *ii.* a current that is proportional to absolute temperature (PTAT) multiplied by a resistor.



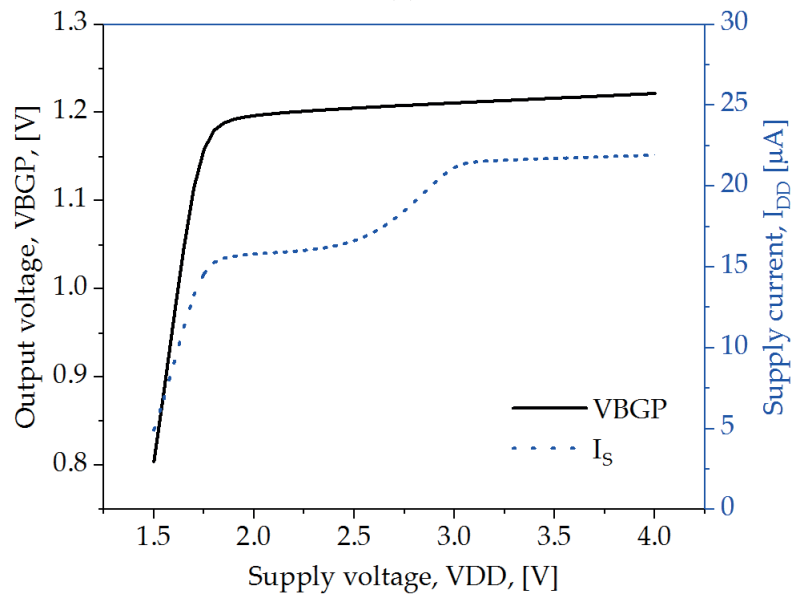
	W ( $\mu\text{m}$ )	L ( $\mu\text{m}$ )
M1, M2	40	5
M4-M6	40	5
M7	40	5
M8-M10	1	0.5
Q1, Q4	10	10
Q2, Q3	80	10

(b)

Figure 5-11 Bandgap reference. a) Schematic diagram. b) Design parameters.  $R_s = 10 \text{ k}\Omega$ ,  $R_{\text{out}} = 100 \text{ k}\Omega$ .



(a)



(b)

Figure 5-12 Simulation results for the BGP voltage source. a) Output voltage vs. temperature at  $V_{DD} = 3.3$  V. b) Output voltage and current consumption vs. supply voltage.

From section 5.2.3, we know that the current generated through a Beta multiplier is a PTAT current, which is why the circuit of the BGP looks similar to that of the Beta multiplier. Simulation results (Figure 5-12a) show that the temperature coefficient of the designed BGP is  $-57.8 \text{ ppm}/^{\circ}\text{C}$  when  $V_{DD} = 3.3 \text{ V}$ . The supply current  $I_{DD}$  is about  $22 \mu\text{A}$  when  $V_{DD} = 3.3 \text{ V}$ . The impact of supply voltage variation to the output voltage is determined by supply voltage sensitivity, and defined as  $\Delta V_{BGP}/\Delta V_{DD}$ . It is  $22.9 \text{ mV/V}$  calculating from  $V_{DD} = 1.8 \text{ V}$  to  $V_{DD} = 3.3 \text{ V}$ .

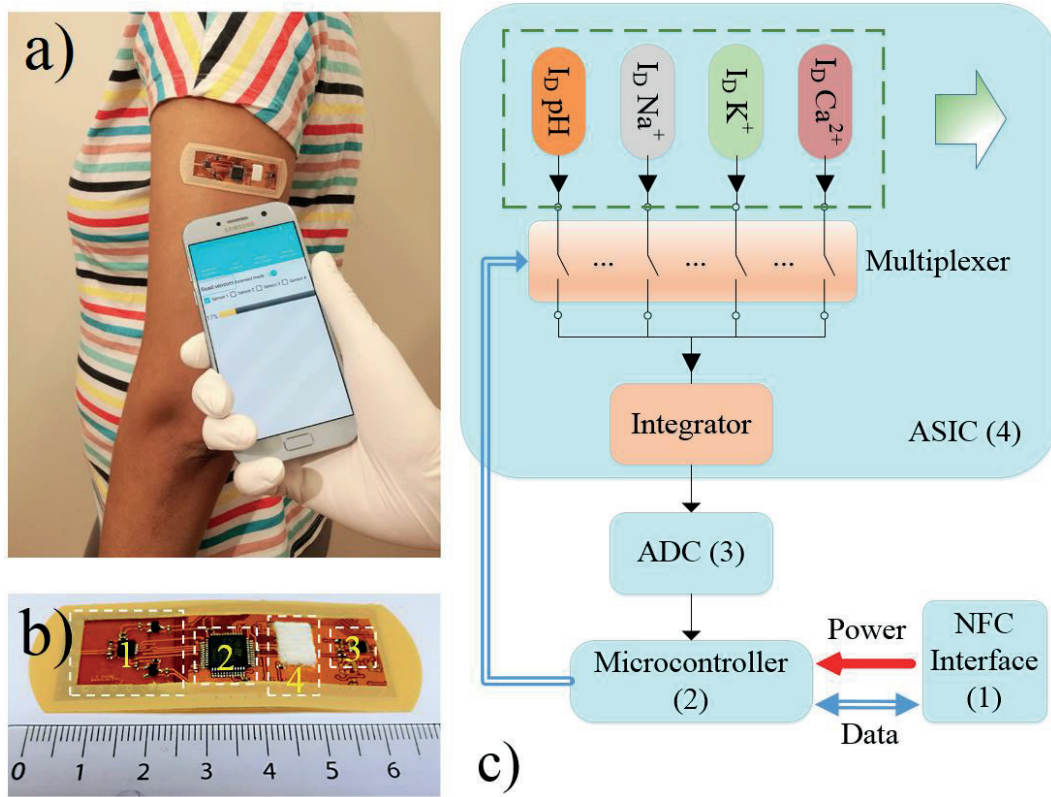


Figure 5-13 a) A photo of the wearable system. b) A photo of the top-side of the NFC tag. ASIC with 3D-EMG-ISFETs is bonded on the bottom side of the tag ('skin side'). A sweat outlet with cotton is attached and extended from the skin side to the front side of the tag through a hole in the tag. c) Corresponding block diagram of the NFC powered sensing tag.

### 5.2.6 Wearable sensor node implementation

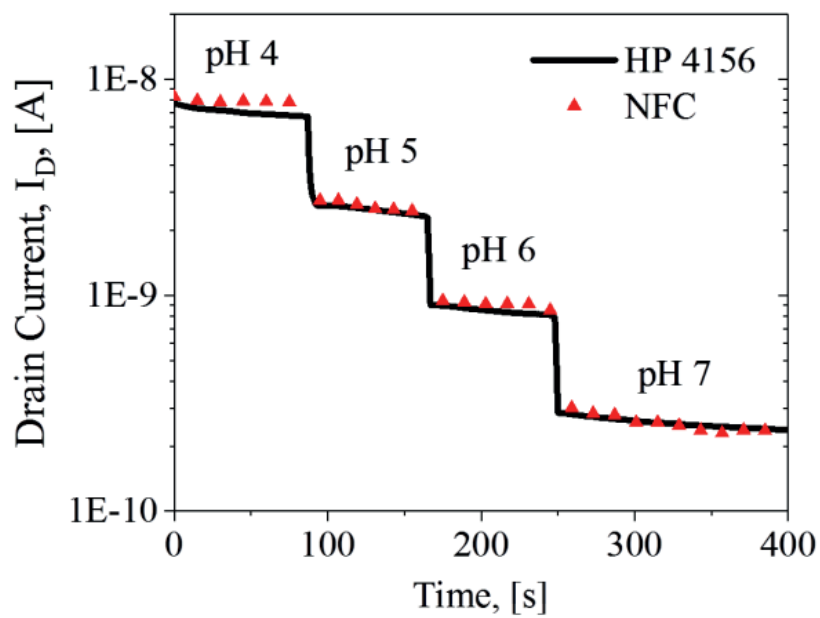
In this section, we present a wirelessly powered, flexible sensor tag (Figure 5-13a) that demonstrates the functionality of the current readout ASIC introduced in the previous sections. It reads the sensor signal from the 3D-EMG-ISFETs via multiplexing and communicates with a mobile terminal through Near Field Communication (NFC) protocol.

Shown in Figure 5-13c is a block diagram of the sensor tag in Figure 5-13b, which consists of (1) ASIC containing 3D-EMG-ISFETs, 16:1 multiplexer, and on-chip integrator. (2) Microcontroller. (3) 12-bit Analog to Digital Converter (ADC). (4) NFC interface chip, voltage regulators and antenna.

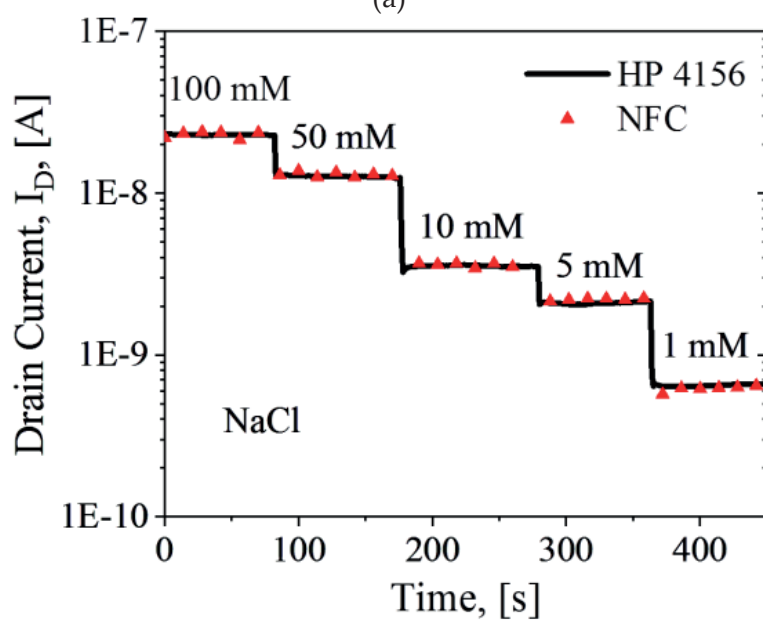
Once the sensor tag gets in proximity with the mobile terminal, it is powered on through NFC energy harvesting. A constant drain-source bias voltage is generated from the ASIC, and the Liquid Under Test (LUT) is biased by a commercial Ag/AgCl reference electrode (RE) (RE-Ag/AgCl from Micrux). The functionalized 3D-EMG-ISFET outputs a drain current ( $I_D$ ) which is proportional to the target ion's concentration.  $I_D$  is readout with an active integrator in the ASIC (Figure 5-3), in order to reject high frequency noise. The integrator reads the current signal into a voltage signal  $V_{out}$ .  $V_{out}$  is then converted by an ADC into digital signal and transmitted via NFC interface to a smart phone for data processing. From the mobile application,  $I_D$  is calculated with the aid of Equation 5.1.

Now we are able to record the drain current with the NFC platform and a dedicated android application. Dynamic responses of the 3D-EMG-pH sensor and 3D-EMG- $\text{Na}^+$  sensor have been recorded by the NFC application, in order to justify its wirelessly powered, multiplexed sensing capability. The 3D-EMG-ISFET for pH sensing, is sequentially immersed in drops of pH buffer. Time dependent measurement of the  $I_D$  is recorded both with a Precision Semiconductor Parameter Analyzer (HP 4156), and with the NFC platform. A good agreement is shown in Figure 5-14a. The same has been done with the 3D-EMG- $\text{Na}^+$  sensitive FET, and plotted in Figure 5-14b, demonstrating the NFC platform's accurate sensing capability.





(a)



(b)

Figure 5-14 Chronoamperometric readout of the pH sensing 3D-EMG-ISFET (a), and 3D-EMG- $\text{Na}^+$  sensitive FET (b), using NFC communication vs. with Precision semiconductor parameter analyzer (HP 4156).

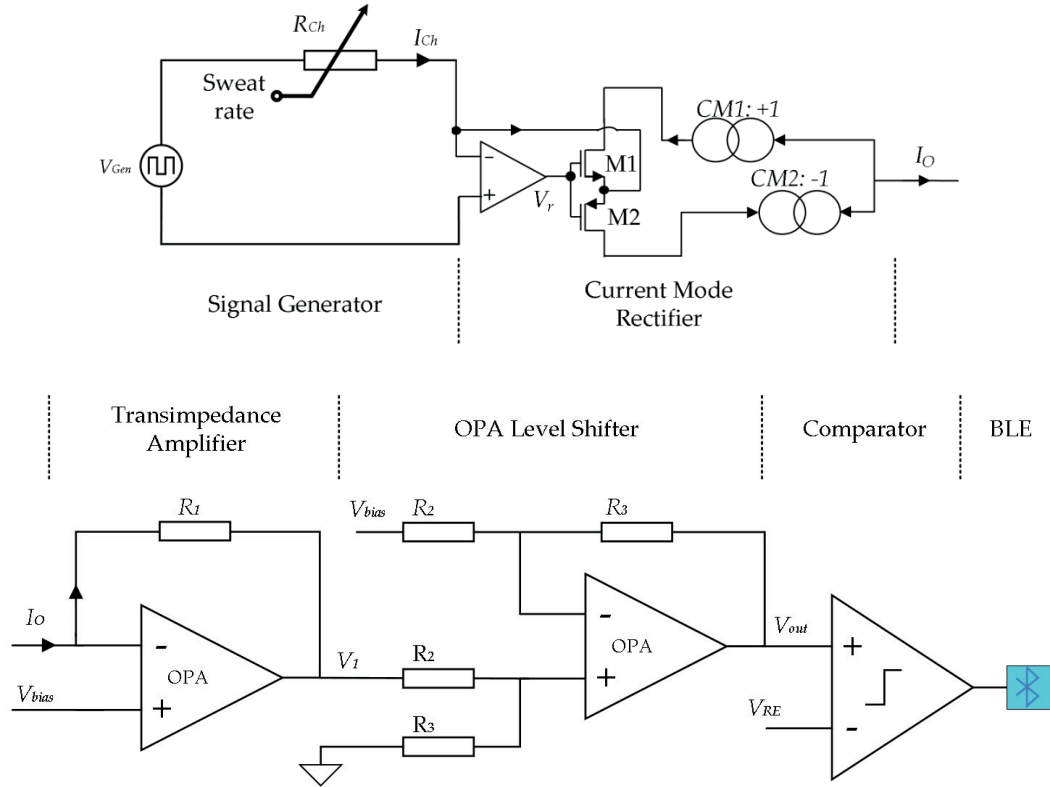


Figure 5-15 Readout circuit for channel impedance

### 5.3 Sweat-rate-to-frequency readout implementation

As introduced in Chapter 4, the microfluidic channel conductance is modulated by the sweat rate, into a pulsed signal. In this section, we are going to present the readout circuit dedicated to reading the channel conductance, providing the capability of streaming real-time changes in the channel conductance.

#### 5.3.1 Block design and analysis

Shown in Figure 5-15 is a block diagram of the readout circuit that converts the channel conductance into a voltage signal. It consists of a signal generator that generates an AC

voltage  $V_{Gen}$  with tunable frequency (from 1 kHz to 20 MHz) and amplitude of 0.5 Volts. The AC voltage is applied on the channel resistor ( $R_{Ch}$ ), to generate an output current ( $I_{Ch}$ ) that is proportional to the channel conductance ( $G_{Ch} = 1/R_{Ch}$ ).

AC voltage is applied here due to the fact that we will need to integrate the sweat rate readout in the same microfluidic channel as the biomarker sensors. With AC voltage at an appropriate frequency, it is possible minimize cumulative migration of ions on the biomarker sensing electrodes, and thereby minimize the double layer charge screening effects, which tends to mask the charges introduced by biomarkers during sensing.

$I_{Ch}$  is then passed through a current-mode rectifier, which rectifies the AC current  $I_{Ch}$  into a DC current  $I_O$ . This is needed for a single-supply powered system, in order to always keep the signal in the supply range.

In the current-mode rectifier, when  $I_{Ch}$  is positive<sup>2</sup>, it is directed through transistor M2 and current mirror 2 (CM2), leading to  $I_O = -I_{Ch}$ . When  $I_{Ch}$  is negative, it is directed through the other path, i.e., transistor M1 and current mirror 1 (CM1), resulting in  $I_O = I_{Ch}$ . Therefore,  $I_O = -|I_{Ch}|$  is a DC current flowing in the negative direction (opposite to the corresponding arrow of  $I_O$ ). After the current-mode rectifier,  $I_O$  is fed into a transimpedance amplifier, resulting in an intermediate voltage signal ( $V_1 = V_{bias} - R_1 * I_O$ ). In the next stage, an OPA level shifter is used to further amplify the signal, and nullify its common mode component. The output voltage is

Equation 5.3

$$V_{out} = -I_O * R_1 R_3 / R_2 = |I_{Ch}| * R_1 R_3 / R_2$$

Therefore,  $V_{out}$  is a positive voltage proportional to the amplitude of  $I_{Ch}$ .

Feeding  $V_{out}$  to the input of an ADC or a comparator results in direct digitization of the channel conductance signal into a pulse width modulated digital signal, whose frequency and duty cycle are related to the sweat rate in the fashion deducted and demonstrated in

---

<sup>2</sup> Polarity of current variables are marked in the schematic with arrows, a 'positive' current is when the current flows in the direction pointed by the corresponding arrow, and 'negative' current means the current flows in the opposite direction.

Chapter 4. Either ADC or comparator is used depending on the application, e.g., during experimental verification stage, it is necessary to use the ADC to record the accurate raw value of channel conductance, in order to post-process and extract more concrete features of the channel; whereas in wireless sensor node applications where power supply and data processing capabilities are limited, and the properties of channel conductance have been well defined through optimization, using a comparator will largely alleviate the CPU's load in calculation. Finally, the digital data stream is transmitted through Bluetooth Low Energy (BLE) communication to a mobile application, in order to continuously monitor the channel conductance.

### 5.3.2 Component selection and circuit implementation

The signal generator (Figure 5-16) is realized with two voltage dividers that generates  $V_L$  and  $(V_H = V_L + V_{Gen})$ , two ultra-low power OPAs (20  $\mu$ A/Amplifier, in a commercially available micropower quad-packaged operational amplifier OPA4336. The same OPA4336 is used for the other OPAs shown in Figure 5-15) connected in unity feedback mode in order to buffer the aforementioned voltages, four low leakage switches in a commercial quad SPST analog switch IC (MAX4751), and a low power (3 V, 0.4 mA) oscillator (LTC6900) that provides a single-supply, rail-to-rail, 50% duty cycle square wave output signal ( $CLK$ ). The  $CLK$  signal's frequency can be tuned from 1 kHz to 20 MHz via an external resistor. The  $CLK$  signal is then inverted with a commercial logic inverter IC (SN74LVC2G04) to generate two clock signals ( $\varphi$  and  $\bar{\varphi}$  with phase difference of 180°) to control the switches.

**The current-mode rectifier** is consisted of an input stage and an output stage. The input stage is a bi-directional current conveyor constructed by one OPA, one NMOS transistor and one PMOS transistor. The pair of transistors are from a commercial monolithic dual N-channel and dual P-channel complementary matched transistor pair ALD1105. The current mirrors in the output stage are consisted of basic current mirror pairs, also formed with the transistor pairs in an ALD1105 (shown in Figure 5-17).

**The ADC or comparator** is selected to be the integrated ADC/comparator from the selected BLE system on chip (SoC), nRF52832.

**The BLE SoC** is currently chosen to be carried in a commercially available development board (Bluetooth nRF52 Feather [132]).

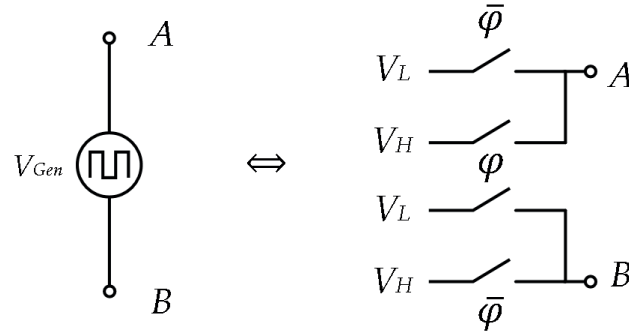


Figure 5-16 Signal generator schematic

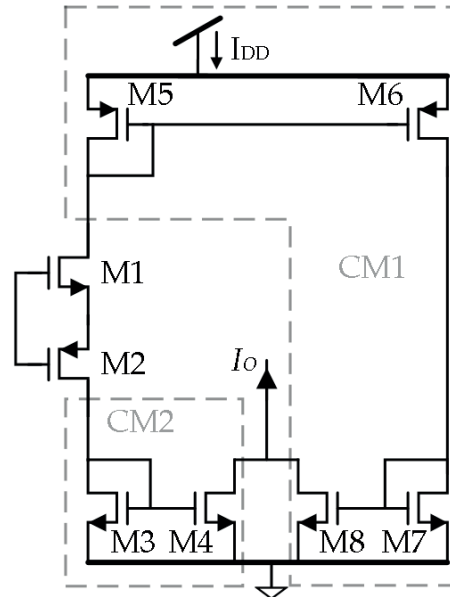


Figure 5-17 Current mirror schematic

### 5.3.3 Experimental validation and discussions

The entire circuit hasn't been tested yet, due to the fact that more works are undergoing to optimize the microfluidic channel's long-time performance. However, some of the

individual consisting blocks have been validated in our previous work. These include the signal generator and the current-mode rectifier. We are going to introduce the validation results obtained with them in this section. The experimental setup is shown in Figure 5-18, a commercial NMOS transistor (ALD1105) is connected as the device under test (DUT).

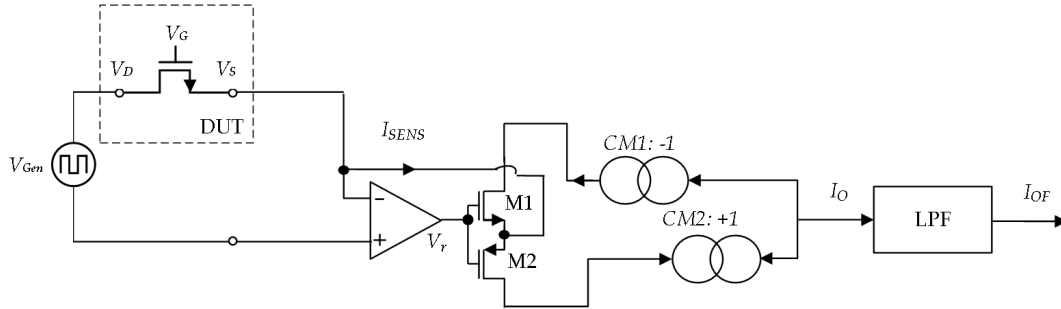


Figure 5-18 Experimental validation of the signal generator and current mode rectifier

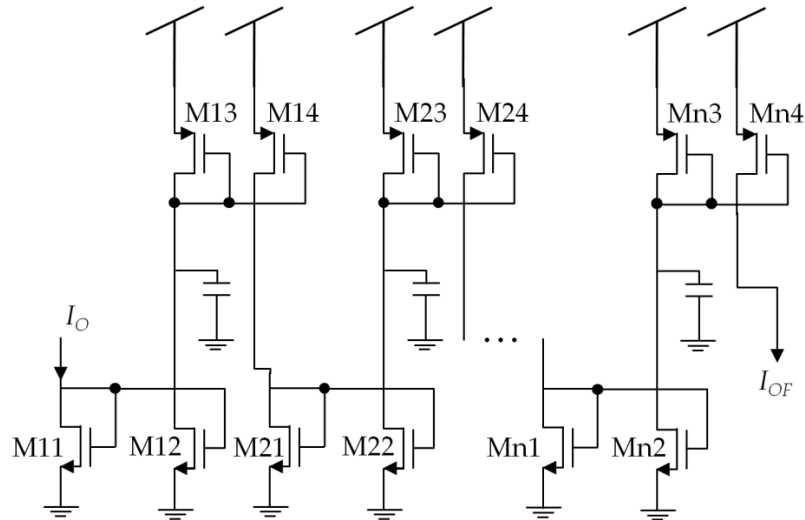
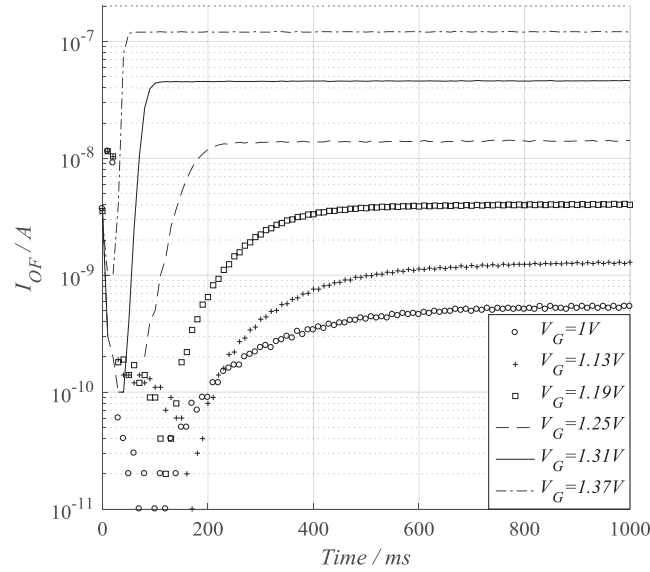
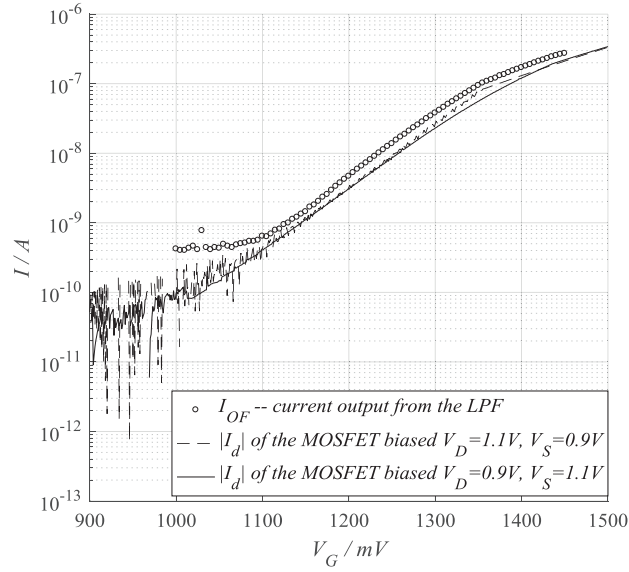


Figure 5-19 An 8th order current mode LPF,  $n = 4$ .



(a)



(b)

Figure 5-20 Measurement results from the experimental validation setup. a) Dynamic response of the output current  $I_{OF}$  under different gate bias conditions. b) Extracted  $I_{OF}$ - $V_G$  sweep compared with the  $I_D$ - $V_G$  characteristics of a standalone transistor.

Therefore, the DUT is considered a variable resistor controlled by the gate terminal voltage ( $V_G$ ) of the NMOS transistor. The signal generator, as detailed in Figure 5-16, generates alternating square wave voltages (Frequency = 77 Hz,  $V_H = 1.1$  V,  $V_L = 0.9$  V) to

bias the transistor's drain and source terminals. The 77 Hz CLK signal in this experiment was generated by the pulse generator unit (PGU) of a semiconductor parameter analyzer (HP4156). This results in an AC current ( $I_{\text{SENS}}$ ) flowing through the channel of the transistor into the current mode rectifier with a DC current output ( $I_o$ ). The current mode rectifier was realized with ALD1105 and OPA336, the same components as in the circuit introduced in Figure 5-15. After that,  $I_o$  is passed through an 8th-order current-mode low pass filter (LPF, shown in Figure 5-19), which is integrated in a dedicated ASIC designed with AMS 0.35  $\mu\text{m}$  technology. The output current  $I_{\text{OF}}$  is measured with HP 4156. As  $V_G$  is swept from  $V_G = 0.9 \text{ V}$  to  $V_G = 1.5 \text{ V}$ , we plotted  $I_{\text{OF}}$  versus time in Figure 5-20a.  $I_{\text{OF}}$  versus  $V_G$  is extracted from this plot, at time = 500 ms, and shown in Figure 5-20b as a 'circle' symbolled curve.

In comparison, we characterized the  $I_D$ - $V_G$  characteristics of the NMOS transistor individually, under two bias conditions (since the voltage generator was periodically switching the transistor between these two bias conditions): a.  $V_D = 1.1 \text{ V}$ ,  $V_S = 0.9 \text{ V}$ ; b.  $V_D = 0.9 \text{ V}$ ,  $V_S = 1.1 \text{ V}$ . The results are shown in Figure 5-20b as a dashed line and a straight line, respectively. Comparing the  $I_{\text{OF}}$  versus  $V_G$  results with the  $I_D$ - $V_G$  characteristics, we conclude that the combination of the signal generator, the current mode rectifier and the 8<sup>th</sup> order current mode LPF works accurately in biasing a transistor and outputs a current with tolerable error provided the large conductance variations in our application: microfluidic channel conductance measurement.

## 5.4 Conclusions

In this chapter, we designed readout circuits for the sensors involved in our sweat sensing system.

- ISFET sensors biased in transconductance readout mode.
- Sweat rate sensor conductance monitoring readout circuit.

We validated the ISFET readout circuit with a wearable patch, loaded with 3D-EMG-ISFET sensors to measure multiple ions through multiplexing. Both pH and  $\text{Ca}^{2+}$  have been measured. The results were compared with established instrument measurements, proving the wearable communication capability of our sensor patch. More developments



are undergoing to establish reliable signal fidelity characterizations such as signal to noise ratio degradation related to communication channel.

We developed readout circuit for real-time monitoring and streaming of channel conductance variations. Individual components of the readout circuit have been validated via experiments measuring conductance at the same level of channel conductance. In the near future, we will validate the whole setup with both ex-situ measurements and in-situ measurements of sweat rate.



## Chapter 6 Conclusions

---

Up till now, we have demonstrated the design, characterization and integration of all necessary building blocks for a wearable sweat sensing patch that is to be tested on human skin. This chapter will draw some conclusions as well as provide outlook for possible follow ups in both research and industry. The first part of this chapter summarizes the main contributions of this thesis and future work to be continued regarding the scope of this thesis. The second part is an outlook of what is remaining to be of high research interest and industrialization obstacles, in the field of wearable sweat sensors.

## 6.1 Main contributions

The main contributions of this thesis are summarized in this section.

### 6.1.1 High performance, CMOS BEOL integrated 3D-EMG-ISFET sensors

We developed a series of post-processing methods to be introduced to the back-end-of-line (BEOL) of a standard CMOS process, and achieved 3D-EMG-pH sensors with state of the art figure of merits as summarized below:

- Near-Nernstian limit sensitivity: 56 mV/pH.
- Ultra-low device-to-device threshold variation:  $\pm 28$  mV.
- Minimum reported power consumption: 2 pW/sensor.
- Low drift rate: 0.7 mV/hour.
- High robustness, low cost, up-scalability for industrialization.

As introduced in Chapter 3, neither CMOS ISFET nor near-Nernstian sensitivity is new from scientific point of view. However, we combined the virtues of both, made the scientific and technological breakthroughs in terms of high performance, high predictability and low cost. Device to device variation, which has been a big issue in ISFET sensors research, is eliminated through our novel post-process steps. The off-state current of our devices are low, which ensures the ultra-low power consumption when the 3D-EMG-ISFETs are biased in deep sub-threshold region. These breakthroughs will greatly benefit the ISFET research as well as sensor industry.

Through BEOL functionalization, we were able to integrate multiple ion sensors by functionalizing the 3D-EMG-ISFET with ion selective membranes (ISMs) on a single die, the resulting 3D-EMG-(Na<sup>+</sup>/K<sup>+</sup>/Ca<sup>2+</sup>) sensors featuring:

- High sensitivity, 57 mV/dec[Na<sup>+</sup>], 48 mV/dec[K<sup>+</sup>], 26 mV/dec[Ca<sup>2+</sup>].
- High selectivity against interfering ions, cross sensitivity < 9 mV per decade of interfering ion concentration.
- Simultaneous recording multiple ions' concentrations in the same liquid under test.
- Fast response time of less than 5 seconds.

BEOL post-processing and functionalization of standard CMOS chips is a key feature of our work. It opens the possibility of adopting different surface modification methods which not necessarily have to be CMOS process compatible. For example, heterogeneous integration [133], [134] could be envisioned to improve the limit of detection of 3D-EMG-ISFET sensors, thanks to the BEOL post-processing capability.

### 6.1.2 Experimental verification of sensor performance with unspiked sweat samples

Dedicated experiments were carried out to test the 3D-EMG-ISFETs' capability of making correct interpretations of ion concentrations in real sweat. Sweat samples were tested with three sensors in order to prove the measurement reproducibility, and the results are listed below. Given the large physiological variation range of ion concentrations in healthy individuals, the accuracy achieved by the sensors is acceptable for practical applications.

3D-EMG-pH sensors:

- Standard deviation to average ratio: 2.3%
- Maximum deviation from commercial ISEs: 2.8%

3D-EMG-Na<sup>+</sup> sensors:

- Standard deviation to average ratio: 9.3%
- Maximum deviation from commercial ISEs: 12%

### 6.1.3 First demonstration of long term, continuous, electronic monitoring of low sweat rate

We integrated the ISFET sensor chip with bio-compatible skin interface (microfluidics) with drop-to-drop resolution. The microfluidics is capable of sampling and analyzing sweat drops with volume as low as tens of nano-Liters. The microfluidic channel features are listed below.

- Ultra-low dead volume: < 100 nL
- Fast adsorption of droplets < 1 s.
- Passive pumping and draining of droplets.

Based on the drop-to-drop periodic characteristics of channel conductance, we developed the first, to the best of our knowledge, intuitive electronic methods for long term reading the sweat rate, i.e. the Sweat-Rate-to-Frequency-Modulation (SRFM) method and Sweat-Rate-to-Duty-Cycle (SRDC) method. Experiments were carried out with single pore 'sweating' artificial skin, and proved the validity of our theoretical analysis.

#### 6.1.4 Integration and test of wearable, wirelessly powered sweat sensing patch

This thesis developed high performance individual components required for a wearable sweat sensor. It also integrated the components on a bio-compatible substrate, together with experimentally validated readout circuits, in order to complete the system to be a function-ready sweat sensing patch.

### 6.2 Outlook

Following the main contributions of this thesis, the author is aware that there are still several research and technological advancements that need to be performed in the future. All of them are of great interest in both research and industry concerning wearable sweat sensing.

#### 6.2.1 Reliability of miniaturized ISMs

The research into ISMs [54], [135]–[138] has been one of the most mature parts of the solid state potentiometric sensors. Although researches have covered from sensitivity, selectivity control, chemical leaching [52], [54], water penetration [55], [56], to short term / long term drift [114], [139] and lifetime studies [53], not much effort has been put into the study of reliable miniaturization. Up to now, most of the solid state ISEs are developed by dropcasting [66], [122], which results in large sized ( $> 1$  mm diameter, and  $> 100$   $\mu\text{m}$  thickness) and no-process-controlled ISMs. In some other researches, inkjet print is adopted in order to enhance the reproducibility [140], [141], however, miniaturization has not been their concern. Nonetheless, the miniaturization of single electrodes is of key importance in current technological advancements of sweat sensor development. The

community shares a common sense that in future sweat sensors, multiple ISEs should be co-integrated in a wearable patch to simultaneously monitor target biomarkers. And this could not be realized without reliably miniaturizing the ISMs.

Therefore, this is one field of interest for the useful applications promised by sweat sensors. And it is one of the short term goals in our 3D-EMG-ISFET development. We will try to achieve the following:

- Research into ISMs suitable for inkjet printing.
- Print ISMs with small footprint ( $< 150\ \mu\text{m}$  diameter and  $\sim 10\ \mu\text{m}$  thickness). The diameter of ISMs is the main limitation for integration of solid state ISEs and ISFETs, while the thickness determines the depth of microfluidic channels, which in turn defines the dead volume of this sensor.
- Repeatability and stability enhancement. Silylation [142] will help form covalent bond between the ISM and the sensor surface. This in turn enhances the physical stability of an ISM.

### 6.2.2 Sensing uncharged or weakly charged biomarkers

As summarized in Chapter 2, potentiometric sensing method is the easiest to implement compared to other electrochemical methods, however, they are limited in many use cases. Given the limited types of biomarkers (mainly electrolytes) that potentiometric sensors can sense with high precision, the pursuit of developing potentiometric sensors for other types of biomarkers has never been ceased. Those biomarkers include molecules which are electrically neutral or weakly charged, or molecules whose charges are strongly filtered by the electrical double layer. Molecularly imprinted polymer (MIP) membrane has been introduced to indirectly sense a weakly charged molecule, cortisol, in [47]. Antibody embedded polymer [143] is a viable solution to overcome the Debye length limit by bringing the charge closer to the conductive polymer interface.

### 6.2.3 Microfluidics with long term sweat transporting capability

In Chapter 4, we integrated the ISFET sensor chip with bio-compatible skin interface (microfluidics), and demonstrated drop-by-drop sweat transportation via both optical and electronic methods. The drop-by-drop sweat transportation is due to the high

hydrophilicity of the channel surface, which was made of SU-8 and activated by oxygen plasma. However, as discussed in Chapter 4, the hydrophilicity of the activated SU-8 surface gets degraded within a few hours when it is continuously transporting droplets of artificial sweat. There are several possible ways of fabricating very hydrophilic microfluidic channels:

- Paper microfluidics or wicking fibers. The hydrophilicity of paper and wicking fibers is very stable. However, they are prone to non-specific absorption of analytes into the cellulose itself. Analyte exchanges into and out of the cellulose causes confounding of fresh sweat samples with historic residues [144], [145].
- Processing of glass wafers is a promising way to fabricate microfluidics with ultra-low volume, through lithography and etching processes. The ultra-low dead volume made it possible that historic confounding not a problem anymore. However, it is problematic when we need to monolithically integrate the glass microfluidics with our ISFET sensor chip fabricated in CMOS processes.
- Processing of SU-8 is what we have adopted so far for the microfluidics. It provides the same advantages as provided by glass wafer fabrication, and adds on top of that the capability to be structured directly on CMOS chips/wafers, resulting in monolithic integration of microfluidic sensing chips. However, it has shown the weakness in preserving hydrophilicity.
- Surface functionalization of the microfluidic surface. [129] has reported an approach to enhance the hydrophilicity robustness. The authors covered the microfluidics surface with gold and functionalized it with peptide in order to achieve a robust and bio-compatible hydrophilic surface. Hydrophilicity was stable even after weeks of exposure to air. However, there was no report about the hydrophilicity stability during or after continuous usage (i.e., during or after transporting of liquid). Other kinds of functionalization can also be anticipated, e.g. polymer brushes engineered through surface-initiated polymerization [146] can be applied to saturate the microfluidic surface with hydroxyl groups and hence enhancing the hydrophilicity.

Therefore, future work will need to improve the microfluidic channel's long term hydrophilicity via research into proper functionalization.



### 6.2.4 Continuous streaming and processing of physiological data

Conventional bio-fluid tests are testing biomarker compositions only at discrete time slots. Whereas the wearable sweat sensors offer the opportunity of continuously monitoring the variations of biomarkers in a non-invasive manner. The difference between the two is analogous to that between snapshots and video streams. The information delivered by the latter is orders of magnitude higher than that delivered by the former.

- Now that we got the streamed bio-data, next step should be developments in interpreting them correctly, with the state of the art developments in data parsing technologies and processing algorithms.
- The progress in medical researches concerning the relevance of sweat chemical compositions to individual's health status can be benefited from the advancements in wearable sensors.
- In return from the progress in medical field, machine learning methods can be implemented in the data analysis, in order to provide more insight into health status and bring a bright future to the 'magic' predictive health monitoring [3], [11].

## 6.3 Concluding remarks

According to the main contributions summarized in section 6.1, it is time to conclude that we have reported the integration of all the needed functions in a wearable patch that is tested on humans.

The sensors are high performance, and their fabrication process is up-scalable with great industrialization interest.

The ultra-hydrophilic microfluidic channel together with the exploration of its drop-by-drop resolution sensing sweat rate, demonstrated the first long term continuous sweat-rate monitoring of its kind.

The integrated readout circuit design and experimental verifications paved the way to a fully functional wearable sweat sensing patch demonstrator, which will be of great help in future work concerning data collection and processing.



## References

- [1] B. M. Scirica, "Use of Biomarkers in Predicting the Onset, Monitoring the Progression, and Risk Stratification for Patients with Type 2 Diabetes Mellitus," *Clin. Chem.*, vol. 63, no. 1, pp. 186–195, Jan. 2017.
- [2] P. J. Mazzone *et al.*, "Evaluating Molecular Biomarkers for the Early Detection of Lung Cancer: When Is a Biomarker Ready for Clinical Use? An Official American Thoracic Society Policy Statement," *Am. J. Respir. Crit. Care Med.*, vol. 196, no. 7, pp. e15–e29, 01 2017.
- [3] V. R. Varma *et al.*, "Brain and blood metabolite signatures of pathology and progression in Alzheimer disease: A targeted metabolomics study," *PLoS Med.*, vol. 15, no. 1, p. e1002482, 2018.
- [4] R. Birtwhistle, N. R. Bell, B. D. Thombs, R. Grad, and J. A. Dickinson, "Periodic preventive health visits: a more appropriate approach to delivering preventive services," *Can. Fam. Physician*, vol. 63, no. 11, pp. 824–826, Nov. 2017.
- [5] L. E. Boulware *et al.*, "Systematic review: the value of the periodic health evaluation," *Ann. Intern. Med.*, vol. 146, no. 4, pp. 289–300, Feb. 2007.
- [6] L. T. Krogsbøll, K. J. Jørgensen, C. Grønhøj Larsen, and P. C. Gøtzsche, "General health checks in adults for reducing morbidity and mortality from disease: Cochrane systematic review and meta-analysis," *The BMJ*, vol. 345, Nov. 2012.
- [7] A. Mehrotra and A. Prochazka, "Improving Value in Health Care--Against the Annual Physical," *N. Engl. J. Med.*, vol. 373, no. 16, pp. 1485–1487, Oct. 2015.
- [8] K. M. Chacko and R. J. Anderson, "The annual physical examination: important or time to abandon?," *Am. J. Med.*, vol. 120, no. 7, pp. 581–583, Jul. 2007.
- [9] A. H. Goroll, "Toward Trusting Therapeutic Relationships — In Favor of the Annual Physical," *N. Engl. J. Med.*, vol. 373, no. 16, pp. 1487–1489, Oct. 2015.
- [10] D. U. Himmelstein and R. S. Phillips, "Should We Abandon Routine Visits? There Is Little Evidence for or Against," *Ann. Intern. Med.*, vol. 164, no. 7, p. 498, Apr. 2016.
- [11] "Digital Health: Tracking Physiomes and Activity Using Wearable Biosensors Reveals Useful Health-Related Information." [Online]. Available: <https://journals.plos.org/plosbiology/article?id=10.1371/journal.pbio.2001402>. [Accessed: 26-Jan-2019].

- 
- [12] M. Venugopal, S. K. Arya, G. Chornokur, and S. Bhansali, "A Realtime and Continuous Assessment of Cortisol in ISF Using Electrochemical Impedance Spectroscopy," *Sens. Actuators Phys.*, vol. 172, no. 1, pp. 154–160, Dec. 2011.
- [13] J. Kim *et al.*, "Simultaneous Monitoring of Sweat and Interstitial Fluid Using a Single Wearable Biosensor Platform," *Adv. Sci.*, vol. 5, no. 10, p. 1800880, 2018.
- [14] A. Kaushik, A. Vasudev, S. K. Arya, S. K. Pasha, and S. Bhansali, "Recent advances in cortisol sensing technologies for point-of-care application," *Biosens. Bioelectron.*, vol. 53, pp. 499–512, Mar. 2014.
- [15] W. Dang, L. Manjakkal, W. T. Navaraj, L. Lorenzelli, V. Vinciguerra, and R. Dahiya, "Stretchable wireless system for sweat pH monitoring," *Biosens. Bioelectron.*, vol. 107, pp. 192–202, Jun. 2018.
- [16] M. G. Bulmer and G. D. Forwell, "The concentration of sodium in thermal sweat," *J. Physiol.*, vol. 132, no. 1, pp. 115–122, Apr. 1956.
- [17] J. R. Stofan, J. J. Zachwieja, C. A. Horswill, R. Murray, S. A. Anderson, and E. R. Eichner, "Sweat and Sodium Losses in NCAA Football Players: A Precursor to Heat Cramps?," *Int. J. Sport Nutr. Exerc. Metab.*, vol. 15, no. 6, pp. 641–652, Dec. 2005.
- [18] M. J. Patterson, S. D. R. Galloway, and M. A. Nimmo, "Variations in Regional Sweat Composition in Normal Human Males," *Exp. Physiol.*, vol. 85, no. 6, pp. 869–875, 2000.
- [19] Z. Sonner *et al.*, "The microfluidics of the eccrine sweat gland, including biomarker partitioning, transport, and biosensing implications," *Biomicrofluidics*, vol. 9, no. 3, p. 031301, May 2015.
- [20] M. Bariya, H. Y. Y. Nyein, and A. Javey, "Wearable sweat sensors," *Nat. Electron.*, vol. 1, no. 3, p. 160, Mar. 2018.
- [21] W. G. Robertson and R. W. Marshall, "Ionized calcium in body fluids," *Crit. Rev. Clin. Lab. Sci.*, vol. 15, no. 2, pp. 85–125, 1981.
- [22] J. Stahl, "Studies of the Blood Ammonia in Liver Disease: Its Diagnostic, Prognostic, and Therapeutic Significance," *Ann. Intern. Med.*, vol. 58, no. 1, p. 1, Jan. 1963.
- [23] S. E. Browne, "Magnesium and Cardiovascular Disease," *Br. Med. J.*, vol. 2, no. 5349, p. 118, Jul. 1963.
- [24] T. D. Chinevere, R. W. Kenefick, S. N. Cheuvront, H. C. Lukaski, and M. N. Sawka, "Effect of Heat Acclimation on Sweat Minerals," ARMY RESEARCH INST OF ENVIRONMENTAL MEDICINE NATICK MA THERMAL AND MOUNTAIN MEDICINE DIVISION, Dec. 2007.

- 
- [25] M. J. Laires, C. P. Monteiro, and M. Bicho, "Role of cellular magnesium in health and human disease," *Front. Biosci. J. Virtual Libr.*, vol. 9, pp. 262–276, Jan. 2004.
- [26] P. J. Derbyshire, H. Barr, F. Davis, and S. P. J. Higson, "Lactate in human sweat: a critical review of research to the present day," *J. Physiol. Sci. JPS*, vol. 62, no. 6, pp. 429–440, Nov. 2012.
- [27] J. Moyer, D. Wilson, I. Finkelshtein, B. Wong, and R. Potts, "Correlation between sweat glucose and blood glucose in subjects with diabetes," *Diabetes Technol. Ther.*, vol. 14, no. 5, pp. 398–402, May 2012.
- [28] T. Umeda, R. Hiramatsu, T. Iwaoka, T. Shimada, F. Miura, and T. Sato, "Use of saliva for monitoring unbound free cortisol levels in serum," *Clin. Chim. Acta Int. J. Clin. Chem.*, vol. 110, no. 2–3, pp. 245–253, Mar. 1981.
- [29] D. Pieragostino, M. D'Alessandro, M. di Ioia, C. Di Ilio, P. Sacchetta, and P. Del Boccio, "Unraveling the molecular repertoire of tears as a source of biomarkers: beyond ocular diseases," *Proteomics Clin. Appl.*, vol. 9, no. 1–2, pp. 169–186, Feb. 2015.
- [30] J. Heikenfeld *et al.*, "Wearable sensors: modalities, challenges, and prospects," *Lab. Chip*, vol. 18, no. 2, pp. 217–248, Jan. 2018.
- [31] "Update on our Smart Lens program with Alcon," *Verily Blog*. .
- [32] A. Mena-Bravo and M. D. Luque de Castro, "Sweat: a sample with limited present applications and promising future in metabolomics," *J. Pharm. Biomed. Anal.*, vol. 90, pp. 139–147, Mar. 2014.
- [33] E. Russell, G. Koren, M. Rieder, and S. H. M. Van Uum, "The detection of cortisol in human sweat: implications for measurement of cortisol in hair," *Ther. Drug Monit.*, vol. 36, no. 1, pp. 30–34, Feb. 2014.
- [34] L. B. Baker, "Sweating Rate and Sweat Sodium Concentration in Athletes: A Review of Methodology and Intra/Interindividual Variability," *Sports Med. Auckl. NZ*, vol. 47, no. Suppl 1, pp. 111–128, Mar. 2017.
- [35] J. Heikenfeld, "Non-invasive Analyte Access and Sensing through Eccrine Sweat: Challenges and Outlook circa 2016," *Electroanalysis*, vol. 28, no. 6, pp. 1242–1249, 2016.
- [36] S. Robinson and A. H. Robinson, "Chemical composition of sweat," *Physiol. Rev.*, vol. 34, no. 2, pp. 202–220, Apr. 1954.

- 
- [37] V. Oncescu, D. O'Dell, and D. Erickson, "Smartphone based health accessory for colorimetric detection of biomarkers in sweat and saliva," *Lab. Chip*, vol. 13, no. 16, pp. 3232–3238, 2013.
- [38] D. B. Dill, F. G. Hall, and H. T. Edwards, "Changes in composition of sweat during acclimatization to heat," *Am. J. Physiol.-Leg. Content*, vol. 123, no. 2, pp. 412–419, Jul. 1938.
- [39] F. Sargent, C. R. Smith, and D. L. Batterton, "Eccrine sweat gland activity in heat acclimation," *Int. J. Biometeorol.*, vol. 9, no. 3, pp. 229–231, Oct. 1965.
- [40] J. D. Périard, S. Racinais, and M. N. Sawka, "Adaptations and mechanisms of human heat acclimation: Applications for competitive athletes and sports," *Scand. J. Med. Sci. Sports*, vol. 25 Suppl 1, pp. 20–38, Jun. 2015.
- [41] J. Heikenfeld, "Bioanalytical devices: Technological leap for sweat sensing," *Nature*, vol. 529, no. 7587, pp. 475–476, Jan. 2016.
- [42] M. A. Huestis, E. J. Cone, C. J. Wong, A. Umbricht, and K. L. Preston, "Monitoring Opiate Use in Substance Abuse Treatment Patients With Sweat and Urine Drug Testing," *J. Anal. Toxicol.*, vol. 24, no. 7, pp. 509–521, Oct. 2000.
- [43] A. Luchini *et al.*, "Nanoparticle technology: addressing the fundamental roadblocks to protein biomarker discovery," *Curr. Mol. Med.*, vol. 10, no. 2, pp. 133–141, Mar. 2010.
- [44] D. P. Rose *et al.*, "Adhesive RFID Sensor Patch for Monitoring of Sweat Electrolytes," *IEEE Trans. Biomed. Eng.*, vol. 62, no. 6, pp. 1457–1465, Jun. 2015.
- [45] S. Anastasova *et al.*, "A wearable multisensing patch for continuous sweat monitoring," *Biosens. Bioelectron.*, vol. 93, pp. 139–145, Jul. 2017.
- [46] H. Y. Y. Nyein *et al.*, "A Wearable Electrochemical Platform for Noninvasive Simultaneous Monitoring of Ca<sup>2+</sup> and pH," *ACS Nano*, vol. 10, no. 7, pp. 7216–7224, Jul. 2016.
- [47] O. Parlak, S. T. Keene, A. Marais, V. F. Curto, and A. Salleo, "Molecularly selective nanoporous membrane-based wearable organic electrochemical device for noninvasive cortisol sensing," *Sci. Adv.*, vol. 4, no. 7, p. eaar2904, Jul. 2018.
- [48] W. Gao *et al.*, "Fully integrated wearable sensor arrays for multiplexed *in situ* perspiration analysis," *Nature*, vol. 529, no. 7587, pp. 509–514, Jan. 2016.
- [49] A. Martín *et al.*, "Epidermal Microfluidic Electrochemical Detection System: Enhanced Sweat Sampling and Metabolite Detection," *ACS Sens.*, vol. 2, no. 12, pp. 1860–1868, Dec. 2017.

- 
- [50] D. Kinnamon, R. Ghanta, K.-C. Lin, S. Muthukumar, and S. Prasad, "Portable biosensor for monitoring cortisol in low-volume perspired human sweat," *Sci. Rep.*, vol. 7, Oct. 2017.
- [51] A. J. Bandodkar *et al.*, "Battery-free, skin-interfaced microfluidic/electronic systems for simultaneous electrochemical, colorimetric, and volumetric analysis of sweat," *Sci. Adv.*, vol. 5, no. 1, p. eaav3294, Jan. 2019.
- [52] E. Bakker and E. Pretsch, "Lipophilicity of tetraphenylborate derivatives as anionic sites in neutral carrier-based solvent polymeric membranes and lifetime of corresponding ion-selective electrochemical and optical sensors," *Anal. Chim. Acta*, vol. 309, no. 1, pp. 7–17, Jun. 1995.
- [53] Oliver. Dinten *et al.*, "Lifetime of neutral-carrier-based liquid membranes in aqueous samples and blood and the lipophilicity of membrane components," *Anal. Chem.*, vol. 63, no. 6, pp. 596–603, Mar. 1991.
- [54] P. Gehrig, B. Rusterholz, and W. Simon, "Very lipophilic sodium-selective ionophore for chemical sensors of high lifetime," *Anal. Chim. Acta*, vol. 233, pp. 295–298, Jan. 1990.
- [55] Xizhong. Li and D. Jed. Harrison, "Measurement of concentration profiles inside a nitrite ion-selective electrode membrane," *Anal. Chem.*, vol. 63, no. 19, pp. 2168–2174, Oct. 1991.
- [56] J. Janata, "Historical review. Twenty years of ion-selective field-effect transistors," *Analyst*, vol. 119, no. 11, pp. 2275–2278, Jan. 1994.
- [57] B. J. Polk, A. Stelzenmuller, G. Mijares, W. MacCrehan, and M. Gaitan, "Ag/AgCl microelectrodes with improved stability for microfluidics," *Sens. Actuators B Chem.*, vol. 114, no. 1, pp. 239–247, Mar. 2006.
- [58] H. Suzuki, T. Hirakawa, S. Sasaki, and I. Karube, "Micromachined liquid-junction Ag/AgCl reference electrode," *Sens. Actuators B Chem.*, vol. 46, no. 2, pp. 146–154, Feb. 1998.
- [59] J. Ghilane, P. Hapiot, and A. J. Bard, "Metal/Polypyrrole Quasi-Reference Electrode for Voltammetry in Nonaqueous and Aqueous Solutions," *Anal. Chem.*, vol. 78, no. 19, pp. 6868–6872, Oct. 2006.
- [60] G. Gritzner, "Reference Redox Systems in Nonaqueous Systems and the Relation of Electrode Potentials in Nonaqueous and Mixed Solvents to Standard Potentials in Water," in *Handbook of Reference Electrodes*, G. Inzelt, A. Lewenstam, and F. Scholz, Eds. Berlin, Heidelberg: Springer Berlin Heidelberg, 2013, pp. 25–31.

- [61] T. Guinovart, G. A. Crespo, F. X. Rius, and F. J. Andrade, "A reference electrode based on polyvinyl butyral (PVB) polymer for decentralized chemical measurements," *Anal. Chim. Acta*, vol. 821, pp. 72–80, Apr. 2014.
- [62] E. Garcia-Cordero *et al.*, "Three-Dimensional Integrated Ultra-Low-Volume Passive Microfluidics with Ion-Sensitive Field-Effect Transistors for Multiparameter Wearable Sweat Analyzers," *ACS Nano*, vol. 12, no. 12, pp. 12646–12656, Dec. 2018.
- [63] P. Clement, "Optimization of a microfluidic interface for sweat collection on the skin," *EPFL Master Thesis*, 2019.
- [64] "11.3: Coulometric Methods," *Chemistry LibreTexts*, 25-Oct-2013. [Online]. Available: [https://chem.libretexts.org/Bookshelves/Analytical\\_Chemistry/Book%3A\\_Analytical\\_Chemistry\\_2.0\\_\(Harvey\)/11\\_Electrochemical\\_Methods/11.3%3A\\_Coulometric\\_Methods](https://chem.libretexts.org/Bookshelves/Analytical_Chemistry/Book%3A_Analytical_Chemistry_2.0_(Harvey)/11_Electrochemical_Methods/11.3%3A_Coulometric_Methods). [Accessed: 24-Jul-2019].
- [65] "Metrohm Autolab." [Online]. Available: <https://www.metrohm-autolab.com/>. [Accessed: 07-May-2019].
- [66] H. Y. Y. Nyein *et al.*, "A Wearable Microfluidic Sensing Patch for Dynamic Sweat Secretion Analysis," *ACS Sens.*, vol. 3, no. 5, pp. 944–952, May 2018.
- [67] A. Alizadeh *et al.*, "A wearable patch for continuous monitoring of sweat electrolytes during exertion," *Lab. Chip*, vol. 18, no. 17, pp. 2632–2641, Aug. 2018.
- [68] J. T. Stock, M. V. Orna, A. C. S. D. of the H. of Chemistry, A. C. S. D. of A. Chemistry, Ont. ) American Chemical Society. Meeting Toronto, and Ont. ) Chemical Congress of North America (3rd : 1988 : Toronto, *Electrochemistry, past and present*. Washington, DC : American Chemical Society, 1989.
- [69] J. T. Stock, "A Backward Look at Scientific Instrumentation," *Anal. Chem.*, vol. 65, no. 7, pp. 344A–351A, Apr. 1993.
- [70] "11.2: Potentiometric Methods - Chemistry LibreTexts." [Online]. Available: [https://chem.libretexts.org/Bookshelves/Analytical\\_Chemistry/Book%3A\\_Analytical\\_Chemistry\\_2.0\\_\(Harvey\)/11\\_Electrochemical\\_Methods/11.2%3A\\_Potentiometric\\_Methods](https://chem.libretexts.org/Bookshelves/Analytical_Chemistry/Book%3A_Analytical_Chemistry_2.0_(Harvey)/11_Electrochemical_Methods/11.2%3A_Potentiometric_Methods). [Accessed: 05-Feb-2019].
- [71] R. W. Cattrall and Henry. Freiser, "Coated wire ion-selective electrodes," *Anal. Chem.*, vol. 43, no. 13, pp. 1905–1906, Nov. 1971.
- [72] H. J. James, Gary. Carmack, and Henry. Freiser, "Coated wire ion-selective electrodes," *Anal. Chem.*, vol. 44, no. 4, pp. 856–857, Apr. 1972.



- 
- [73] A. Bandiziol, P. Palestri, F. Pittino, D. Esseni, and L. Selmi, "A TCAD-Based Methodology to Model the Site-Binding Charge at ISFET/Electrolyte Interfaces," *IEEE Trans. Electron Devices*, vol. 62, no. 10, pp. 3379–3386, Oct. 2015.
- [74] D. E. Yates, S. Levine, and T. W. Healy, "Site-binding model of the electrical double layer at the oxide/water interface," *J. Chem. Soc. Faraday Trans. 1 Phys. Chem. Condens. Phases*, vol. 70, no. 0, pp. 1807–1818, Jan. 1974.
- [75] R. E. G. van Hal, J. C. T. Eijkel, and P. Bergveld, "A novel description of ISFET sensitivity with the buffer capacity and double-layer capacitance as key parameters," *Sens. Actuators B Chem.*, vol. 24, no. 1, pp. 201–205, Mar. 1995.
- [76] P. Bergveld, "Development of an Ion-Sensitive Solid-State Device for Neurophysiological Measurements," *IEEE Trans. Biomed. Eng.*, vol. BME-17, no. 1, pp. 70–71, Jan. 1970.
- [77] Y. G. Bérubé and P. L. de Bruyn, "Adsorption at the rutile-solution interface: I. Thermodynamic and Experimental Study," *J. Colloid Interface Sci.*, vol. 27, no. 2, pp. 305–318, Jun. 1968.
- [78] Neamen, *Semiconductor Physics And Devices*. Irwin, 1992.
- [79] J. Mulder, W. A. Serdijn, A. C. van der Woerd, and A. H. M. van Roermund, *Dynamic Translinear and Log-Domain Circuits: Analysis and Synthesis*. Springer Science & Business Media, 2012.
- [80] E. Vittoz and J. Fellrath, "CMOS analog integrated circuits based on weak inversion operations," *IEEE J. Solid-State Circuits*, vol. 12, no. 3, pp. 224–231, Jun. 1977.
- [81] A. M. Ionescu and H. Riel, "Tunnel field-effect transistors as energy-efficient electronic switches," *Nature*, vol. 479, no. 7373, pp. 329–337, Nov. 2011.
- [82] B. Razavi, *Design of Analog CMOS Integrated Circuits*. McGraw-Hill Education, 2016.
- [83] J. M. Rothberg *et al.*, "An integrated semiconductor device enabling non-optical genome sequencing," *Nature*, vol. 475, no. 7356, pp. 348–352, Jul. 2011.
- [84] C. Toumazou *et al.*, "Simultaneous DNA amplification and detection using a pH-sensing semiconductor system," *Nat. Methods*, vol. 10, no. 7, pp. 641–646, Jul. 2013.
- [85] Y.- Huang *et al.*, "High performance dual-gate ISFET with non-ideal effect reduction schemes in a SOI-CMOS bioelectrical SoC," in *2015 IEEE International Electron Devices Meeting (IEDM)*, 2015, pp. 29.2.1-29.2.4.
- [86] "Signal Conditioning for High Impedance Sensors | Analog Devices." [Online]. Available: <https://www.analog.com/en/technical-articles/signal-conditioning-for-high-impedance-sensors.html>. [Accessed: 04-Mar-2019].

- 
- [87] J.- Zhang *et al.*, "All CMOS Integrated 3D-Extended Metal Gate ISFETs for pH and Multi-Ion (Na<sup>+</sup>, K<sup>+</sup>, Ca<sup>2+</sup>) sensing," in *2018 IEEE International Electron Devices Meeting (IEDM)*, 2018, pp. 12.1.1-12.1.4.
- [88] J. Zhang *et al.*, "Sweat Biomarker Sensor Incorporating Picowatt, Three-Dimensional Extended Metal Gate Ion Sensitive Field Effect Transistors," *ACS Sens.*, Jul. 2019.
- [89] Y. Liao, H. Yao, A. Lingley, B. Parviz, and B. P. Otis, "A 3- $\mu$ W CMOS Glucose Sensor for Wireless Contact-Lens Tear Glucose Monitoring," *IEEE J. Solid-State Circuits*, vol. 47, no. 1, pp. 335–344, Jan. 2012.
- [90] W. Jia *et al.*, "Electrochemical Tattoo Biosensors for Real-Time Noninvasive Lactate Monitoring in Human Perspiration," *Anal. Chem.*, vol. 85, no. 14, pp. 6553–6560, Jul. 2013.
- [91] S. Rigante *et al.*, "Sensing with Advanced Computing Technology: Fin Field-Effect Transistors with High-k Gate Stack on Bulk Silicon," *ACS Nano*, vol. 9, no. 5, pp. 4872–4881, May 2015.
- [92] A. M. Ionescu, "Energy efficient computing and sensing in the Zettabyte era: From silicon to the cloud," in *2017 IEEE International Electron Devices Meeting (IEDM)*, 2017, pp. 1.2.1-1.2.8.
- [93] G. Zheng, F. Patolsky, Y. Cui, W. U. Wang, and C. M. Lieber, "Multiplexed electrical detection of cancer markers with nanowire sensor arrays," *Nat. Biotechnol.*, vol. 23, no. 10, pp. 1294–1301, Oct. 2005.
- [94] X. Chen *et al.*, "Multiplexed analysis of molecular and elemental ions using nanowire transistor sensors," *Sens. Actuators B Chem.*, vol. 270, pp. 89–96, Oct. 2018.
- [95] M. Douthwaite, E. Koutsos, D. C. Yates, P. D. Mitcheson, and P. Georgiou, "A Thermally Powered ISFET Array for On-Body pH Measurement," *IEEE Trans. Biomed. Circuits Syst.*, vol. 11, no. 6, pp. 1324–1334, Dec. 2017.
- [96] S. Nakata, T. Arie, S. Akita, and K. Takei, "Wearable, Flexible, and Multifunctional Healthcare Device with an ISFET Chemical Sensor for Simultaneous Sweat pH and Skin Temperature Monitoring," *ACS Sens.*, vol. 2, no. 3, pp. 443–448, Mar. 2017.
- [97] E. Stern *et al.*, "Label-free immunodetection with CMOS-compatible semiconducting nanowires," *Nature*, vol. 445, no. 7127, pp. 519–522, Feb. 2007.
- [98] F. Bellando, E. Garcia-Cordero, F. Wildhaber, J. Longo, H. Guérin, and A. M. Ionescu, "Lab on skin<sup>TM</sup>: 3D monolithically integrated zero-energy micro/nanofluidics and FD SOI ion sensitive FETs for wearable multi-sensing sweat

- applications," in *2017 IEEE International Electron Devices Meeting (IEDM)*, 2017, pp. 18.1.1-18.1.4.
- [99] P. Bergveld, "Thirty years of ISFETOLOGY: What happened in the past 30 years and what may happen in the next 30 years," *Sens. Actuators B Chem.*, vol. 88, no. 1, pp. 1–20, Jan. 2003.
- [100] J. Bausells, J. Carrabina, A. Errachid, and A. Merlos, "Ion-sensitive field-effect transistors fabricated in a commercial CMOS technology," *Sens. Actuators B Chem.*, vol. 57, no. 1, pp. 56–62, Sep. 1999.
- [101] C. Panteli, P. Georgiou, and K. Fobelets, "Performance improvement of commercial ISFET sensors using reactive ion etching," *Microelectron. Eng.*, vol. 192, pp. 61–65, May 2018.
- [102] X. Huang, H. Yu, X. Liu, Y. Jiang, M. Yan, and D. Wu, "A Dual-Mode Large-Arrayed CMOS ISFET Sensor for Accurate and High-Throughput pH Sensing in Biomedical Diagnosis," *IEEE Trans. Biomed. Eng.*, vol. 62, no. 9, pp. 2224–2233, Sep. 2015.
- [103] Y. Liu, P. Georgiou, T. Prodromakis, T. G. Constandinou, and C. Toumazou, "An Extended CMOS ISFET Model Incorporating the Physical Design Geometry and the Effects on Performance and Offset Variation," *IEEE Trans. Electron Devices*, vol. 58, no. 12, pp. 4414–4422, Dec. 2011.
- [104] N. Moser, T. S. Lande, C. Toumazou, and P. Georgiou, "ISFETs in CMOS and Emergent Trends in Instrumentation: A Review," *IEEE Sens. J.*, vol. 16, no. 17, pp. 6496–6514, Sep. 2016.
- [105] N. Miscourides and P. Georgiou, "ISFET Arrays in CMOS: A Head-to-Head Comparison Between Voltage and Current Mode," *IEEE Sens. J.*, vol. 19, no. 4, pp. 1224–1238, Feb. 2019.
- [106] T.-E. Bae, H.-J. Jang, J.-H. Yang, and W.-J. Cho, "High Performance of Silicon Nanowire-Based Biosensors using a High-k Stacked Sensing Thin Film," *ACS Appl. Mater. Interfaces*, vol. 5, no. 11, pp. 5214–5218, Jun. 2013.
- [107] H. Abe, M. Esashi, and T. Matsuo, "ISFET's using inorganic gate thin films," *IEEE Trans. Electron Devices*, vol. 26, no. 12, pp. 1939–1944, Dec. 1979.
- [108] E. Shahrabi, J. Sandrini, B. Attarimashalkoubek, T. Demirci, M. Hadad, and Y. Leblebici, "Chip-level CMOS co-integration of ReRAM-based non-volatile memories," in *2016 12th Conference on Ph.D. Research in Microelectronics and Electronics (PRIME)*, 2016, pp. 1–4.

- 
- [109] N. Moser, C. Panteli, D. Ma, C. Toumazou, K. Fobelets, and P. Georgiou, "Improving the pH sensitivity of ISFET arrays with reactive ion etching," in *2017 IEEE Biomedical Circuits and Systems Conference (BioCAS)*, 2017, pp. 1–4.
- [110] S. Martinoia and G. Massobrio, "A behavioral macromodel of the ISFET in SPICE," *Sens. Actuators B Chem.*, vol. 62, no. 3, pp. 182–189, Mar. 2000.
- [111] P. Georgiou and C. Toumazou, "ISFET characteristics in CMOS and their application to weak inversion operation," *Sens. Actuators B Chem.*, vol. 143, no. 1, pp. 211–217, Dec. 2009.
- [112] P. A. Hammond and D. R. S. Cumming, "Performance and system-on-chip integration of an unmodified CMOS ISFET," *Sens. Actuators B Chem.*, vol. 111–112, pp. 254–258, Nov. 2005.
- [113] T. Matsuo and M. Esashi, "Methods of isfet fabrication," *Sens. Actuators*, vol. 1, pp. 77–96, Jan. 1981.
- [114] S. Jamasb, "An analytical technique for counteracting drift in ion-selective field effect transistors (ISFETs)," *IEEE Sens. J.*, vol. 4, no. 6, pp. 795–801, Dec. 2004.
- [115] S. Jamasb, S. Collins, and R. L. Smith, "A physical model for drift in pH ISFETs," *Sens. Actuators B Chem.*, vol. 49, no. 1, pp. 146–155, Jun. 1998.
- [116] P. Bühlmann, E. Pretsch, and E. Bakker, "Carrier-Based Ion-Selective Electrodes and Bulk Optodes. 2. Ionophores for Potentiometric and Optical Sensors," *Chem. Rev.*, vol. 98, no. 4, pp. 1593–1688, Jun. 1998.
- [117] H. K. Wipf, L. A. Pioda, Z. Stefanac, and W. Simon, "[Complexes of enniatins and other antibiotics with alkali metal ions]," *Helv. Chim. Acta*, vol. 51, no. 2, pp. 377–381, Mar. 1968.
- [118] L. A. R. Pioda, V. Stankova, and W. Simon, "Highly Selective Potassium Ion Responsive Liquid-Membrane Electrode," *Anal. Lett.*, vol. 2, no. 12, pp. 665–674, Dec. 1969.
- [119] M. Wipf *et al.*, "Selective Sodium Sensing with Gold-Coated Silicon Nanowire Field-Effect Transistors in a Differential Setup," *ACS Nano*, vol. 7, no. 7, pp. 5978–5983, Jul. 2013.
- [120] H. Li, M. S. Islam, and G. Koley, "Graphene-based ion-sensitive field effect transistor," in *2017 75th Annual Device Research Conference (DRC)*, 2017, pp. 1–2.
- [121] J. N. Hussain, N. Mantri, and M. M. Cohen, "Working Up a Good Sweat – The Challenges of Standardising Sweat Collection for Metabolomics Analysis," *Clin. Biochem. Rev.*, vol. 38, no. 1, pp. 13–34, Feb. 2017.

- 
- [122] S. Emaminejad *et al.*, "Autonomous sweat extraction and analysis applied to cystic fibrosis and glucose monitoring using a fully integrated wearable platform," *Proc. Natl. Acad. Sci. U. S. A.*, vol. 114, no. 18, pp. 4625–4630, 02 2017.
- [123] S. B. Kim *et al.*, "Soft, Skin-Interfaced Microfluidic Systems with Wireless, Battery-Free Electronics for Digital, Real-Time Tracking of Sweat Loss and Electrolyte Composition," *Small*, vol. 14, no. 45, p. 1802876, 2018.
- [124] S. B. Kim *et al.*, "Super-Absorbent Polymer Valves and Colorimetric Chemistries for Time-Sequenced Discrete Sampling and Chloride Analysis of Sweat via Skin-Mounted Soft Microfluidics," *Small*, vol. 14, no. 12, p. 1703334, 2018.
- [125] D. Bonn, J. Eggers, J. Indekeu, J. Meunier, and E. Rolley, "Wetting and spreading," *Rev. Mod. Phys.*, vol. 81, no. 2, pp. 739–805, May 2009.
- [126] L. Bromberg *et al.*, "Control of human skin wettability using the pH of anionic surfactant solution treatments," *Colloids Surf. B Biointerfaces*, vol. 157, pp. 366–372, Sep. 2017.
- [127] M. E. Ginn, C. M. Noyes, and E. Jungermann, "The contact angle of water on viable human skin," *J. Colloid Interface Sci.*, vol. 26, no. 2, pp. 146–151, Feb. 1968.
- [128] E. Garcia-Cordero, "Wearable System with Integrated Passive Microfluidics for Real-Time Electrolyte Sensing in Human Sweat," EPFL, Lausanne, 2018.
- [129] N. B. Twine, R. M. Norton, M. C. Brothers, A. Hauke, E. F. Gomez, and J. Heikenfeld, "Open nanofluidic films with rapid transport and no analyte exchange for ultra-low sample volumes," *Lab. Chip*, vol. 18, no. 18, pp. 2816–2825, Sep. 2018.
- [130] P. Bergveld, "New Amplification Method for Depth Recording," *IEEE Trans. Biomed. Eng.*, vol. BME-15, no. 2, pp. 102–105, Apr. 1968.
- [131] D. Takacs *et al.*, "Comparison of latch-up in p- and n-well CMOS circuits," in *1983 International Electron Devices Meeting*, 1983, pp. 159–163.
- [132] "Introduction | Bluefruit nRF52 Feather Learning Guide | Adafruit Learning System." [Online]. Available: <https://learn.adafruit.com/bluefruit-nrf52-feather-learning-guide?view=all>. [Accessed: 07-May-2019].
- [133] P. R. Nair and M. A. Alam, "Performance limits of nanobiosensors," *Appl. Phys. Lett.*, vol. 88, no. 23, p. 233120, Jun. 2006.
- [134] B. Nasri *et al.*, "15.7 Heterogeneous integrated CMOS-graphene sensor array for dopamine detection," in *2017 IEEE International Solid-State Circuits Conference (ISSCC)*, 2017, pp. 268–269.

- [135] A. Craggs, G. J. Moody, and J. D. R. Thomas, "PVC matrix membrane ion-selective electrodes. Construction and laboratory experiments," *J. Chem. Educ.*, vol. 51, no. 8, p. 541, Aug. 1974.
- [136] E. Bakker, P. Bühlmann, and E. Pretsch, "Polymer Membrane Ion-Selective Electrodes—What are the Limits?," *Electroanalysis*, vol. 11, no. 13, pp. 915–933, 1999.
- [137] E. Bakker, M. Lerchi, T. Rosatzin, B. Rusterholz, and W. Simon, "Synthesis and characterization of neutral hydrogen ion-selective chromoionophores for use in bulk optodes," *Anal. Chim. Acta*, vol. 278, no. 2, pp. 211–225, Jun. 1993.
- [138] J. J. Griffin and G. D. Christian, "Long-term stability of ion-selective valinomycin membranes," *Talanta*, vol. 30, no. 3, pp. 201–203, Mar. 1983.
- [139] Y. Miyahara, K. Yamashita, S. Ozawa, and Y. Watanabe, "Shift and drift of electromotive forces of solid-state electrodes with ion-selective liquid membranes," *Anal. Chim. Acta*, vol. 331, no. 1, pp. 85–95, Sep. 1996.
- [140] T. Hattori, F. Dasai, H. Sato, R. Kato, and K. Sawada, "CCD Multi-Ion Image Sensor with Four 128 × 128 Pixels Array," *Sensors*, vol. 19, no. 7, p. 1582, Jan. 2019.
- [141] N. Ruecha, O. Chailapakul, K. Suzuki, and D. Citterio, "Fully Inkjet-Printed Paper-Based Potentiometric Ion-Sensing Devices," *Anal. Chem.*, vol. 89, no. 19, pp. 10608–10616, Oct. 2017.
- [142] E. J. R. Sudhölter, P. D. van der Wal, M. Skowronska-Ptasinska, A. van den Berg, and D. N. Reinhoudt, "Ion-sensing using chemically-modified ISFETs," *Sens. Actuators*, vol. 17, no. 1–2, pp. 189–194, May 1989.
- [143] H.-J. Jang *et al.*, "Electronic Cortisol Detection Using an Antibody-Embedded Polymer Coupled to a Field-Effect Transistor," *ACS Appl. Mater. Interfaces*, vol. 10, no. 19, pp. 16233–16237, May 2018.
- [144] S. Rebouillat and F. Pla, "State of the Art Manufacturing and Engineering of Nanocellulose: A Review of Available Data and Industrial Applications," *J. Biomater. Nanobiotechnology*, vol. 04, p. 165, Apr. 2013.
- [145] S. Sen, J. D. Martin, and D. S. Argyropoulos, "Review of Cellulose Non-Derivatizing Solvent Interactions with Emphasis on Activity in Inorganic Molten Salt Hydrates," *ACS Sustain. Chem. Eng.*, vol. 1, no. 8, pp. 858–870, Aug. 2013.
- [146] J. O. Zoppe, N. C. Ataman, P. Mocny, J. Wang, J. Moraes, and H.-A. Klok, "Surface-Initiated Controlled Radical Polymerization: State-of-the-Art, Opportunities, and Challenges in Surface and Interface Engineering with Polymer Brushes," *Chem. Rev.*, vol. 117, no. 3, pp. 1105–1318, Feb. 2017.

## Junrui Zhang

Electronics and Microfabrication Engineer, DOB: 26.08.1988  
Chemin des Triades 4, CH-1024 Ecublens, Switzerland  
Cell phone: +41766200089  
Email: [junruizhang@gmail.com](mailto:junruizhang@gmail.com)



### **Skills**

- **Project management:** Team leader in UESTC-UEC (University of Electro-Communications) International Remote Robot Development Lab.
- **Microelectronics:** Analog Application Specific Integrated Circuits (ASIC).
- **Microwave engineering:** Passive microwave/millimeter wave frequency components.
- **Micro & Nano fabrication:** Device fabrication in Cleanroom (ISO 5, 6, 7). Experience in photolithography, thin-film deposition, etching and imaging.
- **Electronics:** High speed multi-layer PCB design, Flexible PCB design, DSP, microcontroller, electronic characterization.
- **Bio-chemical engineering:** on-body and ex-situ test of biomarkers, analytical chemistry.
- **Programming language:** Java, C, Matlab, Python.

### **Working Experience**

R&D engineer

EPFL-Nanolab / Xsensio SA

July 2016 – now  
Lausanne, Switzerland

- Project management: IoT sensing platform and software development.
- Wearable biomarker sensor design and characterization.

R&D engineer

Institute IPRINT

July 2014 – Oct 2016  
Fribourg, Switzerland

- Design of low power analog CMOS circuit for capacitive sensor Readout.
- Design of ultra-low power operational amplifier in 0.35  $\mu\text{m}$  CMOS technology.
- Design of lock-in amplifier ASIC.

Research Assistant

City University of Hong Kong

Sept 2013 – Dec 2013  
Hong Kong, China

- Investigation of Omni-directional Dielectric Resonator Antenna for Wireless Communications.
- Investigation Electromagnetic Compatibility in RF System-in-Package.

### **Education**

PhD

École Polytechnique Fédérale de Lausanne

**Thesis:** Wearable System for Real-Time Sensing of Biomarkers in Human Sweat.

July 2014 – July 2019  
Lausanne, Switzerland

Master

University of Electronic Science and Technology of China

**Thesis:** Ultra-wideband Reconfigurable Antenna Array

Sept 2010 – July 2013  
Chengdu, China



Bachelor  
University of Electronic Science and Technology of China  
Thesis: Design of UHF Wideband Antenna and Its Matching Network

Sept 2006 – July 2010  
Chengdu, China

### **Research Experiences**

Doctoral Assistant  
École Polytechnique Fédérale de Lausanne

July 2014 – July 2019  
Lausanne, Switzerland

- Development of miniaturized point of care devices with bio-compatible substrates, for quantifying biomarkers (pH,  $\text{Na}^+$ ,  $\text{K}^+$ ) in human sweat. Main activities include research on electrochemical methods and fabrication in clean room, electronic design and IoT platform integration.

Research assistant  
University of Electronic Science and Technology of China

Sept 2010 – July 2013  
Chengdu, China

- Designed radiation pattern reconfigurable antenna elements in order to realize a phased array that is able to scan its main beam in a wide range from  $-60^\circ$  to  $60^\circ$  in the H-plane.
- Realized a frequency-tunable electrically small antenna, with a varactor diode mounted on a slot of a semi-ring antenna

### **Publications**

- Garcia-Cordero Erick, Bellando Francesco, Zhang Junrui, et al. "Fully integrated ISFET-based wearable sweat analyzer with low-volume microfluidic interface," ACS Nano, 2018.
- Zhang Junrui, et al., "All CMOS Integrated 3D-Extended Metal Gate ISFETs for pH and Multi-Ion ( $\text{Na}^+$ ,  $\text{K}^+$ ,  $\text{Ca}^{2+}$ ) sensing," IEDM 2018, San Francisco, CA.
- Zhang Junrui, Bellando Francesco, Garcia-Cordero Erick, Ionescu, Mihai Adrian (2018). Field effect transistor device and method for sensing ions and biomarkers in a fluid. U.S. Patent Application No. 62/688,413.
- Zhang Junrui, et al., "CMOS compatible energy autonomous wearable sensor system for in situ sweat analysis," MNE 2018, Copenhagen.
- Zhang Junrui, et al., "CMOS 3D-Extended Metal Gate ISFETs with Near Nernstian Ion Sensitivity," 2018 76th Device Research Conference, Santa Barbara, CA.
- Zhang Junrui, et al., "Low power analog frontend for ISFET sensor readout," 17th International Meeting on Chemical Sensors, 2018, Vienna.
- Zhang Junrui, A. M. Ionescu and M. Mazza, "Low-energy biomarker detection through charge-based impedance measurements," 2016 IEEE SENSORS, Orlando, FL.
- M. C. Tang, R. W. Ziolkowski, S. Xiao, M. Li and Junrui Zhang, "Frequency-Agile, Efficient, Near-Field Resonant Parasitic Monopole Antenna," IEEE Transactions on Antennas and Propagation, vol. 62, no. 3, pp. 1479-1483, March 2014.
- Zhang Junrui, Xiao Shaoqiu, et al. Time Domain Characteristics of a Novel Pattern Reconfigurable Pulse Radiating Antenna. IEEE Antenna and Wireless Propagation Letter, Vol. 11, pp. 1202-1205, Oct. 2012.
- Zhang Junrui, Xiao Shaoqiu, et al. Design of UHF Truncated Monopole Antenna and Its Matching Network(in Chinese). Journal of Applied Sciences, Vol.29, No.4, pp. 423-427, Jul. 2011.
- Hai-Feng Lü, Junrui Zhang, et al. Current noise correlations in double quantum dots asymmetrically coupled to external leads. Journal of Applied Physics, 107, 034314 (2010)





